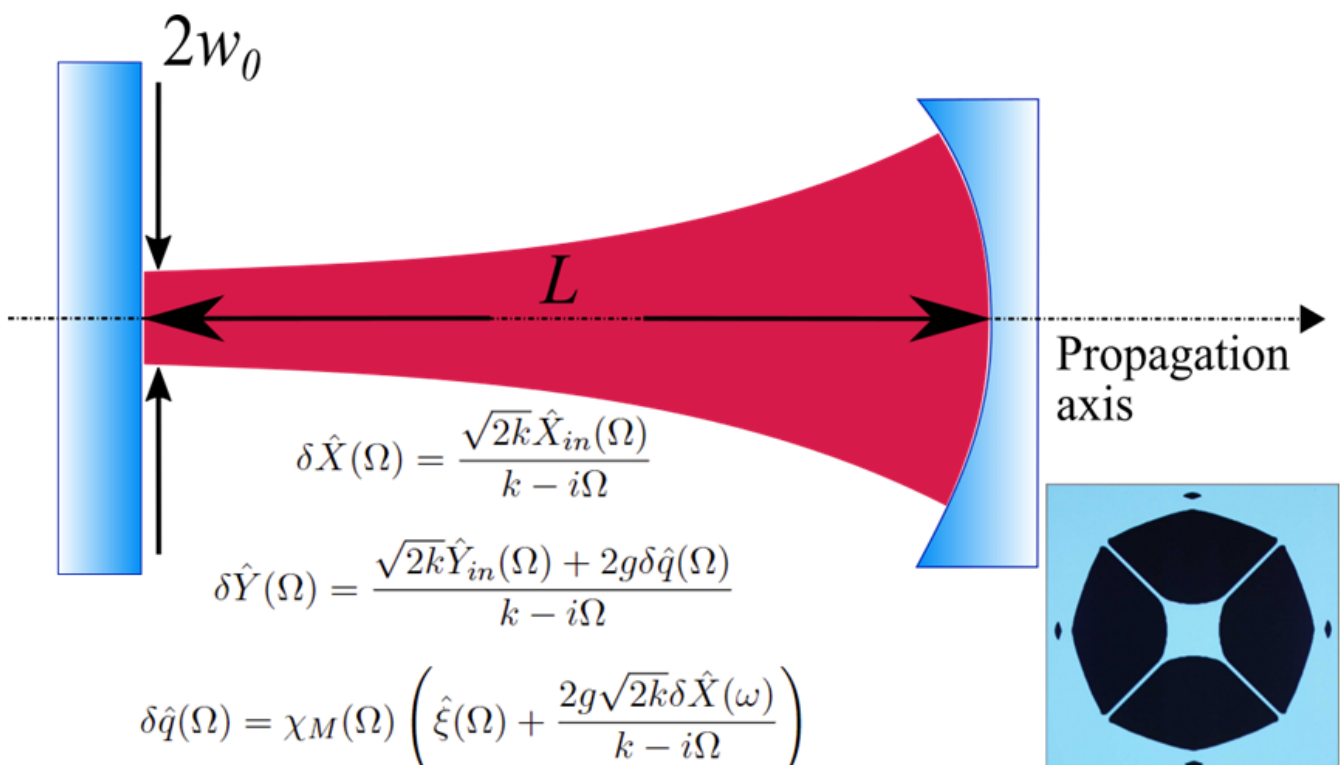


# Feedback cooling of a mechanical resonator from room temperature close to its ground state

Angelo Manetta

PhD Thesis





## **Feedback cooling of a mechanical resonator from room temperature close to its ground state**

PhD Thesis

A dissertation submitted to the Department of Physics at the Technical University of Denmark in partial fulfillment of the requirements for the degree of philosophiae doctor.

July, 2022

By  
Angelo Manetta

Copyright:      Reproduction of this publication in whole or in part must include the customary bibliographic citation, including author attribution, report title, etc.

Published by:   DTU, Quantum Physics and Information Technology (QPIT), Fysikvej 311, 2800 Kgs. Lyngby Denmark

*Che dici? Sopravviveremo? Sopravviveremo. Il problema e' che sopravviveremo.*  
What do you think? Will we survive? We'll survive. Trouble is we will survive.  
*Papa'*

*Si ti vi ka than Kavajsi.*  
Do as the people from Kavajë.  
*Roccia's mom*

## Abstract

In the last two decades, cavity optomechanics has gained a central spot in the research on quantum physics, thanks to its premise to integrate macroscopic oscillators of different nature – optical and mechanical – into a single platform. Here lies the challenge though, as mechanical resonators are typically not in their ground state at room temperature, unlike light. In the sideband unresolved regime, where the optical damping rate is much larger than the mechanical angular frequency, feedback cooling has proven to be a valid approach to overcome this problem. Its working principle consists of a continuous measurement of the mechanical displacement and application of a proportional damping force. Unfortunately, so far its success has relied on operation in a cryogenic environment, which represents a major obstacle when scaling up experiments. In this work, we set to explore the possibility to use feedback cooling to steer a millimeter-sized mechanical resonator into a state of phonon occupancy as low as possible starting from room temperature. Although the minimum occupancy we achieve is 1800, far from the onset of quantum behavior, we pave the way for future success by offering a discussion of which parameters need further optimization in order to obtain a truly macroscopic quantum state. Our experimental scheme operates at 1550 nm, ensuring the viability of integration with other computation and telecommunication protocols. We use phase-sensitive detection of light reflected off high-finesse optical cavities to monitor the mechanical motion and pay great attention to minimizing optical losses, thus making our platform suitable for interface with sources of non classical light such as squeezers. Finally, the low frequency and high quality factor of our mechanical resonators produce long coherence times, particularly appealing for implementing quantum protocols such as state transfer.

I de sidste to årtier har kavitets optomekanik fået en central rolle inden for forskning i kvantefysik. Det skyldes dens evne at integrerer forskellige typer af makroskopiske oscillatorer – optiske og mekaniske – i én enkel platform. Udfordringen er dog at mekaniske resonatorer typisk ikke er i deres kvantemekaniske grundtilstand ved stue temperatur - modsat optisk lys. I det uopløste sidebånd regime, hvor den optiske dæmpningsrate er meget større end den mekaniske frekvens, har feedback cooling vist sig som en valid metode til at overkomme denne udfordring. Metoden består af en kontinuerlige måling af den mekaniske oscillators forskydning og anvendelse af en proportional dæmpningskraft. Desværre er denne metodes succes indtil nu afhængig af kryogene temperaturer, hvilket er en kæmpe forhindring for at skalere eksperimenterne op. I dette arbejde vil vi udforske nye muligheder for at anvende feedback cooling til at styre en millimeter stor mekanisk resonator ind i en kvantetilstand med den lavest mulige fonon okkupans startende fra stue temperatur. Selvom den mindste okkupans vi opnår er på 1800, hvilket er lang fra der hvor kvantemekaniske effekter begynder at spille en rolle, så viser vi vejen til fremtidig succes ved at diskutere hvilke parametre, som skal optimeres yderligere for at opnår en makroskopisk kvantetilstand. Vores eksperimentelle forsøg opererer ved 1550 nm, hvilket gør at muligt at integrere med andre beregnings og telekommunikations protokoller. Vi anvender fase-følsom detektion af lyset reflekteret fra høj finesses kaviteten til at følge den mekaniske bevægelse af resonatoren og derudover er vi meget opmærksomme på at minimere det optisk lys tab, hvilket betyder at vores platform kan fungere med ikke-klassisk lyskilder, så som squeezers. Endelig, vil vores lav frekvens og høj kvalitets faktor mekaniske resonatorer producere lange kohærens tider, hvilket gør dem særlig interessante at anvende til kvanteinformation protokoler, som f.eks. tilstand overførsler mellem lys og mekanik.

## Acknowledgements

To begin with, I wish to thank my supervisor Ulrik Lund Andersen, for the advise, the time and the energy invested on me. I will not forget the weekly meetings and the long, inspiring physics discussions. More importantly, thank you for believing in me, giving me a second chance at a PhD and welcoming me into QPIT. Thanks also to my cosupervisors Jonas Schou Neergaard-Nielsen and Warwick Bowen for their time and availability to discuss problems that sometimes seemed to have no solution. I wish to thank Ulrich Busk Hoff for being my 'unofficial' cosupervisor, for teaching me the small tricks of the lab and the art of navigating DTU. Special thanks go to Tobias Gehring, for the countless ours he spent discussing electronics and optics with me, for helping me out of passion for science and sympathy for an Italian student lost in physics.

Science is seldom an individual achievement. And I definitely had a great team. First off, I owe a great deal of gratitude to Iman, mentor and friend, for teaching me the beauty of optomechanics and the elegance of photography, for listening to me and for the many stories about Persia. Thanks to Joost, for his 'quick and dirty' style of problem solving, for guiding and supporting me even after leaving DTU. And no, I will never forgive you for designing the vertical cavity. Thanks to Dennis and Frederik for being always eager to help, even on super-short notice, for their advice and for the effort at making our meetings more cheerful. Thanks to Sissel, for being always supportive and for bringing color and humanity to our group. Finally, many thanks to Luiz, for the help and the wisdom, for learning with me, for the hours discussing judo, for the tales of Brasil and for introducing me to little Thomas.

Many thanks to the non-optomech members of QPIT who dedicated so much of their time and effort to seeing me succeed. First and foremost, thanks to Rayssa, for the help and the good spirits, for never saying no when I needed help. Thanks to Jens, Casper, Mikkel, Xueshi and Renato. And of course, thanks to Iyad, but we'll get back to that later.

Thanks to all my QPIT friends, Maxime, Luca, Deepak, Anna, Adnan, Rasmus, Santiago, Teresa, Dino, Josh and Iyad, for making work days as fun as holidays.

Grazie a mamma e papa'. Per tutto. Per l'amore, il supporto, la saggezza e gli insegnamenti. Grazie a Federica, per volermi bene cosi' incondizionatamente.

Grazie ai miei Tarati, per essere questa presenza costante e amorevole che da undici anni illumina la mia vita. Grazie a Roccia, per esserci sempre, perche' gli anni e la distanza ci hanno arricchito invece di allontanarci. Grazie a Giulia, perche' si ricorda sempre di me e tiene viva la nostra amicizia.

As much as science, life is often a collective effort too. I owe so much to my Copenhagen family, who put so much effort in keeping lively and exciting the (fewer and fewer) hours I spent outside the lab, for constantly reminding me that life is meant to be lived. Thanks to Silvia, Deepak, Giorgia, Rob, Grazia, Michele, Maxime, Hermine, Helene, Vilija, Michela, Francesca and Ainoa.

Thanks to Vlad, for the quality time, the crazy adventures and for teaching me to believe in myself. For introducing me to judo, one of the greatest discoveries of my PhD years. Speaking of which, thanks to Victor, Jakob, Diogo, Thomas, Gustav, Yorky for the hours on the tatami, some of the best of my time in Copenhagen.

Thanks to Andrea. For changing my life forever. For surprising me, always. For showing me a different perspective. For teaching me to challenge myself, aim higher and overcome my fears and limitations. For listening and supporting me, for teaching me to love nature. I will miss you so much, but don't worry, Canada is only a 30-km bike ride away.

Thanks to Iyad, brother, friend, flatmate and colleague. For everything. For his emotional support in my everyday life and practical support with my PhD. For his enormous heart, his talent with impressions and the endless discussions listing down pros and cons of capitalism. I thank my fate for letting me cross paths with this most remarkable young man.

# List of scientific dissemination

## Peer-reviewed conference contributions

A. Manetta, I. M. Haghghi, D. Høj, J. van der Heijden, U. B. Hoff, and U. L. Andersen, Feedback cooling of a trampoline in a high-finesse cavity from room temperature, *2021 Conference on Lasers and Electro-Optics Europe and European Quantum Electronics Conference*, OSA Technical Digest, Optica Publishing Group, 2021.



# Contents

Abstract . . . . .	iii
Acknowledgements . . . . .	iv
<b>1 Introduction</b>	<b>1</b>
<b>2 Theory</b>	<b>3</b>
2.1 Quantum mechanics . . . . .	3
2.1.1 Quantum measurements . . . . .	3
2.1.2 Quantum harmonic oscillator . . . . .	3
2.1.3 Quantum states of light . . . . .	5
2.1.3.1 Fock states . . . . .	5
2.1.3.2 Coherent states . . . . .	5
2.1.3.3 Thermal states . . . . .	6
2.2 Modulation of the light . . . . .	7
2.2.1 Phase modulation . . . . .	7
2.2.2 Frequency modulation . . . . .	7
2.2.3 Amplitude modulation . . . . .	8
2.3 Power spectral density . . . . .	8
2.4 Optomechanical interaction . . . . .	9
2.4.1 Driven Hamiltonian in a rotating frame . . . . .	10
2.4.2 Quantum Langevin equations of motion . . . . .	10
2.4.3 Semi-classical dynamics . . . . .	11
2.4.4 On-resonance driving . . . . .	12
2.4.5 Mechanical power spectral density . . . . .	13
2.4.6 Input-output relation . . . . .	13
<b>3 Experimental techniques</b>	<b>15</b>
3.1 Photodetection . . . . .	15
3.1.1 Direct detection . . . . .	15
3.1.2 Homodyne detection . . . . .	15
3.1.2.1 Homodyne setup . . . . .	17
3.1.3 Quantum efficiency . . . . .	18
3.1.3.1 Homodyne visibility . . . . .	19
3.1.3.2 Shot-noise scaling with optical power . . . . .	21
3.2 Mechanical resonators . . . . .	22
3.2.1 Out-of-plane modes . . . . .	22
3.2.2 Mechanical properties . . . . .	23
3.3 Optical resonators . . . . .	25
3.3.1 Resonance condition . . . . .	26
3.3.1.1 Cavity coupling regimes . . . . .	29
3.3.2 Gaussian modes . . . . .	29
3.3.3 Cavity stability and eigenmodes . . . . .	30
3.3.4 Cavity design . . . . .	34
3.3.5 Mode-matching laser to cavity fundamental mode . . . . .	35
3.3.6 Optomechanical assembly . . . . .	36
3.3.6.1 Experimental setup I—Vertical cavity . . . . .	36
3.3.6.2 Experimental setup II—Horizontal cavity . . . . .	39

3.3.6.3	Aligning laser to a cavity . . . . .	43
3.3.7	Cavity characterization . . . . .	45
3.3.7.1	Cavity escape efficiency . . . . .	45
3.3.7.2	Optical losses and efficiencies . . . . .	47
3.3.7.3	Optical linewidth . . . . .	47
3.3.7.4	FSR, estimate of effective cavity length and finesse . . . . .	49
3.3.8	Frequency locking . . . . .	50
3.3.8.1	Pound-Drever-Hall scheme . . . . .	51
3.3.8.2	Different implementations of PDH scheme . . . . .	53
3.3.8.3	Cavity detuning . . . . .	55
3.4	Ringdown measurements of mechanical quality factor . . . . .	56
3.5	Single-photon optomechanical coupling . . . . .	57
3.5.1	Optomechanical spring effect . . . . .	59
3.5.2	Quantum noise thermometry . . . . .	62
3.5.2.1	EOM modulation depth . . . . .	64
<b>4</b>	<b>Optomechanical feedback cooling</b>	<b>67</b>
4.1	Theory of feedback cooling . . . . .	67
4.1.0.1	Driving forces . . . . .	69
4.2	Feedback controller . . . . .	70
4.3	Calibration of mechanical spectra . . . . .	71
4.4	Optomechanical feedback cooling I . . . . .	73
4.4.1	Experimental setup . . . . .	73
4.4.2	Trampoline . . . . .	75
4.4.3	Experimental parameters . . . . .	76
4.4.4	Results . . . . .	77
4.4.5	Conclusions: how to move forward . . . . .	79
4.5	Optomechanical feedback cooling II . . . . .	82
4.5.1	Experimental setup . . . . .	83
4.5.2	Phononic membrane . . . . .	84
4.5.3	Phononic membrane: Experimental parameters . . . . .	86
4.5.4	Phononic membrane: Results . . . . .	89
4.5.5	Topology-optimized trampoline . . . . .	92
4.5.6	TOTrampoline: Experimental parameters . . . . .	93
4.5.7	TOTrampoline: Results . . . . .	96
<b>5</b>	<b>Conclusions</b>	<b>99</b>
	<b>Bibliography</b>	<b>101</b>

# 1 Introduction

In the 17th century, during his studies on comets Kepler noticed they always feature a tail pointing away from the sun. He conjectured the existence of a *radiation pressure* acting between the celestial body and the traveling objects. This phenomenon was fully understood only two centuries later by James Clerk Maxwell, who provided an explanation based on his equations for electromagnetism. He argued that the electromagnetic radiation carries a momentum, hence applies a pressure to any surface it impinges on. Finally, experimental proof was reported independently by Pyotr Lebedev in 1900 and by Ernest Fox Nichols and Gordon Ferrie Hull in 1901 [1].

This work focuses on optomechanics, the branch of physics dealing with the interaction between an electromagnetic field and a mechanical resonator driven by radiation pressure force. In the last two decades optomechanics has earned the limelight thanks to both its relevance in fundamental science [2] and its wide range of applications, ranging from sensing [3], to transduction [4] and quantum computing [5]. The gravitational-waves community first showed interest in optomechanics in the context of interferometric detection [6]. In 1967, Braginsky reported the perturbation effect caused by a light beam measuring the position of a mirror on the measurement itself. The exchange of momentum between the light and its target brings about an imprecision in the measurement which is fed back to the measuring light. This is usually referred to as *quantum back action* and provides a lower boundary to the sensitivity of displacement measurements. Braginsky, Khalili and Thorne later developed a comprehensive theory of quantum measurement, encompassing the effects of radiation-pressure quantum fluctuations on measurement accuracy [7].

Small changes in the position of massive objects can be detected through optical interferometric measurement. For example, a resonant beam of light can be used to probe the displacement of the end mirror of a Fabry-Perot interferometer, as its motion induces significant changes in the light phase. The uncertainty of a measurement of such phase shift corresponds to an *imprecision noise* in the displacement measurement which bears an inverse proportionality with the input optical power. On the other hand, increasing power corresponds to an increase of the number of intracavity photons, hence of the backaction noise. In an experiment of unitary efficiency, a trade-off can be found where the two noise sources carry an equal contribution, known as the *standard quantum limit* (SQL).

Braginsky also studied the case of an optical cavity with one end mirror connected to a mechanical oscillator. He observed that when the lifetime of a photon inside the cavity is longer than the mechanical oscillation period, the radiation pressure force results delayed in phase and builds up an effective heating or cooling of the mechanical resonator. The latter case is known as *sideband cooling* and has been demonstrated experimentally through numerous studies [8, 9]. The unresolved sideband regime, where cavity linewidth is far larger than the frequency of mechanical oscillation, offers the option of a different approach, where the radiation pressure can be engineered through an electro-optic system in order to damp the mechanical oscillations [10]. This technique is usually referred to as *feedback cooling*. A similar scheme proved successful at cooling down trapped ions into their motional ground state [11]. At room temperature, light in the visible and infrared range is in the ground state thanks to its high frequency. The same does not hold for mechanical oscillators with resonance frequencies in the kHz or MHz range, whose phonons follow the Bose-Einstein statistical distribution of population. As a consequence, classical thermal noise prevents observation of the quantum behaviour of the mechanical resonator. Using an electro-optomechanical system, ground-state cooling and real-time optimal quantum control of a trapped silica nanosphere with a radius of 72 nm and a mass of  $3 \times 10^{-18}$  kg has recently been proved [12]. It is then an obvious question to ask whether experimental protocols such as feedback cooling can be used to steer massive objects, e.g. millimeter-sized membranes, into their ground state. If possible, this

would represent the ultimate achievement for optomechanics, as it would bring about the possibility to interface two truly macroscopic quantum states. Great success has been achieved both in the near-infrared [13] and microwave [14] range of the electromagnetic field, although ground-state cooling has so far been proven possible only with the aid of a cryogenic environment reducing the phonon occupancy from its room-temperature value. This represents a major hindrance when considering technological ramifications or integration with other experimental platforms, as cryogenic equipment raises the operation costs, offers limited space to allocate optomechanical systems and entails numerous practical constraints. In recent times, encouraging results have been obtained. In particular, room-temperature feedback cooling of a fully integrated on-chip optomechanical system down to a minimum of occupancy of 27 phonons has been reported [15].

The aim of this work is to explore the potential of room-temperature experimental setups with regard to optomechanical feedback cooling of millimeter-sized oscillators with effective mass in the order of nanograms. We start from the earlier work carried out in our group [16], evaluating the performance of a previous setup and discussing the process of designing and building a new one, optimizing its parameters to achieve better experimental results. We harness the knowledge on fabrication of micromechanical resonators with high quality factors that has been developed in our group within the last few years [17] and exploit it to achieve feedback cooling of oscillators with mechanical frequencies up to 1.4 MHz down to 1800 phonons. The theoretical framework of optomechanics will be first discussed, followed by the experimental techniques necessary to perform a feedback cooling. Finally, our experimental results will be presented.

## 2 Theory

### 2.1 Quantum mechanics

#### 2.1.1 Quantum measurements

Non-commuting observables constitute the backbone of quantum mechanics. They represent physical quantities such as position and momentum, whose measurement corresponds to applying an operator  $\hat{O}$  to a quantum state  $|\psi\rangle$ . The outcome of the measurement is given by the operator eigenvalues  $O_i$  that can be found solving the equation

$$\hat{O} |\psi_i\rangle = O_i |\psi_i\rangle \quad (2.1)$$

Hence, if our system is prepared in an arbitrary state  $|\psi\rangle$ , the probability that a measurement of the observable  $\hat{O}$  returns  $O_i$  is given by the expectation value of  $\hat{O}$

$$\langle \hat{O} \rangle = \langle \psi | \hat{O} | \psi \rangle \quad (2.2)$$

while the uncertainty of the measurement outcome is given by the operator's variance

$$Var(\hat{O}) = (\Delta \hat{O})^2 = \langle \hat{O}^2 \rangle - \langle \hat{O} \rangle^2 \quad (2.3)$$

If two operators  $\hat{A}$  and  $\hat{B}$  share a common set of eigenvectors, their commutator  $[\hat{A}, \hat{B}] \equiv \hat{A}\hat{B} - \hat{B}\hat{A}$  is null and we have  $\hat{A}\hat{B} = \hat{B}\hat{A}$ . This means the order in which the two measurements  $\hat{A}$  and  $\hat{B}$  are performed does not produce different outcomes, which is not true for non-commuting operators such that  $[\hat{A}, \hat{B}] \neq 0$ . This results in an uncertainty relation fixing a lower boundary on the precision of subsequent measurements

$$\Delta \hat{A} \Delta \hat{B} \geq \frac{1}{2} \left| [\hat{A}, \hat{B}] \right| \quad (2.4)$$

#### 2.1.2 Quantum harmonic oscillator

In quantum physics many different wave-like physical systems can be modeled as harmonic oscillators, such as the light field in an optical cavity and an isolated vibrational mode in a mechanical resonator. The energy quantum of the harmonic oscillator is then referred to as *photon* in the case of an electromagnetic field and *phonon* for a mechanical-displacement field. The behaviour of a harmonic oscillator of mass  $m$  and frequency  $\omega$  is described by the operators of position  $\hat{q}$  and momentum  $\hat{p}$  and by the Hamiltonian

$$\hat{H} = \frac{m\omega\hat{q}^2}{2} + \frac{\hat{p}^2}{2m} \quad (2.5)$$

Please note that the position and momentum operators do not commute, as we have  $[\hat{q}, \hat{p}] = i\hbar$ . They can both be expressed by a linear combination of the *creation*  $\hat{a}^\dagger$  and *annihilation*  $\hat{a}$  operators

$$\hat{q} = \sqrt{\frac{\hbar}{2m\omega}} (\hat{a}^\dagger + \hat{a}) \quad (2.6)$$

$$\hat{p} = \sqrt{\frac{m\hbar\omega}{2}} i (\hat{a}^\dagger - \hat{a}) \quad (2.7)$$

The creation and annihilation operators are also known as *ladder* operators because their effect on the state  $|n\rangle$  of a harmonic oscillator—populated by a number  $n$  of quanta—is to add or subtract a single quantum

$$\hat{a}^\dagger |n\rangle = \sqrt{n+1} |n+1\rangle \quad (2.8)$$

$$\hat{a} |n\rangle = \sqrt{n} |n-1\rangle \quad (2.9)$$

We can define an occupancy-number operator  $\hat{n} \equiv \hat{a}^\dagger \hat{a}$  with

$$\hat{a}^\dagger \hat{a} |n\rangle = n |n\rangle \quad (2.10)$$

We can thus define the ground state  $|0\rangle$  of the harmonic oscillator such that  $\hat{a} |0\rangle = 0$  and the Hamiltonian in Eq. 2.5 can be rewritten as

$$\hat{H} = \hbar\omega \left( \hat{a}^\dagger \hat{a} + \frac{1}{2} \right) = \hbar\omega \left( \hat{n} + \frac{1}{2} \right) \quad (2.11)$$

Solving the time-independent Schroedinger equation yields the energy spectrum  $E_n$  of the quantum oscillator

$$\hat{H} |n\rangle = E_n |n\rangle = \hbar\omega \left( \hat{n} + \frac{1}{2} \right) |n\rangle \quad (2.12)$$

The harmonic oscillator energy levels are equally spaced by  $\hbar\omega$  and the ground state has *zero-point energy*  $\frac{1}{2}\hbar\omega$ . Given the definitions 2.6 and 2.7, the *zero-point motion*  $q_{zpf} = \sqrt{\frac{\hbar}{2m\omega}}$  and *zero-point momentum*  $p_{zpf} = \sqrt{\frac{m\hbar\omega}{2}}$  of a quantum harmonic oscillator can be defined.

Although the quantum harmonic oscillator is well described by the ladder operators, these are not Hermitian, hence they do not represent measurable observables. On the other hand, we can define a general Hermitian quadrature operator  $\hat{X}^\theta$  given by a linear combination of their real and imaginary parts.

$$\hat{X}^\theta = \hat{a}(\omega) e^{-i\theta} + \hat{a}^\dagger(\omega) e^{i\theta} = \hat{X}^q(\omega) \cos \theta + \hat{X}^p(\omega) \sin \theta \quad (2.13)$$

with

$$\hat{X}^q = \hat{a}^\dagger(\omega) + \hat{a}(\omega) \quad (2.14)$$

$$\hat{X}^p = -i \left( \hat{a}(\omega) - \hat{a}^\dagger(\omega) \right) \quad (2.15)$$

Please note that we get a new commutation relation

$$[\hat{X}^q, \hat{X}^p] = 2i \quad (2.16)$$

from which an uncertainty relation stems

$$\Delta(\hat{X}^q) \Delta(\hat{X}^p) \geq 1 \quad (2.17)$$

### 2.1.3 Quantum states of light

#### 2.1.3.1 Fock states

We already encountered Fock states  $|n\rangle$ , eigenstates of the number operator  $\hat{n}$

$$\hat{n} |n\rangle = n |n\rangle \quad (2.18)$$

described by eigenvalues  $\hbar\omega (n + \frac{1}{2})$ . These Fock states have null variance

$$Var(\hat{n}) = \langle n | \hat{n}^2 | n \rangle - \langle n | \hat{n} | n \rangle^2 \quad (2.19)$$

Also the expectation value of a measurement of an arbitrary quadrature  $X^\theta$  is null

$$\langle n | \hat{X}^\theta | n \rangle = 0 \quad (2.20)$$

The Fock ground state  $|0\rangle$  is called *vacuum state* and its properties determine the fundamental limit in the precision of classical-field measurements. Evaluating the corresponding mean value and variance for the phase and amplitude quadratures, we obtain

$$\langle \hat{X}^q \rangle = \langle \hat{X}^p \rangle = 0 \quad (2.21)$$

and

$$Var(\hat{X}^q) = Var(\hat{X}^p) = 1 \quad (2.22)$$

Fluctuations of the quantum vacuum state bring about the standard quantum limit of field quadrature measurements, usually referred to as *shot noise*.

#### 2.1.3.2 Coherent states

*Coherent states* provide a quantum approximation of a laser field, as they are defined by eigenstates of the annihilation operator

$$\hat{a} |\alpha\rangle = \alpha |\alpha\rangle \quad (2.23)$$

$$\langle \alpha | \hat{a}^\dagger = \alpha^* \langle \alpha | \quad (2.24)$$

with  $\alpha = |\alpha| e^{i\theta}$  being complex due to the non-Hermitian properties of the annihilation operator. We can then expand the coherent state into a basis of number states

$$|\alpha\rangle = \sum_{n=0}^{\infty} |n\rangle \langle n|\alpha\rangle = e^{-\frac{1}{2}|\alpha|^2} \sum_{n=0}^{\infty} \frac{\alpha^n}{\sqrt{n!}} |n\rangle \quad (2.25)$$

The number of photons in a coherent state of amplitude  $\alpha$  follows a Poisson distribution

$$P(n) = e^{-|\alpha|^2} \frac{|\alpha|^{2n}}{n!} \quad (2.26)$$

The mean value and variance of the quadratures evaluated at the coherent state are

$$\langle \hat{X}^q \rangle = \alpha + \alpha^* = 2\Re(\alpha) \quad (2.27)$$

$$\langle \hat{X}^p \rangle = -i(\alpha - \alpha^*) = 2\Im(\alpha) \quad (2.28)$$

$$\text{Var}(\hat{X}^q) = \text{Var}(\hat{X}^p) = 1 \quad (2.29)$$

From these relations we see that coherent states feature minimum uncertainty.

### 2.1.3.3 Thermal states

A harmonic oscillator in thermal equilibrium with its environment at temperature  $T$  is described by a thermal state. Both photons and phonons follow a bosonic statistics described by an occupancy probability

$$p(n) = \exp\left(-n \frac{\hbar\omega}{k_B T}\right) \left[1 - \exp\left(-\frac{\hbar\omega}{k_B T}\right)\right] \quad (2.30)$$

The mean occupancy and variance of the oscillator are given by

$$\langle \hat{n} \rangle = \sum_{n=0}^{\infty} n p(n) = \left[ \exp\left(\frac{\hbar\omega}{k_B T}\right) - 1 \right]^{-1} \quad (2.31)$$

$$\text{Var}(\hat{n}) = \langle \hat{n}^2 \rangle - \langle \hat{n} \rangle^2 \quad (2.32)$$

At room temperature, the *classical limit* approximation  $k_B T \gg \hbar\omega$  is usually satisfied for mechanical oscillators and we have

$$\langle n \rangle_{k_B T \gg \hbar\omega} = \frac{k_B T}{\hbar\omega} \quad (2.33)$$

On the other hand, near-infrared light has usually a frequency in the order of  $\omega/2\pi \approx 10^{14}$ , hence a thermal occupancy of  $\langle n \rangle \approx 10^{-35}$ . The optical field is then in its ground state at room temperature. Thermal states represent mixed states and can be described by a density matrix  $\hat{\rho}$  which in the number-state basis appears as

$$\hat{\rho} = \sum_{n=0}^{\infty} \frac{\langle \hat{n} \rangle^n}{(1 + \langle \hat{n} \rangle)^{n+1}} |n\rangle \langle n| \quad (2.34)$$

As the expectation value of an operator  $\hat{O}$  for a state described by a density matrix is given by  $\langle \hat{O} \rangle = \text{Tr}(\rho \hat{O})$ , the expectation value and variance of the quadrature operator are given by

$$\langle \hat{X}^\theta \rangle = 0 \quad (2.35)$$

$$\text{Var}(\delta \hat{X}^\theta) = \langle n \rangle + \frac{1}{2} \quad (2.36)$$

## 2.2 Modulation of the light

### 2.2.1 Phase modulation

A single-frequency laser can be modeled as a monochromatic scalar light field  $\alpha(t) = \alpha_0 e^{i\omega_0 t}$  of amplitude  $\alpha_0$  and frequency  $\omega_0$ . A harmonic phase modulation at frequency  $\omega_m$  can then be modeled as

$$\alpha_{PM}(t) = \alpha(t) e^{i\beta \cos(\omega_m t)} \quad (2.37)$$

with *beta* being the modulation depth. This can be expanded using some known relations on the Bessel functions  $J_j(M)$  of order  $j$

$$e^{i\beta \cos \theta} = \sum_{j=-\infty}^{\infty} i^j J_j(M) e^{ij\theta} \quad (2.38)$$

$$J_j(M) = \sum_{l=1}^{\infty} \frac{(-1)^l}{l!(l+j)} \left(\frac{M}{2}\right)^{j+2l} \quad (2.39)$$

For a small modulation depth, the phase-modulated field can be written as

$$\alpha_{PM}(t) \approx \alpha_0 e^{i\omega_0 t} [J_0(M) + iJ_1(M)e^{i\omega_m t} + iJ_1(M)e^{-i\omega_m t}] = \alpha_0 e^{i\omega_0 t} \left[ 1 + i\frac{M}{2} (e^{i\omega_m t} + e^{-i\omega_m t}) \right] \quad (2.40)$$

As we can see from Eq. 2.40 phase-modulated light presents three components: an unmodulated carrier at frequency  $\omega_0$  and two sidebands at frequency  $\omega_0 \mp \omega_m$ .

### 2.2.2 Frequency modulation

Frequency modulation induces a similar effect as phase modulation. As frequency  $\nu$  is defined as derivative of the phase  $\theta$

$$\nu = \frac{\omega}{2\pi} = \frac{d\theta}{dt} \quad (2.41)$$

A sinusoidal frequency modulation is then described as

$$\omega = M' \sin(\omega_m t) \quad (2.42)$$

and induces a phase shift

$$\theta = \int M' \sin(\omega_m t) dt = -\frac{M'}{\omega_m} \cos(\omega_m t) \quad (2.43)$$

### 2.2.3 Amplitude modulation

Sinusoidal amplitude modulation of a light field can be expressed as

$$\alpha_{AM}(t) = \alpha(t) (1 + M \cos(\omega_m t)) = \alpha_0 e^{i\omega_0 t} \left[ 1 + \frac{M}{2} (e^{i\omega_m t} + e^{-i\omega_m t}) \right] \quad (2.44)$$

Attenuation can be represented as an amplitude modulation as well, in which case we obtain

$$\alpha_{AM}(t) = \alpha(t) \left[ 1 - \frac{M}{2} (1 - \cos(\omega_m t)) \right] = \alpha_0 e^{-i\omega_0 t} \left[ 1 - \frac{M}{2} + \frac{M}{4} (e^{i\omega_m t} + e^{-i\omega_m t}) \right] \quad (2.45)$$

## 2.3 Power spectral density

Modulating the phase or amplitude of the light produces sidebands around its carrier and represents a way to imprint information into the light field itself. The subject of this work consists in the detection of such fluctuations in the frequency domain. The specific object that we will deal with is called *power spectral density* (PSD) and describes the noise intensity at a specific frequency. For an operator  $\hat{O}$ , the PSD is the limit of its autocorrelation function

$$S_{OO}(\omega) \equiv \lim_{\tau \rightarrow \infty} \frac{1}{\tau} \langle \hat{O}_\tau^\dagger(\omega) \hat{O}_\tau(\omega) \rangle \quad (2.46)$$

where  $\hat{O}_\tau(\omega)$  is the Fourier transform of  $O(t)$  over a time interval  $(-\tau/2; \tau/2)$ . The Fourier transform  $\mathcal{F}$  is defined as

$$O(\omega) = \mathcal{F}(O(t)) = \int_{-\infty}^{\infty} O(t) e^{i\omega t} dt \quad (2.47)$$

while the inverse Fourier transform is given by

$$O(t) = \mathcal{F}^{-1}(O(\omega)) = \frac{1}{2\pi} \int_{-\infty}^{\infty} O(\omega) e^{-i\omega t} d\omega \quad (2.48)$$

Please note that the integration to infinity represents the limit of the window Fourier transform

$$O_\tau(\omega) = \int_{-\tau/2}^{\tau/2} O(t) e^{i\omega t} dt \quad (2.49)$$

Using the Wiener-Khinchin theorem, we can link the autocorrelation function to the power spectral density and obtain

$$S_{OO}(\omega) = \int_{-\infty}^{\infty} e^{i\omega\tau} \langle \hat{O}^\dagger(\tau) \hat{O}(0) \rangle d\tau \quad (2.50)$$

$$S_{O^\dagger O^\dagger}(\omega) = \int_{-\infty}^{\infty} e^{i\omega\tau} \langle \hat{O}(\tau) \hat{O}^\dagger(0) \rangle d\tau \quad (2.51)$$

Please note that  $S_{OO}(\omega)$  and  $S_{O^\dagger O^\dagger}(\omega)$  are always real.

## 2.4 Optomechanical interaction

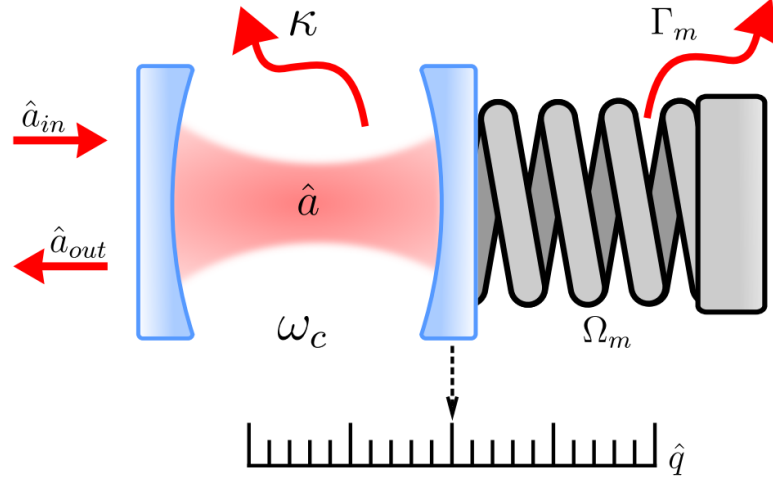


Figure 2.1: Schematic of a typical optomechanical system. An optical field  $\hat{a}_{in}$  of angular frequency  $\omega_L$  enters a cavity of resonance frequency  $\omega_c$  and linewidth  $k$ . The intracavity field  $\hat{a}$  exerts a radiation pressure onto the mirror connected to a mechanical oscillator of angular frequency  $\Omega_M$  and damping rate  $\Gamma_M$ . The resulting displacement  $\hat{q}$  is transduced onto the light and can be readout through the detection of the output field  $\hat{a}_{out}$ .

An optomechanical system can typically be modeled as a linear optical cavity with one mirror connected to a spring so that the radiation pressure acting on such mirror will drive a mechanical oscillation in the direction parallel to the cavity axis. The corresponding physics is ruled by the Hamiltonian

$$\hat{H} = \frac{m_{eff}\Omega_M^2\hat{q}^2}{2} + \frac{\hat{p}^2}{2m_{eff}} + \hbar\omega_c\hat{a}^\dagger\hat{a} \quad (2.52)$$

The first two terms of Eq. 2.52 denote the Hamiltonian of a mechanical oscillator of mass  $m_{eff}$  and resonance frequency  $\Omega_M$  while the last describes the intracavity field of frequency  $\omega_c$  and decay rate  $k$ . This picture does not include any interaction between the mechanical motion and the optical field, which can instead be included by considering the deformation of the cavity due to the oscillator displacement  $\hat{q}$ . As a matter of fact, we can describe the cavity resonance frequency as  $\omega_c = \omega_c(\hat{q})$ , thus taking into account the parametric coupling between the mechanical and optical resonators. We carry out the Taylor expansion  $\omega_c(\hat{q}) \approx \omega_c + \hat{q}\frac{\partial\omega_c}{\partial\hat{q}} + \dots$ . Considering small mirror displacements compared to the cavity length  $L$ , such that we can truncate terms after the first order, we have

$$\omega_c(\hat{q}) \approx \omega_c + \frac{\partial\omega_c}{\partial\hat{q}}\hat{q} \quad (2.53)$$

For a Fabry-Perot cavity, we have  $\frac{\partial\omega_c}{\partial\hat{q}} = \frac{\omega_c}{L}$ . As this derivative quantifies the strength of interaction between the two resonators, we see that working with small cavities tends to present an advantage. We can then rewrite the optical term of the Hamiltonian as

$$\hbar\omega_c\hat{a}^\dagger\hat{a} \approx \hbar\left(\omega_c + \frac{\partial\omega_c}{\partial\hat{q}}\hat{q}\right)\hat{a}^\dagger\hat{a} = \hbar\omega_c\hat{a}^\dagger\hat{a} + g_0\hat{a}^\dagger\hat{a}\left(\hat{b} + \hat{b}^\dagger\right) \quad (2.54)$$

where the definition of the position operator  $\hat{q} = x_{zpf} (\hat{b} + \hat{b}^\dagger)$  was recalled and the single-photon optomechanical coupling rate  $g_0 = \frac{\partial \omega_c}{\partial q} x_{zpf}$  was defined.

### 2.4.1 Driven Hamiltonian in a rotating frame

As the optomechanical coupling is much smaller than the other rates of the system, the optomechanical interaction is boosted by optical feedback of the cavity. It is then convenient to move the system into a reference frame rotating at the frequency  $\omega_L/2\pi$  of the input laser, thus canceling the fast-oscillating terms in the Hamiltonian. This corresponds to a unitary transformation

$$\hat{H} \rightarrow \hat{U} \left( \hat{H} - i\hbar \frac{\partial}{\partial t} \right) \hat{U}^\dagger \quad (2.55)$$

where  $\hat{U} = e^{i\omega_c t \hat{a}^\dagger \hat{a}}$ . In the rotating frame, the Hamiltonian will then be

$$\hat{H}' = \hbar\Omega_M \hat{b}^\dagger \hat{b} + \hbar\Delta_0 \hat{a}^\dagger \hat{a} + \hbar g_0 \hat{a}^\dagger \hat{a} (\hat{b} + \hat{b}^\dagger) + \hbar E (\hat{a}^\dagger + \hat{a}) \quad (2.56)$$

where the detuning  $\Delta_0 = \omega_c - \omega_L$  and the driving strength  $E = \sqrt{2Pk/\hbar\omega_L}$  (with  $P$  being the input laser power) were defined. In this framework, the radiation pressure exerted by the photon momentum transfer onto the mechanical resonator results in a force

$$\hat{F} = \frac{d\hat{H}'}{d\hat{q}} = \hbar \frac{\partial \omega_c}{\partial q} \hat{a}^\dagger \hat{a} = \hbar \frac{g_0}{x_{zpf}} \hat{a}^\dagger \hat{a} \quad (2.57)$$

### 2.4.2 Quantum Langevin equations of motion

The dynamics of an open optomechanical system is described by the Langevin equations of motion, stochastic equations containing both damping rates and random forces. Based on the fluctuation-dissipation theorem, the mechanical resonator motion is constantly damped with rate  $\Gamma_M$  and driven by a stochastic force defining a noise operator  $\hat{\xi}$  of zero mean value. The noise operator satisfies the condition

$$\langle \xi(t) \xi(t') \rangle = \frac{\Gamma_M}{\Omega_M} \int \frac{d\omega}{2\pi} e^{-i\Omega(t-t')} \Omega \left[ \coth \left( \frac{\hbar\Omega}{2k_B T} \right) + 1 \right] \quad (2.58)$$

and it is non-Markovian, that is to say *delta*-correlated. In the classical limit  $k_B T \ll \hbar\Omega$ , Eq. 2.58 can be written as

$$\langle \xi(t) \xi(t') \rangle = \Gamma_M [(2n_{th} + 1) \delta(t - t')] \quad (2.59)$$

In a similar fashion, the intracavity field is subject to a decay rate  $k$  and is excited by the input-field radiation pressure, represented by an annihilation operator  $\hat{a}_{in}$ , defined by the correlations

$$\langle \hat{a}_{in}(t) \hat{a}_{in}^\dagger(t') \rangle = (N(\omega_c) + 1) \delta(t - t') \approx \delta(t - t') \quad (2.60)$$

$$\langle \hat{a}_{in}^\dagger(t) \hat{a}_{in}(t') \rangle = N(\omega_c) \delta(t - t') \approx 0 \quad (2.61)$$

where the thermal occupancy of the optical field  $N(\omega_c)$  was assumed null as stated previously. Using the system Hamiltonian and the Heisenberg equation of motion  $\frac{\partial}{\partial t}\hat{O} = -\frac{i}{\hbar}[\hat{O}, \hat{H}] + \hat{N}$  with  $\hat{N}$  being a noise operator, we can derive the quantum Langevin equations of motion

$$\dot{\hat{a}} = -(k + i\Delta_0)\hat{a} + ig_0\hat{a}\hat{q} + E + \sqrt{2k}\hat{a}_{in} \quad (2.62)$$

$$\dot{\hat{q}} = \Omega_M\hat{p} \quad (2.63)$$

$$\dot{\hat{p}} = -\Omega_M\hat{q} - \Gamma_M\hat{p} + g_0\hat{a}^\dagger\hat{a} + \hat{\xi} \quad (2.64)$$

The optical input field is typically inhabited by a coherent population, such that its amplitude is  $\alpha_{in}\langle\hat{a}_{in}\rangle \neq 0$ . Many channels contribute to the cavity damping, some related to losses of the cavity incoupling/outcoupling port  $k_{ex}$  and some due to intrinsic phenomena such as absorption or scattering  $k_0$ . Since the field inducing intrinsic losses  $\hat{a}_{vac}$  is in a vacuum state ( $\langle\hat{a}_{vac}\rangle = 0$ ), we obtain

$$\sqrt{2k}\hat{a}_{in} \rightarrow \sqrt{2k_{ex}}\hat{a}_{in} + \sqrt{2k_0}\hat{a}_{vac} \quad (2.65)$$

### 2.4.3 Semi-classical dynamics

This picture can be simplified when considering an intense intracavity field, such that the system can be considered to be in a semi-classical steady state. The optical field operator can then be broken down into the sum of a large mean value and small fluctuation  $\hat{a} \rightarrow \alpha_s + \delta\hat{a}$ . The steady state can be found by setting the time derivatives of the Langevin equations to zero, which yields

$$q = \frac{g_0|\alpha_s|^2}{\Omega_M} \quad (2.66)$$

$$\alpha_s = \frac{E}{k + i\Delta} \quad (2.67)$$

The bright intracavity field then changes the equilibrium position of the mechanical oscillator and consequently the detuning into an effective value  $\Delta$

$$\Delta = \Delta_0 - \frac{g_0^2|\alpha_s|^2}{\Omega_M} \quad (2.68)$$

Considering the fluctuations of the operators around their steady state values, the Langevin equations can be rewritten in terms of Hermitian amplitude  $\hat{X}$  and phase  $\hat{Y}$  quadrature operators

$$\delta\hat{X} \equiv (\delta\hat{a} + \delta\hat{a}^\dagger)/\sqrt{2} \quad (2.69)$$

$$\delta\hat{Y} \equiv (\delta\hat{a} - \delta\hat{a}^\dagger)/i\sqrt{2} \quad (2.70)$$

$$\delta\hat{X}_{in} \equiv (\delta\hat{a}_{in} + \delta\hat{a}_{in}^\dagger)/\sqrt{2} \quad (2.71)$$

$$\delta\hat{Y}_{in} \equiv (\delta\hat{a}_{in} - \delta\hat{a}_{in}^\dagger) / i\sqrt{2} \quad (2.72)$$

with  $\hat{X}_{in}$  and  $\hat{Y}_{in}$  bein the corresponding Hermitian input noise operators. Negleting nonlinear terms, we finally obtain our linearised equations

$$\delta\dot{\hat{X}} = -k\delta\hat{X} + \Delta\delta\hat{Y} + \sqrt{2k}\hat{X}_{in} \quad (2.73)$$

$$\delta\dot{\hat{Y}} = -k\delta\hat{Y} - \Delta\delta\hat{X} + g\delta\hat{q} + \sqrt{2k}\hat{Y}_{in} \quad (2.74)$$

$$\delta\dot{\hat{q}} = \Omega_M\delta\hat{p} \quad (2.75)$$

$$\delta\dot{\hat{p}} = -\Omega_M\delta\hat{q} - \Gamma_M\delta\hat{p} + g\delta\hat{X} + \hat{\xi} \quad (2.76)$$

where the effective optomechanical coupling  $g = g_0\sqrt{2}\alpha_s$  was introduced.

#### 2.4.4 On-resonance driving

We will now focus on the case of a driving field on resonance with the cavity, such that  $\Delta = 0$ . This induces a decoupling of the optical amplitude with respect to the phase. On the other hand, mechanical phase and amplitude remain coupled and Eqs. 2.75 and Eq.2.76 can be turned into a single differential equation

$$\delta\ddot{\hat{q}} + \Gamma_M\delta\dot{\hat{q}} + \Omega_M^2\hat{q} = \Omega_M\hat{\xi} - g\Omega_M\delta\hat{X} \quad (2.77)$$

This set of equations can be easily solved in the frequency domain, obtaining

$$\delta\hat{X}(\Omega) = \frac{\sqrt{2k}\hat{X}_{in}(\Omega)}{k - i\Omega} \quad (2.78)$$

$$\delta\hat{Y}(\Omega) = \frac{\sqrt{2k}\hat{Y}_{in}(\Omega) + 2g\delta\hat{q}(\Omega)}{k - i\Omega} \quad (2.79)$$

$$\delta\hat{q}(\Omega) = \chi_M(\Omega) \left( \hat{\xi}(\Omega) + \frac{2g\sqrt{2k}\delta\hat{X}(\omega)}{k - i\Omega} \right) \quad (2.80)$$

with  $\chi_M(\Omega)$  being the *mechanical susceptibility*

$$\chi_M(\Omega) = \frac{\Omega_M}{\Omega_M^2 - \Omega^2 + i\Gamma_M\Omega} \quad (2.81)$$

with a bit of algebra we obtain

$$\delta\hat{q}(\Omega) = \chi_M(\Omega) \left( \hat{\xi}(\Omega) - \sqrt{4\Gamma_M C_{eff}} \hat{X}_{in}(\Omega) \right) \quad (2.82)$$

where the *effective optomechanical cooperativity* was defined

$$C_{eff}(\Omega) \equiv \frac{4g^2/k\Gamma_M}{(1 - 2i\Omega/k)^2} \quad (2.83)$$

The quantity  $C = 4g^2/k\Gamma_M$  is usually referred to simply as *optomechanical cooperativity*.

#### 2.4.5 Mechanical power spectral density

Assuming the optical and mechanical baths as uncorrelated, we can derive the power spectral density of the mechanical displacement operator from Eq. 2.82

$$S_{qq}(\Omega) = \int_{-\infty}^{\infty} \langle \delta\hat{q}(\Omega)\delta\hat{q}(\Omega') \rangle d\Omega' = 2\Gamma_M |\chi_M(\Omega)|^2 [n_{th} + 1 + 2|C_{eff}(\Omega)| S_{x_{in}x_{in}}] \quad (2.84)$$

where the following correlation relations have been taken into account

$$\langle \hat{\xi}(\Omega)\hat{\xi}(\Omega') \rangle = 2\Gamma_M(n_{th} + 1)\delta(\Omega + \Omega') \quad (2.85)$$

$$\langle \hat{\xi}(-\Omega)\hat{\xi}(\Omega') \rangle = 2\Gamma_M(n_{th} + 1)\delta(\Omega - \Omega') \quad (2.86)$$

The first term in Eq. 2.84 stems from the thermal bath driving of spectrum

$$S_{FF}^{th}(\Omega) = \int_{-\infty}^{\infty} \langle \hat{\xi}(\Omega)\hat{\xi}(\Omega') \rangle d\Omega' = 2\Gamma_M(n_{th} + 1) \quad (2.87)$$

while the second term is due to the optical-field backaction which drives the mechanical oscillator. The corresponding back-action power spectral density is

$$S_{FF}^{ba}(\Omega) = 4\Gamma_M \frac{C}{1 - (\Omega/k)^2} = 4\Gamma_M |C_{eff}(\Omega)| \quad (2.88)$$

The power spectral density of the mechanical displacement can then be rewritten as

$$S_{qq}(\Omega) = |\chi_M(\Omega)|^2 (S_{FF}^{th}(\Omega) + S_{FF}^{ba}(\Omega)) \quad (2.89)$$

#### 2.4.6 Input-output relation

Although the intracavity field drives the optomechanical interaction, it is not directly accessible. Therefore a relation linking it to the output field of the cavity is needed, so that we can measure the latter and extract information on the mechanical motion. For a single sided-cavity, the so called *input-output relation* can be used

$$\hat{a}_{out} = \sqrt{2k}\delta\hat{a}(t) - \hat{a}_{in}(t) \quad (2.90)$$

which transforms the field amplitude and phase quadratures into

$$\hat{X}_{out} = \sqrt{2k}\delta\hat{X}(t) - \hat{X}_{in}(t) \quad (2.91)$$

$$\hat{Y}_{out} = \sqrt{2k}\delta\hat{Y}(t) - \hat{Y}_{in}(t) \quad (2.92)$$

$$\delta\hat{X}_{out} = -\frac{k+i\Omega}{k-i\Omega}\hat{X}_{in} \quad (2.93)$$

$$\delta\hat{Y}_{out} = -\frac{k+i\Omega}{k-i\Omega}\hat{Y}_{in} - 2\sqrt{\Gamma_M C_{eff}(\Omega)}\delta\hat{q}(\Omega) \quad (2.94)$$

The last equation can be rewritten as

$$\delta\hat{Y}_{out} = -\frac{k+i\Omega}{k-i\Omega}\hat{Y}_{in} - 2\sqrt{\Gamma_M C_{eff}(\Omega)}\chi_M(\Omega) \left[ \hat{\xi}(\Omega) + 2\sqrt{\Gamma_M C_{eff}(\Omega)}\hat{X}_{in}(\Omega) \right] \quad (2.95)$$

For an on-resonance driving ( $\Delta = 0$ ), information on the mechanical displacement is imprinted onto the phase quadrature of the output field at a characteristic measurement rate

$$\mu = \Gamma_M |C_{eff}(\Omega_M)| = \Gamma_M \frac{C}{1 + (2\Omega_M/k)^2} \quad (2.96)$$

In the sideband unresolved regime ( $k \ll \Omega_M$ ) we can use the approximation  $\mu = 4g^2/k$ , while in the sideband resolved regime, where  $\Omega/k \rightarrow \infty$ , the measurement rate tends to 0 and the information imprinted onto the light phase becomes asymptotically small. As we will see, optomechanical feedback cooling relies on the assumption that the measurement rate is larger than the thermal decoherence rate  $\gamma = \Gamma_M n_{th}$ .

Using a phase-sensitive scheme to detect the output field of the cavity allows to infer information on the mechanical displacement. This was done in our experiments through homodyne detection. The detected mechanical motion fluctuations are then given by

$$\delta\hat{q}_{det} \equiv \frac{\hat{Y}_{out}(\Omega)}{2\sqrt{\Gamma_M C_{eff}(\Omega)}} = \delta\hat{q}_0(\Omega) - \frac{1}{2\sqrt{\Gamma_M C_{eff}(\Omega)}} \left( \frac{k+i\Omega}{k-i\Omega} \right) \hat{Y}_{in}(\Omega) - 2\sqrt{\Gamma_M C_{eff}(\Omega)}\chi_M(\Omega)\hat{X}_{in}(\Omega) \quad (2.97)$$

The right side of Eq. 2.97 presents three contributions: one given by the mechanical motion, one arising from phase fluctuations in the input-field phase and one stemming from back-action noise of the probe amplitude quadrature.

## 3 Experimental techniques

It is about time we complement this beautiful fairy tale of our theoretical framework with some experimental techniques to test its adherence to reality. We will start with direct photodetection techniques, then move to the homodyne-detection scheme we used to probe the interaction between our mechanical and optical resonators. We will go through their working principles and describe their practical implementation, along with the necessary characterization measurements. Later on, we will cover the techniques for a thorough characterization of the optical and the mechanical resonators considered individually. After describing how the modulation depth of the electro-optic modulator in our setup was measured, experimental techniques for the estimate of the single-photon coupling rate will be presented.

### 3.1 Photodetection

#### 3.1.1 Direct detection

The intensity of a light beam can be measured by a photodetector. More specifically, in our lab we use *photodiodes*, based on a semiconductor p-n junction converting an optical signal into an electronic one. To good approximation their behaviour is linear, as the current generated is directly proportional to the incident power through a constant *responsivity* expressed in A/W. Alternatively, the dimensionless *quantum efficiency* can be used, describing the number of emitted electrons per incident photon.

In our experiments, we used commercial photodiodes from Thorlabs, for both characterization measurements and frequency-locking. A PDA50B2 Ge switchable-gain amplified detector was employed for cavity alignment and characterization of the time spectrum in transmission due to its large chip size. An APD430C/M InGaAs variable-gain avalanche photodetector was used in Pound–Drever–Hall schemes to lock the frequency of the probing light beam to our optical cavities. The choice of this particular device was due to its larger bandwidth with respect to the PDA50B2 model and to the low electronic noise of the built-in amplifier. In measurements featuring an auxiliary laser operated simultaneously with the probing one, a PDA10CF-EC InGaAs fixed-gain amplified detector was used for side-of-fringe locking of its frequency to the cavity.

#### 3.1.2 Homodyne detection

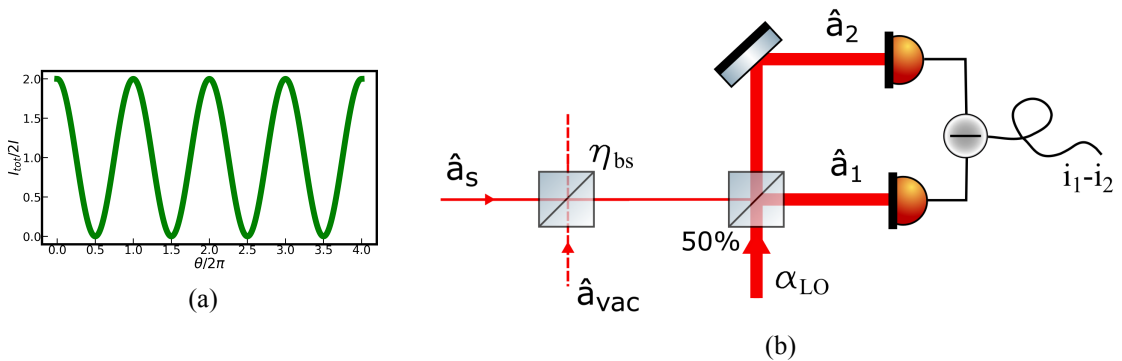


Figure 3.1: a) Interference between two fields of intensity  $I$  as a function of their phase difference  $\theta$ . b) Homodyne detection scheme. The difference-current output of the detector is proportional to the quadrature variables of the incoming field  $\hat{a}_s$ . Non-ideal detection efficiency is modeled by a fictitious beamsplitter of transmittance  $\eta_{bs}$  in the signal beam.

Unlike intensity, the phase of a light field is not directly accessible through measurement with a device. Hence, more convoluted detection schemes must be employed. In our measurements we use *balanced homodyne detection* [18, 19, 20] to obtain information on the mechanical motion, whose amplitude quadrature is transcribed onto the phase of intracavity light. When a weak electromagnetic field is spatially overlapped and interfered with a phase-coherent, much more intense one, shining their light onto a photodiode allows to reconstruct the interference pattern as a function of their phase difference  $\theta$  (see Fig. 3.1a). Instead if this overlap beam meets a 50/50 beamsplitter and the two outputs are focused onto separate—ideally identical—photodiodes, the resulting photocurrents can be subtracted. This provides an electronic signal which carries information on an arbitrary quadrature  $q_\theta$  depending on the phase difference. A sketch of how homodyne detection works is presented in Fig. 3.1b.

Let us now briefly establish how a homodyne scheme can be modeled. Two spatially-overlapping electromagnetic-field modes  $\hat{a}_1$  and  $\hat{a}_2$  meet a beamsplitter on their path and they are both transmitted with transmittance  $T$  and reflected with reflectance  $R = 1 - T$ . The new modes  $\hat{a}'_1$  and  $\hat{a}'_2$  emerging from the optical component will be described by

$$\begin{pmatrix} \hat{a}'_1 \\ \hat{a}'_2 \end{pmatrix} = \begin{pmatrix} \sqrt{T} & \sqrt{1-T} \\ -\sqrt{1-T} & \sqrt{T} \end{pmatrix} \begin{pmatrix} \hat{a}_1 \\ \hat{a}_2 \end{pmatrix} \quad (3.1)$$

Given a 50/50 beamsplitter, we have  $T = 1/2$ . The signal beam is described by the operator  $\hat{a}_s$ , while the local oscillator (LO) has a much stronger intensity and is usually described as a purely classical object  $|\alpha_{LO}| e^{i\theta}$ . The two modes emerging from the beamsplitter will then be

$$\hat{a}'_1 = \frac{1}{\sqrt{2}} \left( |\alpha_{LO}| e^{i\theta} + \hat{a}_s \right) \quad (3.2a)$$

$$\hat{a}'_2 = \frac{1}{\sqrt{2}} \left( |\alpha_{LO}| e^{i\theta} - \hat{a}_s \right) \quad (3.2b)$$

and after impinging on separate photodiodes they will generate photocurrents  $i_{1,2} \propto n_{1,2} = (\hat{a}'_{1,2})^\dagger \hat{a}'_{1,2}$  with their difference  $i_-$  being

$$i_- = i_1 - i_2 \propto (\hat{a}'_1)^\dagger \hat{a}'_1 - (\hat{a}'_2)^\dagger \hat{a}'_2 = |\alpha_{LO}| \left( \hat{a}_s e^{-i\theta} + \hat{a}_s^\dagger e^{i\theta} \right) = \sqrt{2} |\alpha_{LO}| \hat{q}_{s,\theta} \quad (3.3)$$

Eq. 3.3 shows the fluctuations of the homodyne signal are proportional to both the local oscillator amplitude and the signal field quadrature. This result only holds if the two detection arms are perfectly balanced. Such condition causes the  $|\alpha_{LO}|^2$  terms to cancel each other in the difference photocurrent, hence canceling out the local oscillator classical noise in the two arms.

Please bear in mind that any quantum measurement is deeply influenced by losses, as these tend to degrade quantum states. Hence it is extremely important to model losses properly and this is usually done by a beamsplitter model. When a field crosses a beamsplitter of transmittance  $\eta_{bs}$ , its intensity is diminished by a factor  $1 - \eta_{bs}$  while the signal is mixed with a fraction  $1 - \eta_{bs}$  of the the input from the other port. This happens even when no light, i.e. a vacuum mode, is shone onto the other port. The difference photocurrent will reflect such behaviour, showing a contribution proportional to the vacuum quadrature  $\hat{q}_v$

$$i_- \propto \sqrt{2} |\alpha_{LO}| \left( \sqrt{\eta_{bs}} \hat{q}_{s,\theta} + \sqrt{1 - \eta_{bs}} \hat{q}_v \right) \quad (3.4)$$

Many sources of loss—for example photodiode inefficiencies—can be modeled in this way, since they bring about the same effect on the homodyne signal.

### 3.1.2.1 Homodyne setup

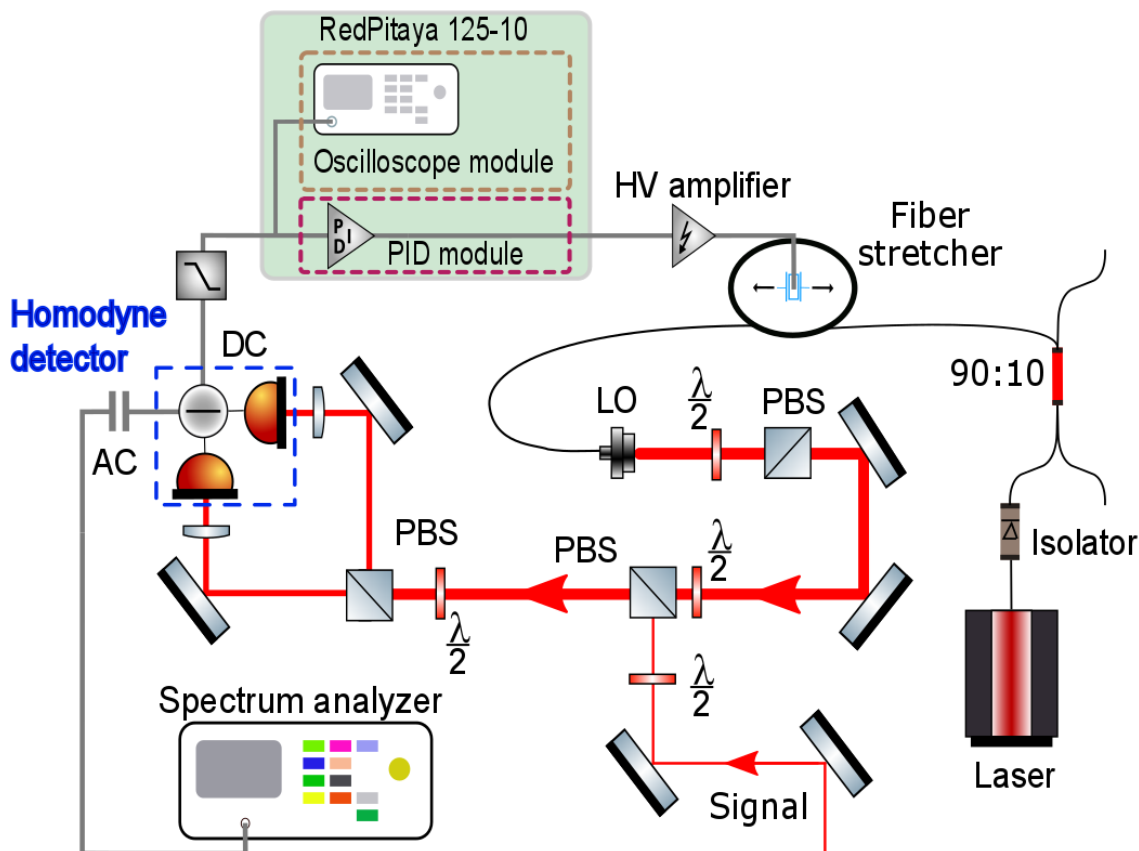


Figure 3.2: Our implementation of a homodyne detection scheme.

Fig. 3.2 displays how we implemented a homodyne detection scheme for our experiments. Light coming from our laser goes through a fiber optical isolator, then a fiber beamsplitter so that 90% of the optical power is deployed as local oscillator. After outcoupling into free space, a half-wave plate is used in combination with a PBS for power regulation, then this local oscillator is spatially overlapped with our signal field on a second PBS. It is important to highlight that while the signal beam is reflected off the PBS surface, the local oscillator will pass through it—waveplates were used again to maximize reflection and transmission, respectively. As a consequence, these beams have perpendicular polarization in the output port and they do not interfere. As one last half-wave plate rotates both polarizations by  $\frac{\pi}{4}$  and a PBS splits the power in two beams of equal intensity, interference is produced. The PBS outputs are then focused onto the different diodes of our homodyne detector and the resulting photocurrents are subtracted directly on the detector circuit board. A simplified schematic of our homodyne detector is presented in Fig. 3.3. A high-pass filter separates the DC part of the difference photocurrent from the AC signal, with the latter providing the input to our spectrum analyzer Keysight N9000B CXA. The DC signal goes through an analog low-pass filter and is then monitored using the oscilloscope hosted by a RedPitaya 125-10 single-board computer. This allows to detect any unbalance with respect to the electronic zero, which can be compensated by rotating the last half-wave plate.

As we see in Eq. 3.3, the homodyne photocurrent carries information about an arbitrary quadrature  $\hat{q}_{s,\theta}$  depending on the relative phase  $\theta$  between local oscillator and optical signal. As in our experiments we want to measure only the phase quadrature of the signal field, a locking scheme

is necessary to fix this relative phase. The DC signal featuring interference fringes is then used as error function and fed to a digital PID-controller hosted by the RedPitaya. The software modules from PyRPL, an open-source, Python-based package are used to run this RedPitaya [21]. Locking to the zero-crossing point of such interference fringes corresponds to locking the relative phase between fields to  $\pi/2$ , thus enabling detection of pure phase quadrature. To achieve this, a fiber stretcher—essentially a fiber coiled around a piezo actuator—placed between the 90/10 fiber beam-splitter and the LO outcoupler is controlled by the PID output. As the error-function value drifts from 0, the controller signal builds up and the fiber is stretched in order to compensate the change in relative phase.

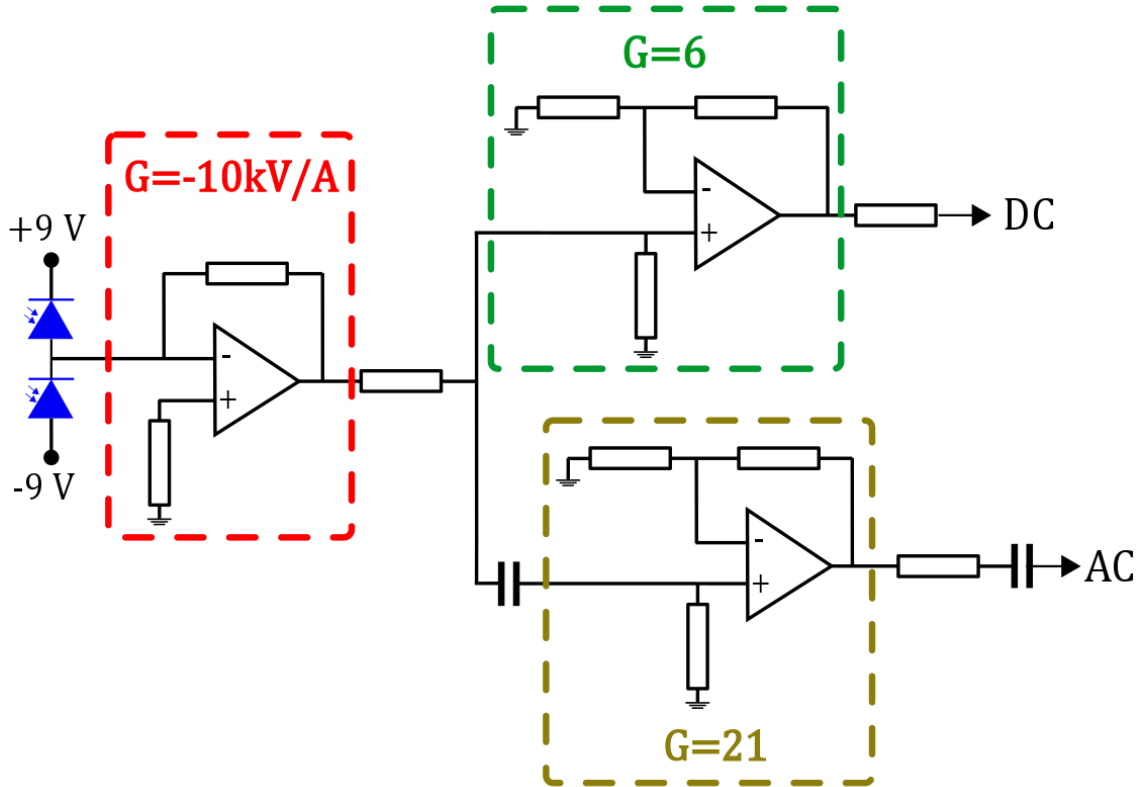


Figure 3.3: Simplified schematic of our homodyne detector. The photodiodes are reverse-biased with 9 V and the photocurrents they generate are subtracted onboard directly. The resulting signal is converted into voltage by a transimpedance operational amplifier with a gain of  $-10 \text{ kV/A}$ . This is split in two and one part is high-pass filtered and then amplified by a non-inverting operational amplifier with a gain of 21. Its output is sent to our spectrum analyzer and represents our measurement signal. The other part contains also the DC signal and it goes through a separate amplification stage (non-inverting operational amplifier with a gain of 6), whose output is fed to a RedPitaya for monitoring and phase locking.

### 3.1.3 Quantum efficiency

We already stressed the role of optical losses in quantum measurements. Photodiodes with low quantum efficiency can represent one of the main sources of loss, as only a fraction of the impinging photons will contribute to the generated photocurrent and be detected. It is then necessary to estimate the quantum efficiency  $\eta_{QE_\lambda}$  (where the subscript  $\lambda$  highlights the wavelength dependency) of the photodiodes used for homodyne detection in order to correctly quantify the overall efficiency of the measurement. This can be done by measuring the responsivity  $R_D$  of our detector, i.e. the photocurrent  $i$  generated per unit of input optical power  $P_0$

$$R_D = \frac{i}{P_0} = \frac{\eta_{QE\lambda} q \lambda}{hc} \quad (3.5)$$

where  $q$  is the elementary electron charge,  $h$  is Planck's constant and  $c$  is the speed of light in vacuum. The transimpedance operational amplifier in our detector (see Fig. 3.3) converts the photocurrent into a voltage  $v_{photo}$  which is then amplified by subsequent op amps. We indicate the overall gain as  $g_D$  and obtain

$$R_D = \frac{v_{photo}}{g_D P_0} = \frac{1}{g_D} \frac{\eta_{QE\lambda} q \lambda}{hc} \quad (3.6)$$

In practice, we send light to one of the two photodiodes in our detector while covering the other and measure the output voltage for different values of the optical power, then repeat for the other photodiode. A simple linear fit allows us to estimate the responsivity, hence the quantum efficiency for each of them. We present an example in Fig. 3.4.

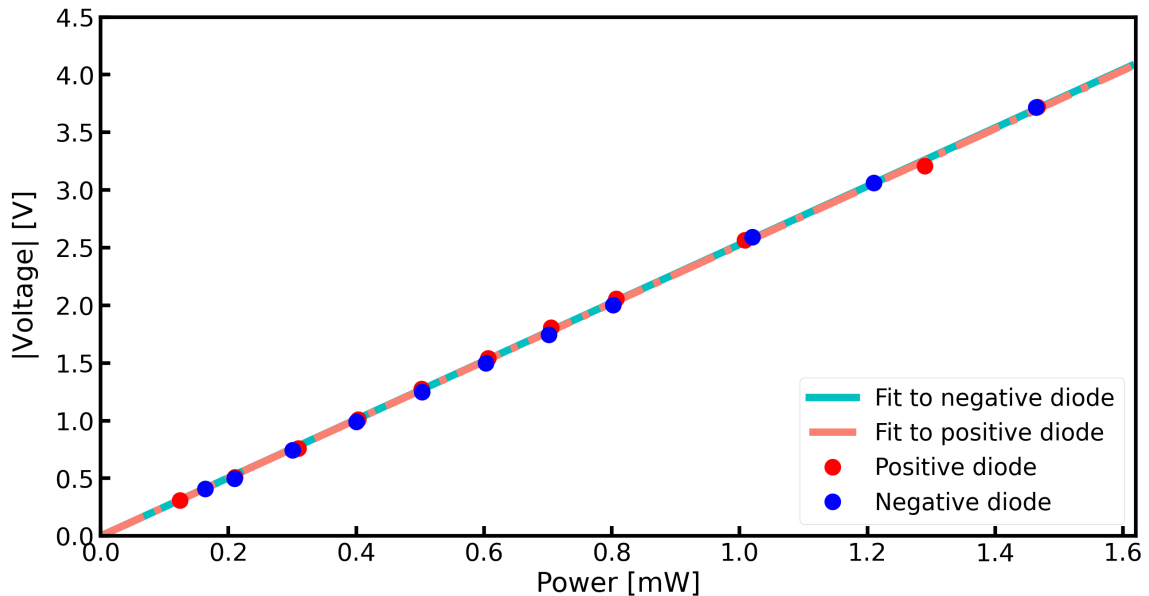


Figure 3.4: Measurement of the responsivity of our homodyne detector's photodiodes. Please note that the absolute value of the output voltage is reported on the y axis. From the slope of the fitting curve, we can extract the quantum efficiency using Eq. 3.6.

In this work, we first used commercial InGaAs photodiodes (Thorlabs FDGA05), featuring a quantum efficiency  $\eta_{QE} = 0.76$  at a wavelength around 1550 nm. These were then replaced by custom-made InGaAs photodiodes with 0.99 quantum efficiency manufactured at the Fraunhofer Heinrich Hertz Institute of Berlin.

### 3.1.3.1 Homodyne visibility

Among the different sources of optical loss affecting homodyne measurements, sub-optimal mode-matching between local oscillator and optical signal deserves a special mention. Even when they can both be described by pure, gaussian TEM<sub>00</sub> modes of the electromagnetic field, small misalignments and differences in mode shape can degrade the beam overlap, hence the interference. This induces an optical loss which in our beamsplitter model is quantified by a transmittance  $\eta_{bs} = \nu^2$ , with  $\nu$  being the *visibility* of the interference fringes

$$\nu = \frac{I_{max} - I_{min}}{I_{max} + I_{min}} \quad (3.7)$$

where  $I_{max}$  ( $I_{min}$ ) represents the maximum (minimum) power of the interference fringes. Down to a deeper physical level, we can think of visibility as a measurement of how much information is transferred from the signal phase to the detector photocurrent after amplification by the LO pump in the homodyne process.

Visibility can be measured experimentally by equating local oscillator and probe power, balancing the homodyne photocurrent for the local oscillator and then finally shining light only on a single photodiode of the homodyne detector. Assuming linear conversion of optical power into electric current, Eq. 3.7 can be rewritten in terms of recorded voltages

$$\nu = \frac{V_{max} - V_{min}}{V_{max} + V_{min}} \quad (3.8)$$

Fitting a cosine function to the experimental data (as shown in Fig.3.5) allows to determine the visibility. Since this value depends on the optical alignment, it is subject to small variations over time and yet its knowledge is very critical to the success of feedback cooling, like all sources of loss. Hence for every dataset presented in the chapter on measurements we will report the corresponding visibility value.

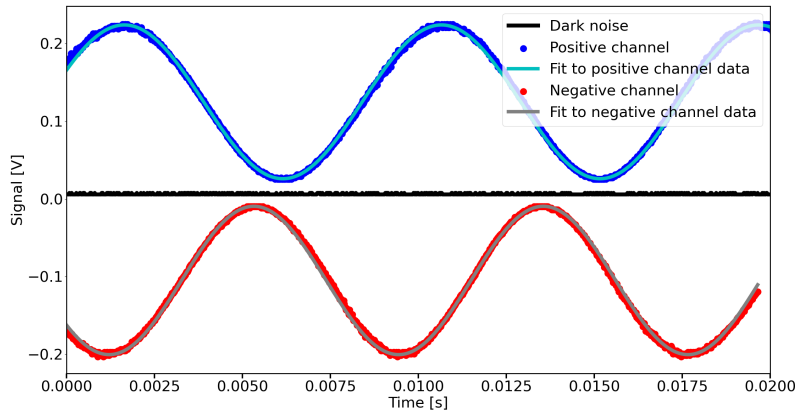
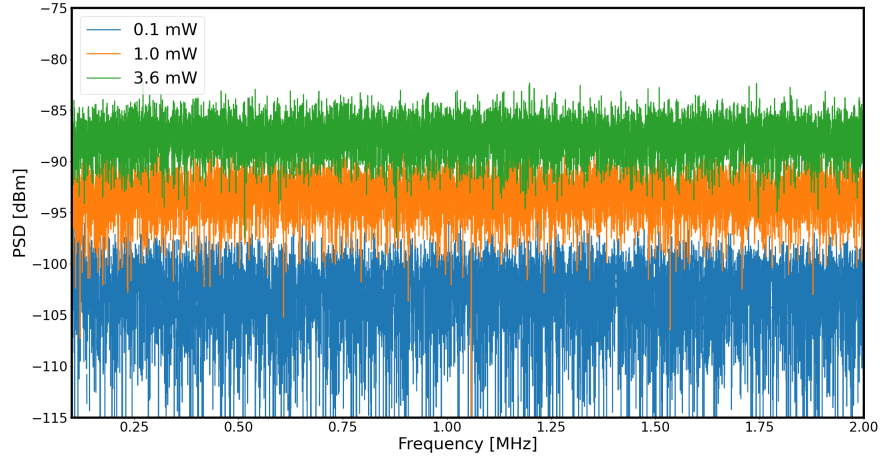


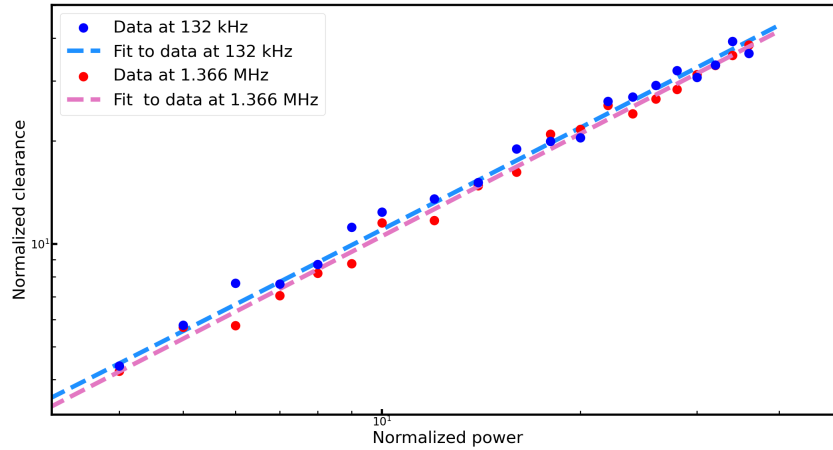
Figure 3.5: Interference visibility recorded on the positive (blue) and negative (red) channel photodiodes of our homodyne detector. The dark noise (black) was subtracted from the voltage values before calculating the visibility.

Most commonly, the signal beam and the local oscillator will not feature the same spatial profile even when both wavefronts have gaussian shape. This tends to reduce the homodyne visibility. A suitable choice of lenses enables to modify the profile of one of the beams and improve the mode overlap (*optical mode-matching*). In our case, we were able to increase the visibility from 0.87 up to 0.96. We will elaborate on this technique later in Sec. 3.3.5, as it plays a vital role in aligning the light path to an optical cavity.

## 3.1.3.2 Shot-noise scaling with optical power



(a)



(b)

Figure 3.6: a) Homodyne measurement of the shot noise. Traces were collected for different values of the local oscillator power. Dark noise was subtracted. b) Shot noise clearance from electronic noise as a function of local oscillator power. Clearance is normalized to the level detected using the lowest local oscillator power, while x-values have been normalized to the minimum local oscillator power.

Let us now take a step back and have a closer look at Eq. 3.4. When no signal is steered into the homodyne-detection setup, vacuum represents its input. In this situation though, only the local oscillator contributes to the detected noise power. The power spectral density related to the difference photocurrent will then scale linearly with the local oscillator intensity.

$$S_{i-i} \propto 2 |\alpha_{LO}|^2 S_{\hat{q}_v \hat{q}_v} \quad (3.9)$$

Equipped with such knowledge, we can now determine whether at a specific frequency our de-

tector's performance is shot-noise limited, i.e. if the shot noise dominates over other sources of noise, such as electronics. In order to do so, a series of measurements was recorded blocking the signal beam and steering only the local oscillator into the homodyne-detection setup. The optical power was increased from an initial value of  $0.1 \mu\text{W}$  up to  $3.6 \text{ mW}$ , while shot-noise traces were recorded with our spectrum analyser, whose resolution bandwidth was set to  $100 \text{ Hz}$ . Examples are shown in Fig. 3.6a. The clearance from dark noise was evaluated by averaging the noise level in a bandwidth of  $10 \text{ kHz}$  around the frequency of interest. In particular, here we focus on the behaviour of our detector at the mechanical frequencies  $132 \text{ kHz}$  and  $1.366 \text{ MHz}$ . Fig. 3.6b displays data obtained by normalizing the local oscillator power to its lowest value and the clearance to the value recorded at the minimum local oscillator power. Fitting these data to a simple linear model, a slope of  $1.09$  and  $1.05$  is extrapolated at  $132 \text{ kHz}$  and  $1.366 \text{ MHz}$ , respectively. This is in agreement with what described by Eq. 3.9, hence we can deduce the performance of our homodyne detector is shot-noise limited. Furthermore, no detector saturation can be observed in 3.6b.

## 3.2 Mechanical resonators

Different kinds of mechanical resonators will be presented in this work, such as the trampolines and phononic membranes shown in Figs. 3.7, all fabricated by our QPIT Research Process Scientist Dennis Høj in our clean room facility DTU Nanolab. In this section, we will explain the general working principles of mechanical resonators and explain what are their relevant physical quantities. We will not provide details about the individual microstructures here, as these will be presented in the next chapter along with the results of our experimental measurements.

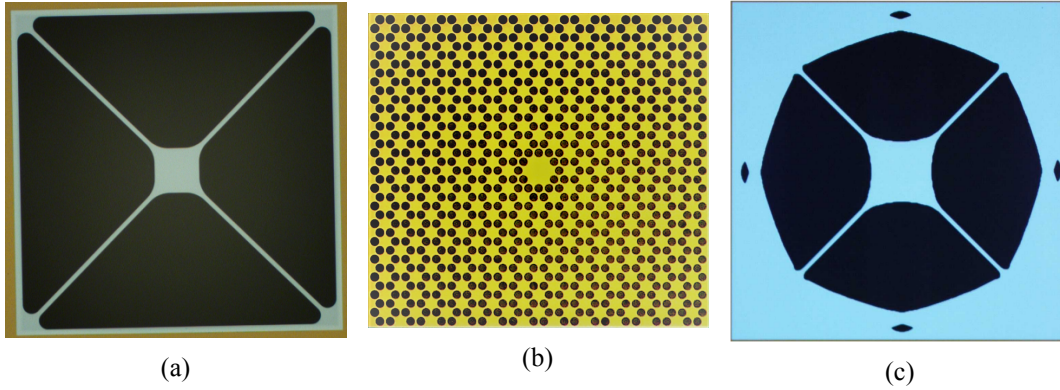


Figure 3.7: The different kinds of mechanical resonators chosen for our feedback cooling experiments. From left to right: a) a tethered membrane (trampoline), b) a phononic membrane and c) a topology-optimized trampoline. Please note in b) the yellow area depicts a  $\text{Si}_3\text{N}_4$  free-standing layer while the black spots are empty holes.

### 3.2.1 Out-of-plane modes

We consider a thin, square membrane, whose out-of-plane modes can be described by a relatively simple model [22] illustrated in Fig. 3.8. If a uniform tensile stress  $\sigma$  is applied, the motion of the resonator is described by a two-dimensional wave equation

$$\frac{D}{h} \nabla^4 w(x, y, t) - \sigma \nabla^2 w(x, y, t) = -\rho \frac{\partial^2}{\partial t^2} w(x, y, t) \quad (3.10)$$

where  $w(x, y, t)$  is the displacement at a given point  $(x, y)$  on the membrane evolving in time  $t$ . Furthermore,  $l$  is the side length of the membrane,  $h$  its thickness and  $\rho$  is the material density. We assume  $h \ll l$ .  $D$  is the flexural rigidity

$$D = \frac{Eh^3}{12(1-\nu^2)} \quad (3.11)$$

with  $E$  being the Young's modulus and  $\nu$  the Poisson's ratio. Eq. 3.10 can be solved by applying the boundary condition that  $w(x, y, t)$  and its derivatives with respect to  $x$  and  $y$  vanish at the edges of the membrane. Separating the variables, we can approximate the solutions as sinusoidal transverse-mode shapes

$$w(x, y, t) \approx q(t) \sin(nkx) \sin(mky) \quad (3.12)$$

where  $k = \pi/l$  and  $m$  and  $n$  are integers indicating the number of antinodes along the  $x$  and  $y$  directions, respectively. The membrane displacement can be described as a 1D harmonic oscillator

$$q(t) = q_0 \cos(\Omega_M t + \phi) \quad (3.13)$$

with  $q_0$  and  $\phi$  representing amplitude and initial phase of the motion, respectively. The mechanical angular frequency  $\Omega_M$  follows the relation

$$\Omega_M^2 = \frac{\pi^2 \sigma}{\rho l^2} (n^2 + m^2) \quad (3.14)$$

Given the mass of the membrane  $m_0 = \rho l^2 h$ , an effective mass  $m_{eff}$  is associated to the mode shape

$$m_{eff} = \rho h \int_0^l \int_0^l \sin^2(nkx) \sin^2(mky) dx dy = \frac{m_0}{4} \quad (3.15)$$

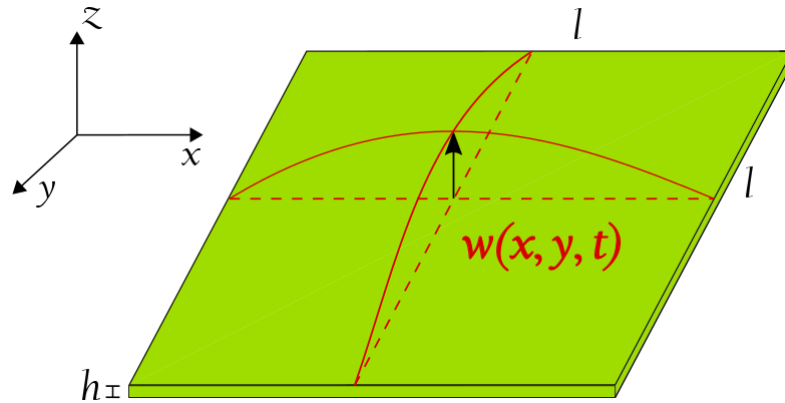


Figure 3.8: Illustration of the out-of-plane motion of a square membrane of side length  $l$  and thickness  $h$ . Its modes are described by the function  $w(x, y, t)$ .

### 3.2.2 Mechanical properties

All our mechanical resonators are fabricated out of thin layers of stressed silicon nitride  $\text{Si}_3\text{N}_4$  deposited on a silicon chip. While in the plane parallel to the chip surface the membranes have mm-sized dimensions (see Figs. 3.9), their thickness in the direction perpendicular to the surface is of few tens of nanometers. Such a low thickness yields an effective mass in the order of  $10^{-12}$  kg,

that for each sample was estimated using a finite element simulation in COMSOL Multiphysics. The small effective mass tends to have a beneficial effect, as the single-photon optomechanical coupling  $g_0$  presents an inverse square root dependency on it through the zero-point fluctuation amplitude  $g_0 \propto x_{zpf} = \sqrt{\frac{\hbar}{2m_{eff}\Omega_M}}$ . Since the feedback cooling performance improves with increasing optomechanical coupling, our resonators were designed in order to minimize the effective mass and maximize  $g_0$ .

Each microstructure presented in this work features many mechanical resonances at different frequencies. Yet for every sample we will be focusing only on a single mechanical mode at a well-defined frequency, ranging between 100 kHz and 1.4 MHz depending on the type of resonator. More specifically, we will draw our attention to the mode for which the quality factor, i.e. the ratio  $Q_M = \Omega_M/\Gamma_M$  with  $\Gamma_M$  being the mechanical damping rate, has been optimized through design and fabrication. As a matter of fact, in order to observe quantum mechanical behaviour, the requirement for quantum coherent oscillation of the mechanical resonator must be satisfied. This means that on average less than half a phonon can leak into the oscillator from the environment over a mechanical period [23]. Such criterion is determined by the inequality

$$Q_M\Omega_M > 2\frac{k_B T}{\hbar} \quad (3.16)$$

with  $T$  being the temperature. Our mechanical resonators are then engineered to maximize the  $Q_M\Omega_M$  product.

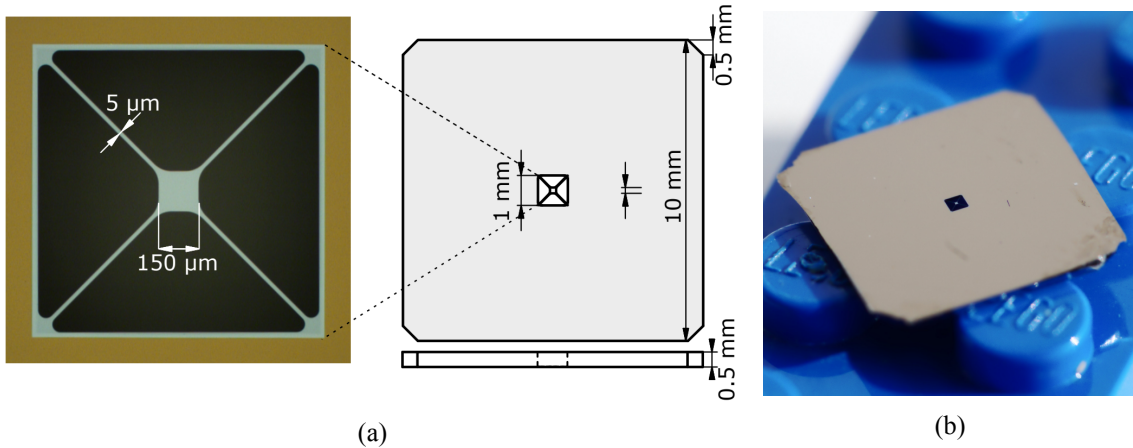


Figure 3.9: a) The dimensions of a typical trampoline chip are displayed. b) To give readers a better feeling, its size is compared to a small Lego brick.

Taking a closer look at the quality factor, we see that it quantifies the ratio between the energy stored and lost during an oscillation period. Several channels contribute to the energy losses in the resonator, so that the overall quality factor is given by the relation

$$\frac{1}{Q_M} = \sum \frac{1}{Q_{M,i}} \quad (3.17)$$

with  $Q_{M,i}$  being the different contributions. The main loss mechanisms are listed below [17].

- *Gas damping* is due to the gas molecules in the surrounding environment, which provide a viscous damping force when their pressure is high enough. This effect can be minimized simply by placing the mechanical resonator in a high-vacuum chamber and bringing the

system down to a pressure of  $10^{-6}$  mbar or lower. Fig. 3.10 shows how reducing the pressure improves the quality factor of trampoline resonators up to a saturation value.

- *Acoustic radiation* or *phonon tunneling* is caused by the dissipation of mechanical waves into the silicon substrate and sample holder. In particular, clamping the resonator chip to its holder appears to enhance this mechanism by creating more contact points, hence more channels for phonons to couple to the environment. On the other hand the impact of this phenomenon can be minimized by an appropriate design of the mechanical resonator. For example providing the membrane with a phononic shield, a periodic microstructure that creates a bandgap in the phonon dispersion. The phononic membranes presented in this work (see Fig. 3.7b) were designed following this approach [24].
- *Intrinsic damping* is related to the material properties and internal friction forces, which dominate over the other loss mechanisms when the resonator is perfectly decoupled from the environment. Use of high-stressed deposition layers has been shown to greatly reduce this mechanism and improve the quality factor [25].

The reader will have probably noticed that no information was provided about how to measure the quality factor of our mechanical resonators. A thorough description of the *ringdown* technique used for this purpose will be provided in Sec. 3.4, after we present our optical setups and their working principles.

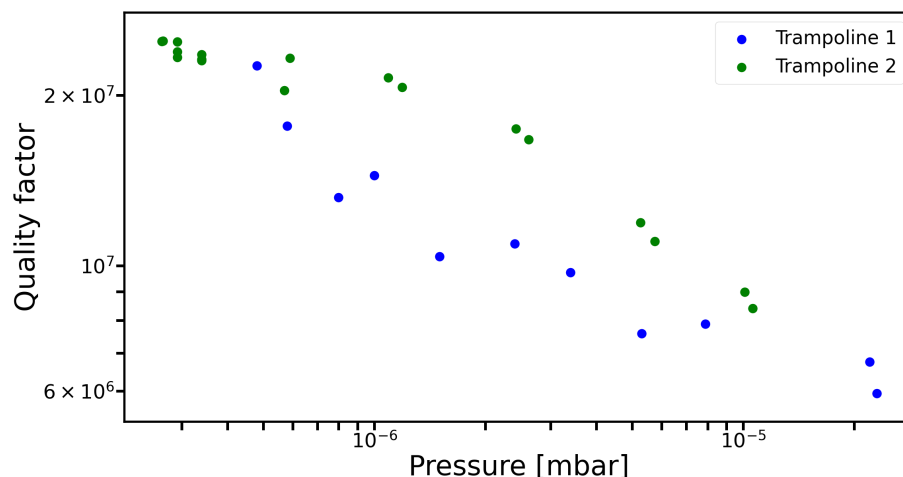


Figure 3.10: The mechanical quality factor measured as a function of gas pressure inside the vacuum chamber for two different trampoline resonators. We can observe how increasing the pressure enhances the gas damping, thus reducing the mechanical quality factor. In sample 2 (green dots) we observe a saturation of the quality factor around  $2.5 \times 10^7$  for pressure below  $7 \times 10^{-7}$  mbar, indicating that the damping rate is dominated by other loss mechanisms than air damping. Please note these values were measured before dicing the silicon carrier wafer into millimeter-sized chips. Dicing was observed to have a detrimental effect on the quality factor.

### 3.3 Optical resonators

Optical resonators or *cavities* are extraordinary objects. They can reduce the continuum of modes of a wave traveling in free space to a discrete set. They can amplify the intensity of the incoming electromagnetic fields by orders of magnitude. After introducing their basic physical principles [26, 27], we will describe how our optical cavities were designed, characterized and stabilized in frequency. Please note that, as our optical cavities are operated in vacuum, the refractive index always equals 1, hence we will make our life easier and ignore dependencies on this variable in

the following equations.

### 3.3.1 Resonance condition

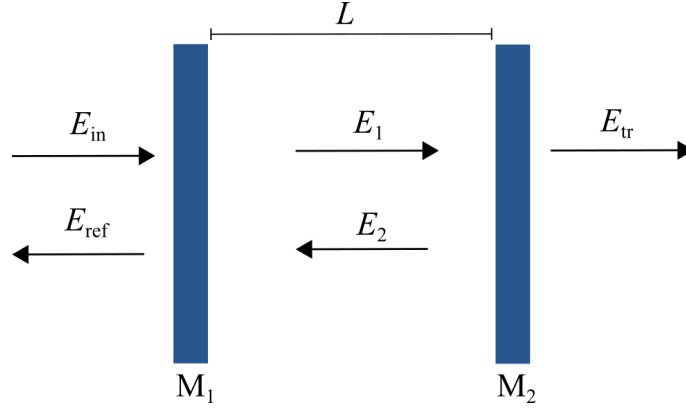


Figure 3.11: Schematic of a Fabry–Pérot optical cavity of length  $L$  featuring two plane mirrors  $M_1$  and  $M_2$ .

An optical cavity is a region of space delimited by mirrors which impose boundary conditions on an electromagnetic field. In particular, a proper arrangement of the mirrors will force the field to vanish at their location and—for specific frequencies—to form a standing wave between their surfaces. The standard cavity in optomechanics is a Fabry–Pérot resonator, a system of two parallel highly-reflective mirrors facing each other. The model we describe in the following will be based on this particular geometry, as it was chosen for our experiments too.

Let us now consider the cavity represented by two mirrors  $M_1$  and  $M_2$  with reflection and transmission coefficients  $r_i$  and  $t_i$  ( $i = 1, 2$ ), located at distance  $L$  from each other. A light beam of amplitude  $E_{in}$  impinges on  $M_1$ . This situation is depicted in Fig. 3.11. The stationary fields will have to meet the boundary conditions set by the mirrors:

$$E_1 = t_1 E_{in} + r_1 E_2 e^{ik_\lambda L} \quad (3.18a)$$

$$E_2 = r_2 E_1 e^{ik_\lambda L} \quad (3.18b)$$

$$E_{ref} = r_1 E_{in} + t_1 E_2 e^{ik_\lambda L} \quad (3.18c)$$

$$E_{tr} = t_2 E_1 e^{ik_\lambda L} \quad (3.18d)$$

where  $k_\lambda \equiv \frac{2\pi}{\lambda}$  is the light wavenumber. The intracavity field has been modeled as sum of two components traveling in opposite directions and amplitudes  $E_1$  and  $E_2$ , while the amplitude of the field transmitted (reflected) through the cavity is  $E_{tr}$  ( $E_{ref}$ ). The solutions to this set of equations are given by

$$E_{ref} = \frac{r_1 - r_2 (r_1^2 - t_1^2) e^{2ik_\lambda L}}{1 - r_1 r_2 e^{2ik_\lambda L}} E_{in} \quad (3.19a)$$

$$E_{tr} = \frac{t_1 t_2 e^{ik_\lambda L}}{1 - r_1 r_2 e^{2ik_\lambda L}} E_{in} \quad (3.19b)$$

$$E_{cav} = E_1 + E_2 = \frac{t_1 (1 + r_2 e^{ik_\lambda L})}{1 - r_1 r_2 e^{2ik_\lambda L}} E_{in} \quad (3.19c)$$

with  $E_{cav}$  being the amplitude of the total intracavity field. For a symmetric cavity,  $r_1 = r_2 = r$ ,  $t_1 = t_2 = t$  and the reflectivity and transmissivity are respectively defined as  $\mathcal{R} = |r|^2$  and  $\mathcal{T} = |t|^2$ , thus yielding:

$$r^2 - t^2 = \mathcal{R}e^{2i\phi_r} - \mathcal{T}e^{2i\phi_t} = 2e^{i\phi_r} \quad (3.20)$$

where we assumed the cavity to be lossless, hence  $\mathcal{R} + \mathcal{T} = 1$ , and  $\phi_t = \frac{\pi}{2} + \phi_r$ . The normalized transmitted intensity will then be given by

$$\mathcal{I}_{tr} = \left| \frac{E_{tr}}{E_{in}} \right|^2 = \frac{(1 - \mathcal{R})^2}{(1 - \mathcal{R})^2 + 4\mathcal{R} \sin^2 \delta} \quad (3.21)$$

where  $\delta = k_\lambda L + \phi_r$ . It is easy to see from Eq. 3.21 that the transmitted intensity is maximized when  $\delta = \delta_p = p\pi$  with  $p \in \mathbb{N}$ . The minimum distance in phase between two maxima will then be  $\delta_{p+1} - \delta_p = \pi$ . In terms of frequency  $f$ , this translates as:

$$f_{FSR} = f_{p+1} - f_p = \frac{c}{2L} \quad (3.22)$$

The quantity  $f_{FSR}$  is usually referred to as *free spectral range*. Not only it quantifies the frequency spacing between consecutive peaks of the transmitted intensity, but it gives us an estimate of the round-trip time of a photon inside the cavity  $\tau_{rt} = 1/f_{FSR}$ . More importantly, Eq. 3.22 enables us to deduce a *resonance* condition for the incoming light of frequency  $f_L$  to propagate as a stationary field inside the cavity:

$$f_L = f_p = p \frac{c}{2L} \quad (3.23)$$

Taking a closer look at Eq. 3.21, we notice that carrying out a Taylor expansion of the sine term around a maximum of transmission we can obtain

$$\mathcal{I}_{tr} = \frac{\left( \frac{1-\mathcal{R}}{\sqrt{\mathcal{R}}} \right)^2}{4(\delta - p\pi)^2 + \left( \frac{1-\mathcal{R}}{\sqrt{\mathcal{R}}} \right)^2} \quad (3.24)$$

We can clearly see that when the incoming light is resonant with the cavity, the transmitted intensity displays a Lorentzian shape with FWHM  $\delta_{FWHM} = \frac{1-\mathcal{R}}{\sqrt{\mathcal{R}}}$ . Eq. 3.24 can be expressed in terms of frequency as well:

$$\mathcal{I}_{tr}(f) = \frac{f_{FSR}^2 \left( \frac{1-\mathcal{R}}{\pi\sqrt{\mathcal{R}}} \right)^2}{4(f - pf_{FSR})^2 + f_{FSR}^2 \left( \frac{1-\mathcal{R}}{\pi\sqrt{\mathcal{R}}} \right)^2} \quad (3.25)$$

As expected, the transmission spectrum displays a Lorentzian shape in frequency and a FWHM  $k = f_{FSR} \frac{1-\mathcal{R}}{\pi\sqrt{\mathcal{R}}}$ . It will be useful to introduce one more physical quantity, called *optical finesse*, which quantifies the number of round trips a photon can undergo inside the cavity before being expelled

$$\mathcal{F} = \frac{\delta_{p+1} - \delta_p}{\delta_{FWHM}} = \frac{f_{FSR}}{k} = \frac{\pi\sqrt{\mathcal{R}}}{1 - \mathcal{R}} \quad (3.26)$$

Armed with such knowledge, we can now shine a new light on the meaning of Eqs. 3.19. When light is resonant with the cavity  $\delta = p\pi$  and we get

$$\mathcal{I}_{tr} = \frac{\mathcal{T}^2}{(1 - \mathcal{R})^2} \approx 1 \quad (3.27a)$$

$$\mathcal{I}_{ref} = \left| \frac{E_{ref}}{E_{in}} \right|^2 = \mathcal{R} \left( \frac{1 - \mathcal{R} - \mathcal{T}}{1 - \mathcal{R}} \right)^2 \approx 0 \quad (3.27b)$$

$$\mathcal{I}_{cav} = \left| \frac{E_{cav}}{E_{in}} \right|^2 = \frac{\mathcal{T} (1 + \sqrt{\mathcal{R}})^2}{(1 - \mathcal{R})^2} \approx \frac{1 + 2\sqrt{\mathcal{R}} + \mathcal{R}}{1 - \mathcal{R}} \approx \mathcal{F} \quad (3.27c)$$

Where  $\mathcal{R} \approx 1$  and  $\mathcal{R} + \mathcal{T} = 1$  have been used. These results present a clear interpretation: even in case of high-reflective mirrors, if the incident light is resonant with the cavity most of its amplitude will penetrate inside and here it will build up coherently. The finesse  $\mathcal{F}$  quantifies the amplification of the stationary field inside the cavity with respect to the impinging field. The cavity is essentially transparent to resonant light, meaning that intensity of the light transmitted through the output mirror is approximately the same as the incoming field.

Please note that results above still hold in the case of a cavity with mirrors having different reflection coefficients,  $r_1 \neq r_2$ . In such cases we simply need to change the definition of reflectivity to  $\mathcal{R} = \sqrt{\mathcal{R}_1 \mathcal{R}_2}$ . The optical finesse will then be

$$\mathcal{F} = \frac{\pi \sqrt{\mathcal{R}_1 \mathcal{R}_2}}{1 - \sqrt{\mathcal{R}_1 \mathcal{R}_2}} \quad (3.28)$$

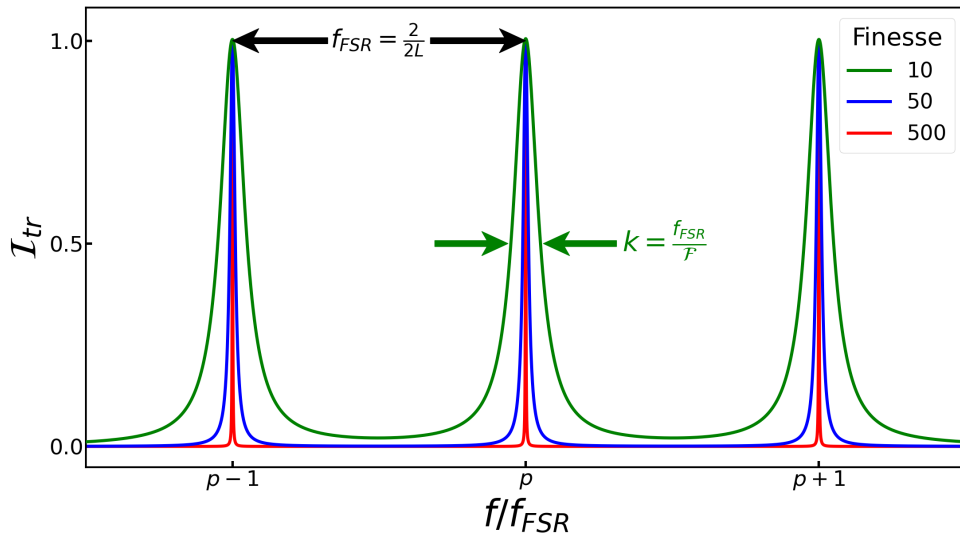


Figure 3.12: Optical resonances in a cavity are equally spaced by a frequency distance  $f_{FSR}$  and their FWHM  $k$  is defined by the finesse  $\mathcal{F}$ .

### 3.3.1.1 Cavity coupling regimes

The linewidth  $k$  quantifies the photon loss rate of a cavity and it is given by the sum of a term  $k_{ex}$  representing incoupling and outcoupling of light from free space and the internal losses  $k_0$

$$k = k_{ex} + k_0 \quad (3.29)$$

This breakdown gives rise to three different regimes of light coupling into the cavity from free space:

- *undercoupled* regime ( $k_0 \gg k_{ex}$ ), usually undesirable as it brings about loss of information,
- *critically coupled* or *impedance-matching* regime ( $k_{ex} \approx k_0$ ) where all the input light is transmitted through the cavity,
- *overcoupled* regime ( $k_{ex} \gg k_0$ ), where most input photons emerge from the cavity without being absorbed or transmitted through a secondary port.

As it will be shown, all our experiments are operated in the overcoupled regime.

### 3.3.2 Gaussian modes

Before moving forward with our description of the behaviour of optical cavities, a few details will be needed on the propagation of light. In particular, in the plane perpendicular to the direction of propagation we model the intensity profile of our beam as a Gaussian curve tending to zero as the distance from the propagation axis increases. The validity of such assumption is supported by our laser beams being well collimated and can be verified simply by shining the laser output onto a CCD camera, as we show in Fig. 3.13.

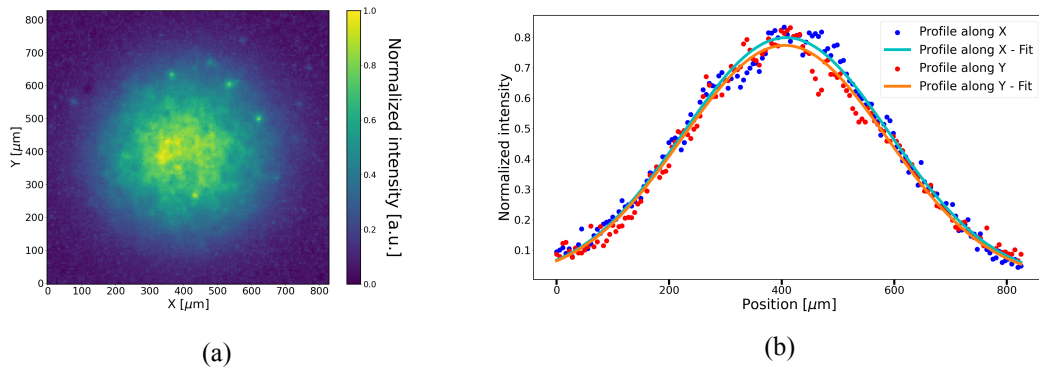


Figure 3.13: a) CCD image of one of our laser beams as outcoupled from fiber into free space. b) Cross sections of this image were successfully fitted to Gaussian curves.

We will now consider a light beam propagating in free space and featuring a well-defined wavelength  $\lambda$ , wavenumber  $k_\lambda$  and polarization. While  $z$  represents the position along its propagation axis, we can indicate the distance of a point within the beam cross section from the propagation axis itself by  $r^2 = x^2 + y^2$ , where  $x$  and  $y$  represent its cartesian coordinates. The field mode can be described by

$$u_{00}^{opt}(r, z) = u_{00} \frac{w_0}{w(z)} \exp \left\{ i [k_\lambda z - \psi(z)] - r^2 \left[ \frac{1}{w^2(z)} - \frac{ik_\lambda}{2R(z)} \right] \right\} \quad (3.30)$$

where  $u_{00}$  is a normalization constant,  $w(z)$  describes the beam radius at which the field amplitude falls by  $1/e$  with respect to its maximum value,  $R(z)$  is the radius of curvature of the beam

wavefront and the  $\psi(z)$  is the Gouy phase shift, related to the phase velocity of light. These terms feature an analytical dependency on  $z$

$$w(z) = w_0 \sqrt{1 + \left(\frac{z}{z_R}\right)^2} \quad (3.31a)$$

$$R(z) = z \left[ 1 + \left(\frac{z_R}{z}\right)^2 \right] \quad (3.31b)$$

$$\psi(z) = \arctan\left(\frac{z}{z_R}\right) \quad (3.31c)$$

Taking the point at which  $w(z)$  hits its minimum values as the origin of our spatial reference system  $z = 0$ , then we define *beam waist* and *Rayleigh range* or *Rayleigh distance* the quantities  $w_0 = w(z = 0)$  and  $z_R = \frac{k_\lambda w_0^2}{2}$ , respectively. The latter object is rather interesting, as it defines the transition between different propagation regimes. In particular, while at the beam waist position  $R(z = 0) = \infty$ , on the other hand we have  $R(z \gg z_R) \approx z$ . This means that the wavefront is planar within a distance of  $z_R$  from the beam waist position and it becomes spherical outside such range. At the same time, the spot size at the Rayleigh distance is  $w(z = z_R) = w_0 \sqrt{2}$ , hence the area of the beam cross-section is doubled with respect to the beam waist position. Finally, given their analytical relation, the smaller the beam waist the smaller the Rayleigh range, hence the beam approaches its spherical-wavefront regime more quickly. We can then define a spread angle  $\theta$  as

$$\tan \theta \equiv \frac{w}{z} \Big|_{z \gg z_R} \simeq \frac{w_0}{z_R} = \frac{2}{k_\lambda w_0} \approx \theta \quad (3.32)$$

Eq. 3.32 shows how the Rayleigh range represents a measure of the distance across which our beam propagates while remaining collimated. We can verify this model describes a Gaussian intensity profile simply by calculating the squared modulus of Eq. 3.30:

$$\mathcal{I}(r, z) = \left| u_{00}^{opt}(r, z) \right|^2 = \mathcal{I}_0 e^{-\frac{2r^2}{w(z)^2}} \quad (3.33)$$

with  $\mathcal{I}_0(z) = \frac{|u_{00}|^2}{1 + \left(\frac{z}{z_2}\right)^2}$  expressing the field intensity along the propagation axis. The Gaussian beam behaviour is sketched in Fig. 3.14.

### 3.3.3 Cavity stability and eigenmodes

We just described the behaviour of Gaussian beam of light propagating in free space. What happens when a such beam encounters mirrors on its path, provided that their spatial arrangement and reflectivities are suitable to form an optical cavity at the same wavelength? We will derive the behaviour of light inside a resonator, considering a general scenario where an optical cavity is formed by two spherical mirrors and taking into account the boundary conditions they fix.

First off, we require the optical resonator to be stable. A necessary condition is that the beam propagating inside the cavity must exactly retrace itself onto the path between the end mirrors upon reflection from one of them. For this to happen, the radius of curvature of its wavefront must match the radius of curvature of the mirrors at their respective positions. We indicate the propagation axis as  $z$ , such that  $z = 0$  is the position of the beam waist between the two mirrors positioned at  $z_1$  and  $z_2$  with radius of curvature  $R_1$  and  $R_2$ , respectively. We follow the convention

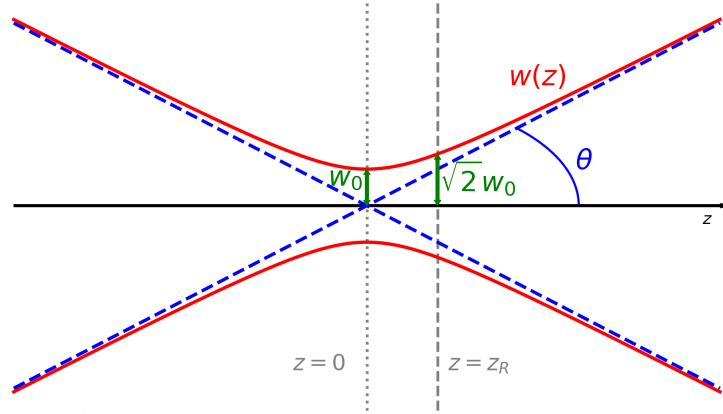


Figure 3.14: A sketch of a Gaussian beam's behaviour along the propagation axis  $z$ : at  $z = 0$  the spot size hits its minimum value  $w_0$  (*beam waist*) and it grows when moving away from this position, following the  $w(z)$  function and hitting an amplitude of  $\sqrt{2}w_0$  at the Rayleigh distance. The spreading angle  $\theta$  is indicated by dashed lines.

in which the radius of curvature is considered positive when the beam is diverging as it propagates to the right. From Eq. 3.31b, a standing wave will form only if

$$R(z_1) = z_1 + \frac{z_R^2}{z_1} = -R_1 \quad (3.34a)$$

$$R(z_2) = z_2 + \frac{z_R^2}{z_2} = R_2 \quad (3.34b)$$

Given a distance between mirrors of  $L = z_2 - z_1$ , for each mirror we can define the parameter  $g_i \equiv 1 - \frac{L}{R_i}$  with  $i = 1, 2$ . Therefore we have

$$z_1 = -L \frac{g_2(1 - g_1)}{g_1 + g_2 - 2g_1g_2} \quad (3.35a)$$

$$z_2 = L \frac{g_1(1 - g_2)}{g_1 + g_2 - 2g_1g_2} \quad (3.35b)$$

As a consequence the Rayleigh range, beam waist and spot sizes at the two mirrors will respectively be given by

$$z_R = L \frac{\sqrt{g_1g_2(1 - g_1g_2)}}{g_1 + g_2 - 2g_1g_2} \quad (3.36)$$

$$w_0^2 = \frac{2L}{k_\lambda} \frac{\sqrt{g_1g_2(1 - g_1g_2)}}{g_1 + g_2 - 2g_1g_2} \quad (3.37)$$

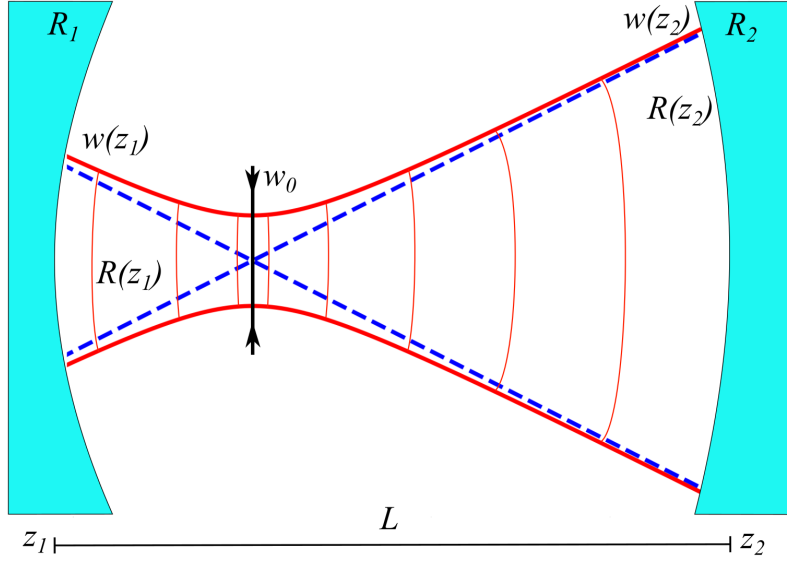


Figure 3.15: Propagation of a Gaussian beam inside a cavity formed by two spherical mirrors. For the beam resonator to be stable, the beam must trace itself back onto the optical path between mirrors upon reflection from one of them. As a consequence, the wavefront radius of curvature at each mirror position must match the mirror radius.

$$w(z_1)^2 = \frac{2L}{k_\lambda} \sqrt{\frac{g_2}{g_1(1-g_1g_2)}} \quad (3.38a)$$

$$w(z_2)^2 = \frac{2L}{k_\lambda} \sqrt{\frac{g_1}{g_2(1-g_1g_2)}} \quad (3.38b)$$

From Eqs.3.36-3.38 it is apparent that a standing wave is formed inside the resonator only when the system satisfies the *stability condition* given by

$$0 \leq g_1g_2 \leq 1 \quad (3.39)$$

It is easy to show how this model can be applied to the case of two planar mirrors described in Sec.3.3.1, simply by considering their radius of curvature to be infinite. On the other hand, such arrangement does not produce a stable optical resonator [28], hence for our experiments we chose a hemispherical configuration featuring a plane mirror and a spherical one. In this geometry,  $R_1 = \infty$ ,  $R_2 = R$  and  $g_1 = 1$ , so that  $0 < g_2 < 1$ . As a consequence the cavity length must be smaller than the radius of curvature of the spherical mirror. The beam waist is then located on the plane mirror and its size is

$$w_0^2 = \frac{2L}{k_\lambda} \sqrt{\frac{g_2}{1-g_2}} = \frac{2}{k_\lambda} \sqrt{L(R-L)} \quad (3.40)$$

while the beam radius at the position of the spherical mirror is

$$w(z_2)^2 = \frac{2L}{k_\lambda} \sqrt{\frac{1}{g_2(1-g_2)}} = \frac{2R}{k_\lambda} \sqrt{\frac{L}{R-L}} \quad (3.41)$$

Now that we found ourselves a stability criterion for optical resonators, we can have a discussion on the eigenmodes of the intracavity field. In general, after one round trip, this can be described as a propagation integral of the initial field

$$\mathcal{E}^{(1)}(x, y) = e^{-2ik_\lambda L} \iint K(x, y, x_0, y_0) \mathcal{E}^{(0)}(x_0, y_0) dx_0 dy_0 \quad (3.42)$$

where the integral is evaluated over an arbitrary reference plane perpendicular to the cavity axis while  $K$  represents the propagation kernel. Solutions to this linear operator equation are given by a set of eigenmodes  $\mathcal{E}_{mn}(x, y)$  determined by eigenvalues  $\gamma_{mn}$  satisfying the propagation relation

$$\mathcal{E}_{mn}^{(1)}(x, y) = e^{-2ik_\lambda L} \gamma_{mn} \mathcal{E}_{mn}^{(0)}(x, y) \quad (3.43)$$

Please note that this means the eigensolutions correspond to optical modes that trace themselves exactly back onto the path between the cavity mirrors upon reflection from one of them. This was the condition we set when looking for a stability criterion for the resonator. Although in general our eigenvalue problem does not necessarily have a solution, we can prove that the Hermite-Gauss functions satisfy said conditions. These are usually referred to as  $\text{TEM}_{mn}$  and are given by

$$u_{mn}^{opt}(x, y, z) = u_{mn} \frac{w_0}{w(z)} H_m \left( \frac{\sqrt{2}x}{w(z)} \right) H_n \left( \frac{\sqrt{2}y}{w(z)} \right) \times \exp \left\{ i [k_\lambda z - \psi_{mn}(z)] - (x^2 + y^2) \left[ \frac{1}{w^2(z)} - \frac{ik_\lambda}{2R(z)} \right] \right\} \quad (3.44)$$

where  $m, n \in \mathbb{N}$ ,  $H_j$  represents the  $j$ -th Hermite polynomial while  $\psi_{mn}(z)$  is once again the Guoy phase, now expressed by

$$\psi_{mn}(z) = (m + n + 1) \arctan \frac{z}{z_R} \quad (3.45)$$

The perceptive reader will quickly notice that for  $m = n = 0$ , Eq.3.3.3 takes the form of the field  $u_{00}^{opt}(r, z)$  in Eq. 3.30, i.e. the fundamental mode of the intracavity field has Gaussian shape. Furthermore, the Hermite Gauss functions form a complete basis, meaning that any resonant field can be written as a linear combination of the cavity modes they describe

$$\mathcal{E}(x, y) = \sum_{mn} c_{mn} \mathcal{E}_{mn}(x, y) \quad (3.46)$$

Knowledge of the modes of an optical cavity allows us to reformulate its resonance condition. For a standing wave to form inside the resonator, the phase change light undergoes after one round trip needs to be an integer multiple of  $2\pi$ . This means that at  $x = y = 0$  we must get

$$k_{\lambda, pmn} L - [\psi_{mn}(z_2) - \psi_{mn}(z_1)] = p\pi \quad (3.47)$$

with  $p \in \mathbb{N}$ . This formula can easily be translated into terms of frequency

$$f_{pmn} = \frac{c}{2L} \left[ p + \frac{m + n + 1}{\pi} \arccos(\sqrt{g_1 g_2}) \right] \quad (3.48)$$

where  $p$  quantifies the number of antinodes of the field along the cavity axis, hence it identifies a specific *longitudinal* mode, while  $m, n$  describe the transverse mode.

## 3.3.4 Cavity design

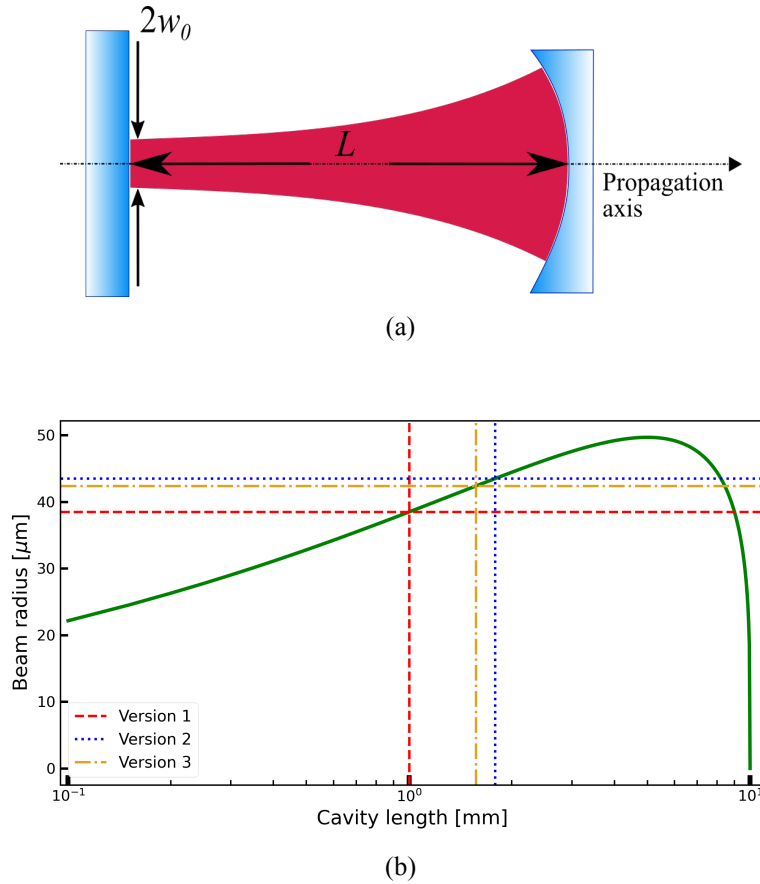


Figure 3.16: a) Propagation of  $\text{TEM}_{00}$  inside a hemispherical cavity. The waist position is located on the plane mirror, where the radius of curvature diverges. At the position of the spherical mirror, the radius of curvature of the Gaussian beam matches that of the mirror itself,  $R(L) = R$ . b) Eq. 3.40 allows us to determine the beam-waist size inside the cavity as a function of its length. The red, blue and golden lines pinpoint the length values chosen for the cavity design in the different versions of the feedback cooling experiment we performed and the corresponding accepted beam waists.

Different versions of a feedback-cooling experiment will be presented in this thesis, based on different optical cavities. Although different mirror reflectivity values were chosen for the optical resonators, they all feature a hemispherical geometry with a concave spherical mirror of radius of curvature  $R = -10$  mm. This provides an upper boundary to the cavity size since, as we saw in Sec. 3.3.3, its length needs to be shorter than  $R$  for the resonator to be stable. Furthermore, Eq. 3.40 allows us to determine how large the beam waist will be inside the cavity. How this relation plays out is displayed in Fig. 3.16b. As Fig. 3.16a shows, given the choice of a hemispherical cavity, the beam waist will be located on the flat mirror.

In general using a small cavity is beneficial, as for Fabry–Pérot resonator the optomechanical coupling is inversely proportional to the cavity length [23]. Nevertheless, a trade-off must be found, as practical considerations in the design of the optomechanical assembly must be taken into account. For example, the distance between mirrors cannot be shorter than the thickness of the silicon chip carrying the mechanical resonator, which is about 0.5 mm. One more constraint is given by the necessity for the optical mode to overlap with  $150 \mu\text{m} \times 150 \mu\text{m}$  central pad of the mechanical resonator. As our membranes are placed at submillimeter distance from the plane mirror, this con-

dition translates into having  $w_0 \leq 75 \mu\text{m}$ . For the three cavities used for feedback cooling, length values of 1 mm, 1.788 mm and 1.568 mm were chosen, respectively corresponding to waist sizes of  $38 \mu\text{m}$ ,  $43 \mu\text{m}$  and  $42 \mu\text{m}$ .

Differences between the three cavities are listed in Table 3.1, where the expected finesse values calculated from Eq. 3.28 can be found. Difference in the transmissivity  $\mathcal{T}$  of their mirrors brought about a significant change in the theoretical finesse moving from a vertical geometry to a horizontal one. The choice to decrease it was due to the availability of mirrors in our lab rather than to scientific reasons.

Cavity	Geometry	$L$ [mm]	$w_0$ [ $\mu\text{m}$ ]	$\mathcal{T}_{\text{plane mirror}}$ [ppm]	$\mathcal{T}_{\text{spherical mirror}}$ [ppm]	$\mathcal{F}_{\text{theory}}$
1	Vertical	1	38	200	10	29 917
2	Horizontal	1.788	43	400	200	10 470
3	Horizontal	1.568	42	400	10	15 322

Table 3.1: Some characteristics of the cavities used for of the feedback cooling experiments.

### 3.3.5 Mode-matching laser to cavity fundamental mode

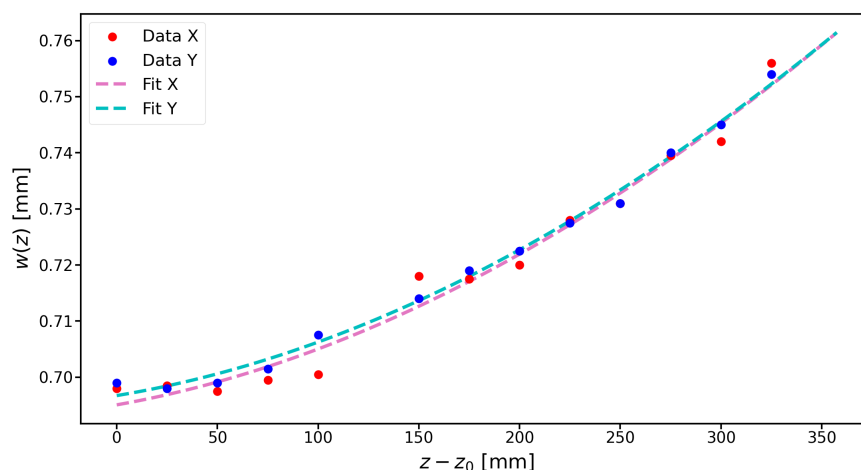


Figure 3.17: Knife-edge data and fit. Our commercial profiler measures the beam radius along orthogonal directions  $X$  and  $Y$ . Here we fit both datasets to Eq. 3.49. Unsurprisingly, the fit results are extremely similar in the two directions, with a waist size of  $692 \mu\text{m}$  and  $693 \mu\text{m}$  and waist position of  $-85 \text{ mm}$  and  $-83 \text{ mm}$  for the  $X$  and  $Y$  components, respectively. To choose our mode-matching lenses, we simply considered the average between the  $X$  and  $Y$  values.

In all our measurements, we worked with the Gaussian-shaped fundamental mode of the cavity field  $\text{TEM}_{00}$ . The quality factor of our mechanical resonators is optimized only for the fundamental mechanical mode, which typically features a Gaussian intensity profile. Thus  $\text{TEM}_{00}$  represents the cavity mode of maximum overlap with the mechanical-displacement field, yielding the strongest optomechanical interaction. Given the very specific spatial distribution of  $\text{TEM}_{00}$ , it is quite unlikely that our laser propagating in free space can match it. This is a vital aspect though, as the higher the spatial overlap (*mode-matching*) between our laser and the fundamental cavity mode, the higher is the transfer of energy between the two. The higher the mode-matching, the lower is the amount of optical power wasted exciting higher-order cavity modes. Since our laser features a Gaussian intensity profile too, once the waist size and position of  $\text{TEM}_{00}$  are determined, all it takes is a few lenses to obtain a high mode-matching efficiency. Taking our horizontal cavity

as an example, given its hemispherical configuration, its length and the radius of curvature of its spherical mirror we can easily determine a beam waist of  $43\ \mu\text{m}$  located on the incoupling plane mirror. The beam waist size and position of our laser in free space can simply be measured by a knife-edge technique. This is carried out shining the laser light on a powermeter and cutting the beam with a slit, which is then moved in the plane  $XY$  perpendicular to the light propagation axis  $\vec{z}$ . The Gaussian profile of intensity can thus be reconstructed in order to extrapolate the beam radius at the position of the slit. Repeating this measurements for different positions of the slit along  $\vec{z}$  and fitting the  $z$  vs  $w(z)$  data to

$$w(z) = w_0 \sqrt{1 + \left( \frac{z - z_0}{z_R} \right)^2} \quad (3.49)$$

where  $z_0$  is a known reference position for the measurements, allows to determine position and size of the beam waist. We used a commercial BP209-IR tool Dual Scanning Slit Beam Profiler from Thorlabs to record our knife-edge data. Fig. 3.17 shows the measurement results. Fitting yields a waist size of about  $693\ \mu\text{m}$  and position of  $-84\ \text{mm}$ , where the negative sign indicates the beam waist is located before the reference position  $z_0$ . Choosing a set of two lenses with focal lengths of  $-100\ \text{mm}$  and  $150\ \text{mm}$  at a distance of  $25\ \text{mm}$  and  $360\ \text{mm}$  from reference  $z_0$ , respectively, allows to match our laser beam to the target  $\text{TEM}_{00}$  mode of our cavity.

As stated previously in Sec. 3.1.3.1, a similar approach can be used to mode-match the local oscillator to the signal beam and increase the visibility of homodyne detection. In this case, lenses are usually placed along the path of the local oscillator in order to match its spatial profile to the signal beam. Please note that matching the local oscillator to the probe—not the other way around—prevents an increase in the number of optical components in the path of the signal beam, hence avoiding an increase of optical losses.

### 3.3.6 Optomechanical assembly

We will now present more details about how the two cavity assemblies were manufactured and put together. They were both designed bearing a simple criterion in mind, which is to enhance the spatial overlap between the fundamental modes of the mechanical and optical resonators. In addition, the system must be located in high vacuum ( $10^{-5}$  to  $10^{-9}$  mbar) in order to minimize the effect of gas damping on the mechanical oscillator and maximize the mechanical quality factor. The optomechanical assembly needs then to be fabricated out of materials with outgassing rate as low as possible in high vacuum. While cavity mirrors and the mechanical-resonator chip are made of vacuum-compatible materials, metals such as stainless steel, aluminium and copper were chosen for the rest of the assembly.

#### 3.3.6.1 Experimental setup I—Vertical cavity

The first version of our experimental setup was designed and built by Jan Bilek, who carried out his PhD research in our group between 2015 and 2018. Its vertical geometry reflects the need to minimize the detrimental effects of chip clamping on the mechanical quality factor [29]. It simply relies on gravity to hold the sample in position on a plane parallel to the optical table. This is achieved by orienting the cavity axis vertically, in the direction perpendicular to the plane of the optical table and to the rest of the optical setup. Drawings of the optomechanical assembly are presented in Fig. 3.18b-d. Using a  $45^\circ$ -mount mirror light is steered out of the optical-table plane into the vertical direction and coupled to the cavity through the plane mirror. This is held in position by a clamp screwed into the bottom plate of the assembly. A fluorocarbon (Viton) o-ring is fitted in between the mirror and the clamp to avoid damage to the optical component. The plane mirror supports the Si chip carrying the mechanical resonator, which is aligned to the cavity axis with a precision of  $\pm 0.1\ \text{mm}$  by positioning it inside a cut-out on the flip side of bottom plate. The kind of chips used in this version of the experiment feature a  $\sim 10\ \mu\text{m}$  spacer that prevents the membrane

from crashing against the plane mirror. The spherical mirror was held parallel to the plane one by a manual XY stage (OWIS MKT 40B-D15-SH-V6) used for fine-tuning of the cavity-axis position with respect to the central pad of the mechanical resonator. A piezo actuator was placed between the XY stage and the concave mirror to control its position and lock the cavity resonance frequency to the probing laser (more details about this will follow in the section about frequency-locking). The whole structure is located inside a custom-made metal scaffold holding the cavity in position and hanging from the top flange of the vacuum chamber. Except for the mirrors, all the components inside the chamber feature an aperture perpendicular to the direction of the cavity axis in order to provide optical access from both sides.

Laser light can be steered through the center of the optomechanical cavity with a simple method. A CCD camera is held vertically about 15 cm above the vacuum chamber's top flange, which contains an IR-coated glass window. Before aligning the laser to our cavity, the mechanical resonator inside the cavity is imaged exploiting the high transmissivity of the mirrors for visible light. The spherical mirror is thus shifted to a position over the membrane's central pad using the XY stage. An IR detector is then placed between the chamber window and the camera and laser light is aligned to the cavity. After removing the detector, an IR sensor card can be held right below the incoupling mirror in such a way that the secondary, visible-range emitted light can be imaged by the camera as shown in Fig. 3.19. If such light does not go through the membrane central pad, the position of the spherical mirror can be corrected using the XY stage. Please note that every adjustment of the mirror position corresponds to a displacement of the optical resonator's axis, hence laser light must be realigned to the cavity using the IR detector. After some iteration, the light should cross the center of both the mechanical resonator and the cavity and the chamber can be pumped down into high vacuum. Although this represents the best approach we could find, the resulting alignment between membrane and cavity is not precise enough. A poor overlap is then obtained between the mechanical-displacement field and fundamental intracavity mode, yielding a low optomechanical coupling. We will come back to this issue later in the chapter about experimental results, where we will explain how we decided to redesign the entire cavity to fix it.

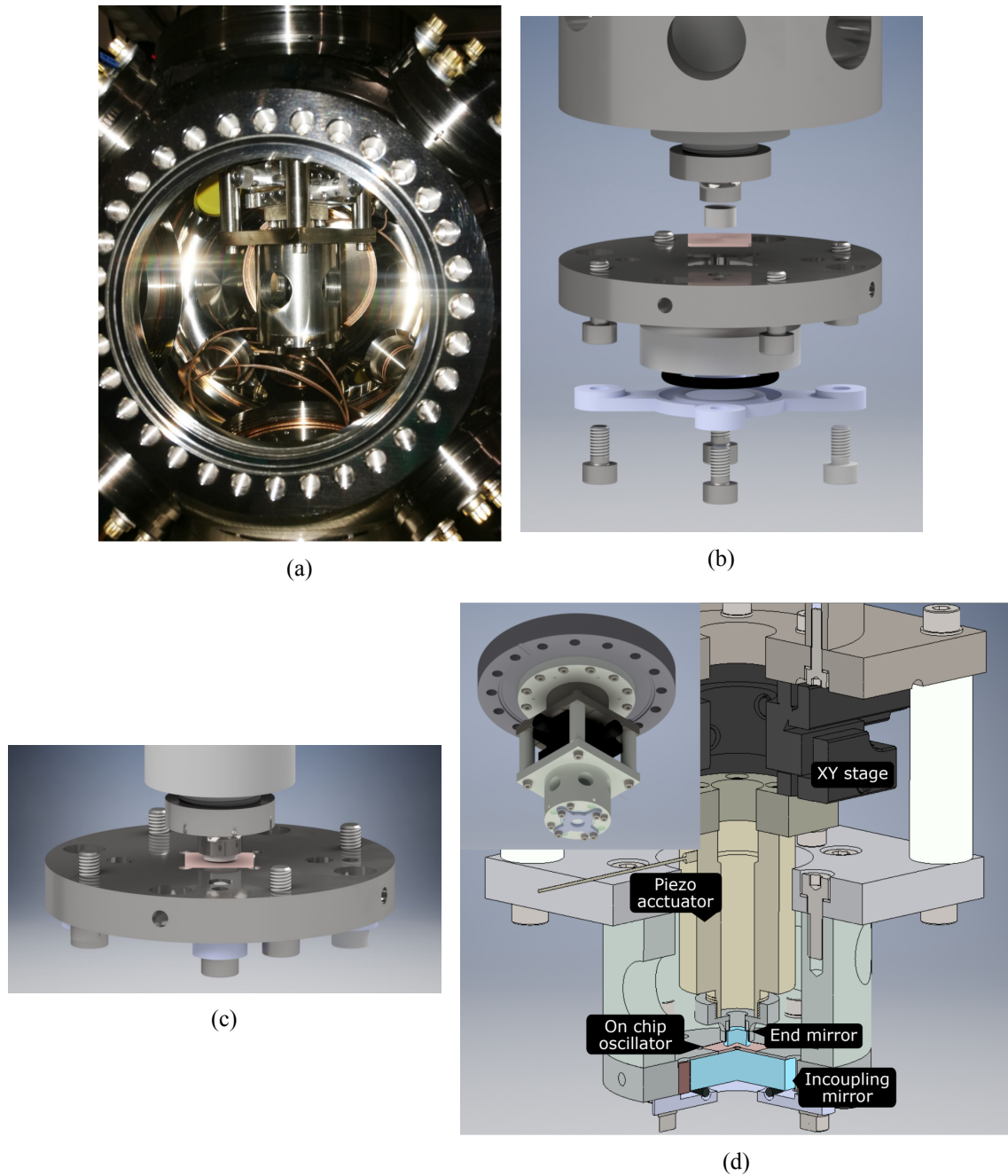


Figure 3.18: a) Picture of the vertical optomechanical assembly inside the vacuum chamber. The central column hosting the cavity hangs from the top flange of chamber. b) Design of the vertical optomechanical cavity. An exploded view of the assembly including optical cavity and on-chip mechanical oscillator (in pink) is displayed. While the concave mirror was glued to the piezo actuator, the plane one was clamped to the bottom of a ConFlat flange. A cut-out in the flange plate provides a rough alignment for the position of the chip, which is supported by the plane mirror itself. c) The steel cylinder was removed to give a better view of the 1 mm-long cavity. d) Three-quarters section view of the vertical assembly. While the XY stage, piezo actuators and mirrors were commercially available, the stainless-steel scaffold was custom made in our workshop. The piezo actuator is bound to a XY stage which is used to fine-tune the alignment of the cavity axis to the membrane central-pad. Inset shows a bottom view of the cavity assembly. Images from [16].

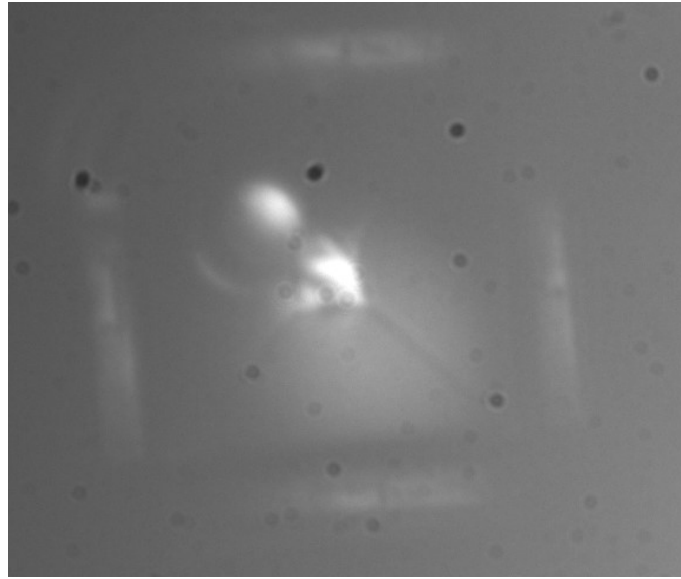


Figure 3.19: Vertical cavity: CCD image of a trampoline membrane seen through the spherical mirror. To its corner the circle of the mirror apex is visible. The light spot overlapping with the trampoline is in the visible spectrum as it is emitted by the IR sensor card used for alignment.

### 3.3.6.2 Experimental setup II —Horizontal cavity

In order to obtain a good overlap between the mechanical-displacement field and the fundamental intracavity mode and to boost the optomechanical coupling, during my PhD I designed and built two new optomechanical assemblies. These are based on the same optical geometry as the previous cavity, with a 1-inch-diameter plane mirror and a spherical one with a diameter of 5 mm and a radius of curvature of 10 mm. Nevertheless, these new cavities feature two fundamental differences with respect to the previous design. To begin with, the cavity axis is *parallel* to the optical table, which means light can be steered into the optical resonator without exiting the setup plane. This considerably shortens the distance light has to travel to reach the cavity, making mode-matching much easier. Unlike the case of the vertical cavity, using an in-plane configuration enables to actually see where the beam enters the cavity, making alignment easier. A high mode-matching efficiency can thus be obtained with much less effort. Furthermore, better control over the path of the backreflected light was achieved. Since our homodyne detection measurements are performed on the light reflected off the cavity, spherical aberration can limit our detection efficiency in the vertical-cavity setup. Small deformations of the backreflected beam due to misalignment of its path yield an upper boundary to the mode-matching with the local oscillator, ultimately limiting our homodyne visibility. This problem is easily fixed when using a horizontal configuration.

A second, more fundamental feature of our horizontal-cavity assembly is the fact that it represents a *monolithic* system. The relative positions of the cavity axis and the membrane's central pad are fixed by references embedded into the cavity mount and the chip carrying our mechanical resonator. An area of  $400 \times 400 \mu\text{m}$  was removed from each corner of the silicon chips by chemical etching during the microfabrication process. The precision of this process is limited by the photolithography step, delivering an uncertainty of about  $\pm 10 \mu\text{m}$ . Correspondingly, the shape of a  $500 \mu\text{m}$ -deep square cut-out was engraved into the assembly mount in such a way the inward, concave corners would match the etched-off features of the silicon chip (orange areas in 3.20b and d), which can thus be positioned with extreme precision (Fig. 3.21 a). On the back-side of the cut-out, a  $200 \mu\text{m}$ -thick ring was carved out with inner and outer diameters of 1.4 mm and 3.2 mm, respectively (green areas in 3.20a and c), so that the spherical mirror can be positioned around it. The assembly mount was manufactured by a CNC machining process capable of removing metal layers from the opposite sides of an object at the same time. Processing both sides of the assembly

simultaneously yields extreme precision in the relative alignment of their features, whose uncertainty is estimated to be about  $\pm 5 \mu\text{m}$ . Both the square cut-out and the reference ring located at the bottom of larger cylindrical wells, designed to accommodate the mirrors (yellow areas in 3.20a and c, blue areas in 3.20b and d). Once these have been entered, they're held in position by metal side plates (see Fig.d). As the chip features no embedded spacers and its membrane is oriented toward the incoupling plane mirror, a silicon ring is used to prevent them from coming into contact and cause damage (Fig. 3.21b). This ring has an additional function of providing tunability to the cavity length and to the relative position of the membrane inside the optical resonator. To prevent the chip from falling out of the cut-out, it was fixed to the assembly mount by two stripes of Kapton tape. Once the whole structure is closed by clamping the side plates to the main body of the assembly, no degree of freedom is allowed for the chip nor the curved mirror. Combining the uncertainties given by the chip fabrication and the CNC processing, an overall uncertainty of about  $15 \mu\text{m}$  is estimated for the relative alignment of the optical axis with respect to the center of the membrane. Given a size of  $150 \times 150 \mu\text{m}$  for the membrane central-pad, such a tolerance should yield a very good overlap between the optical and mechanical-displacement fields.

Two separate optomechanical assemblies were built using this geometry, the former containing a phononic membrane and the latter a topology-optimized trampoline. Also the optical properties of the two assemblies differ due to the different mirror transmissivity (see Table 3.1). Finally, different thickness values were chosen for the Si ring spacers, yielding different cavity length. In particular, a  $420 \mu\text{m}$ -thick ring was chosen for the first version and a  $200 \mu\text{m}$ -thick one for the second.

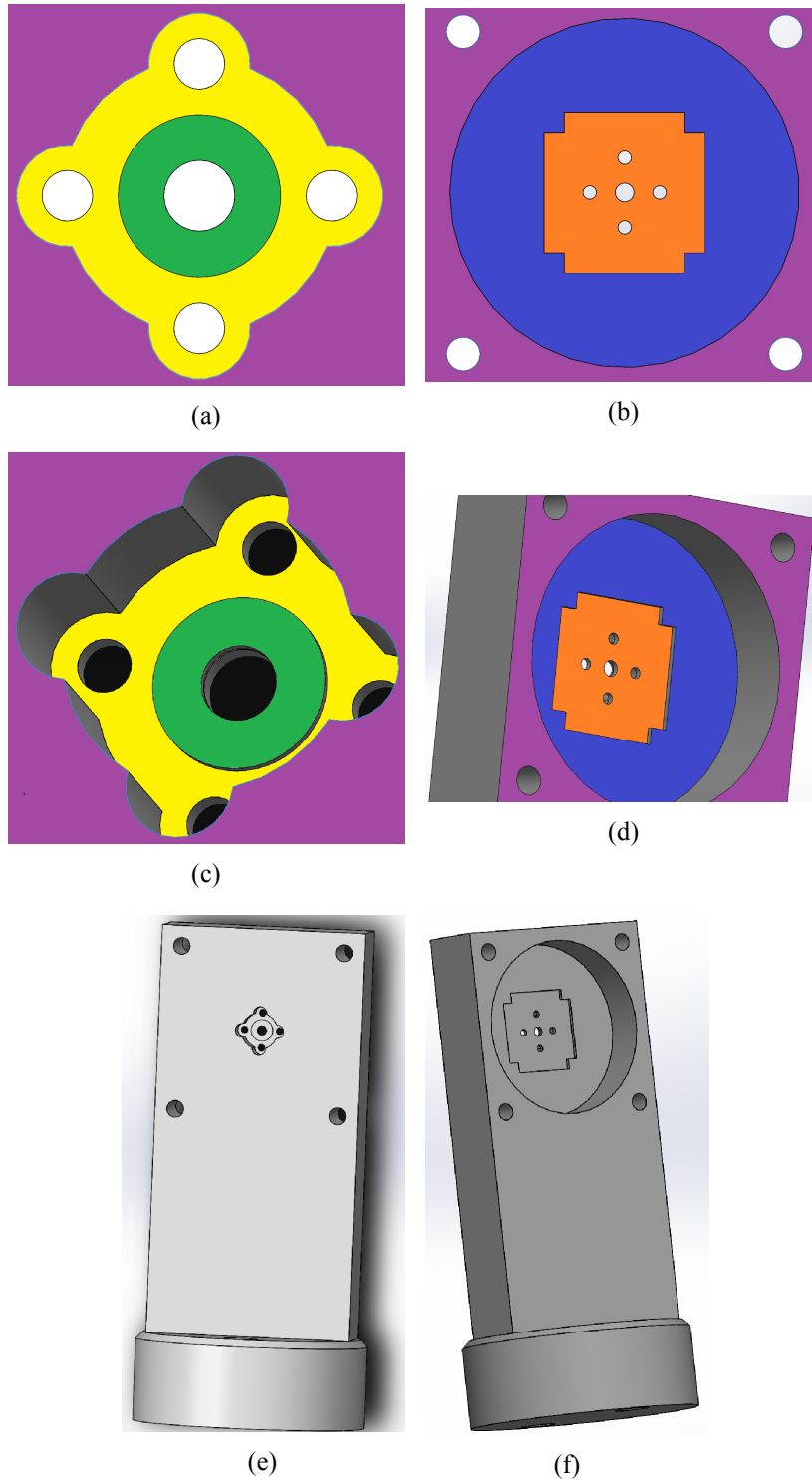


Figure 3.20: a and c) A metal ring (green) sticks out of the optomechanical assembly and it is used as an inner boundary to position the spherical mirror. A square with removed corners is cut-out (orange in Figs. b and d) from the opposite side of the assembly. Dimensions are chosen so that its inward, concave corners match the etched-off corners of the membrane chip, which can then be fit inside. Figs. e and f show the opposite sides of the optomechanical assembly design.

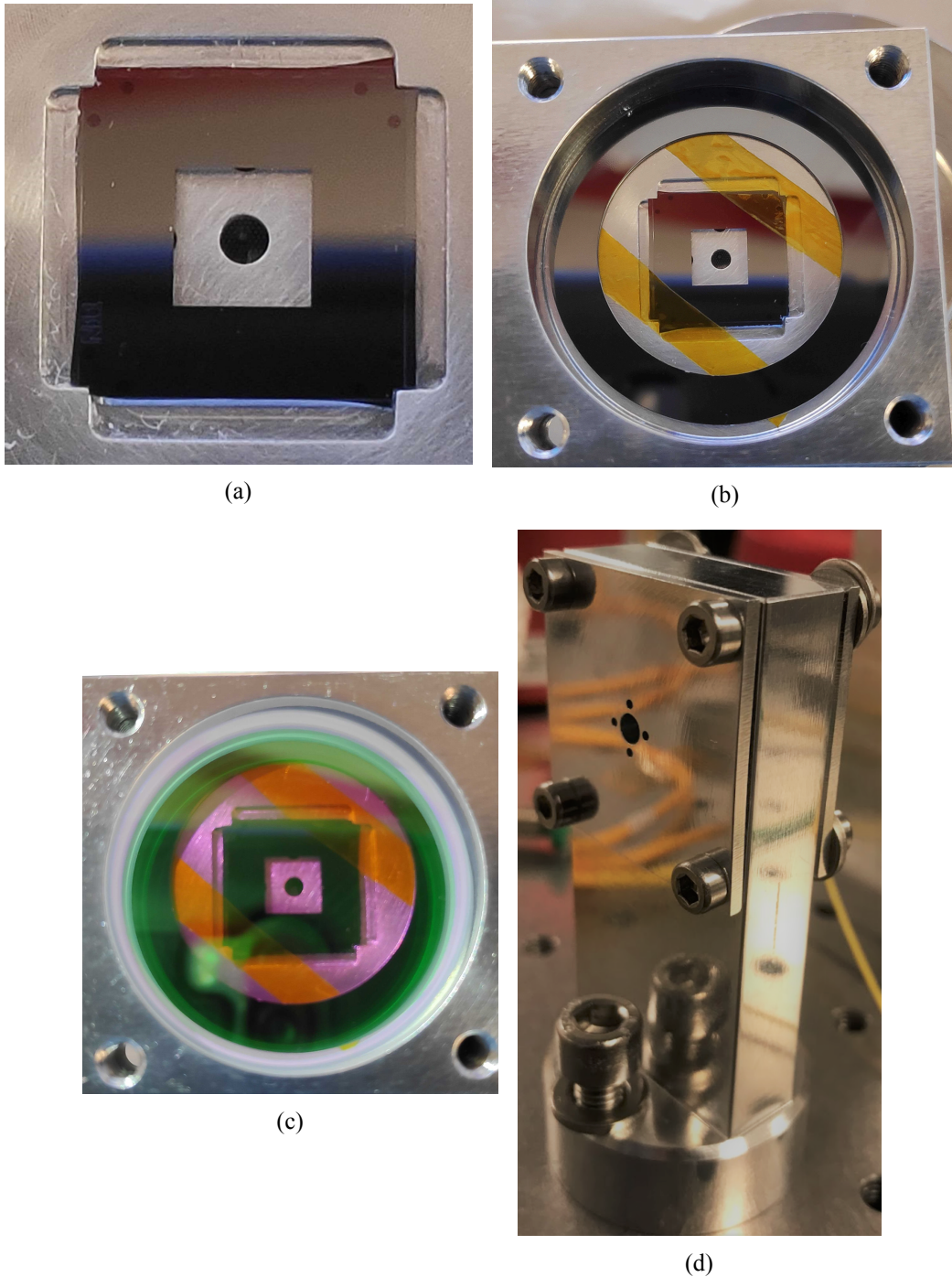


Figure 3.21: a) Mechanical-resonator chip is positioned inside a cut-out in the cavity mount. The chip corners have been etched off in order to match the inward, concave corners of the cut-out, thus ensuring the alignment between the cavity axis and the central pad of the membrane. b) The chip is fixed to the cavity mount by two Kapton tape stripes to prevent it from toppling over when the cavity axis is parallel to the optical table. As the membrane is bound to the top surface of the chip, a silicon ring spacer provides a small gap between the chip and the plane mirror to avoid contact between them. The mirrors are then placed into the assembly (Fig. c) and held in position by metal side plates (Fig. d). Both the main body of the assembly and the side plates feature circular holes aligned with the membrane window of the silicon chip and the center of the spherical mirror, in order to provide optical access to the cavity from both sides.

3.3.6.3 Aligning laser to a cavity

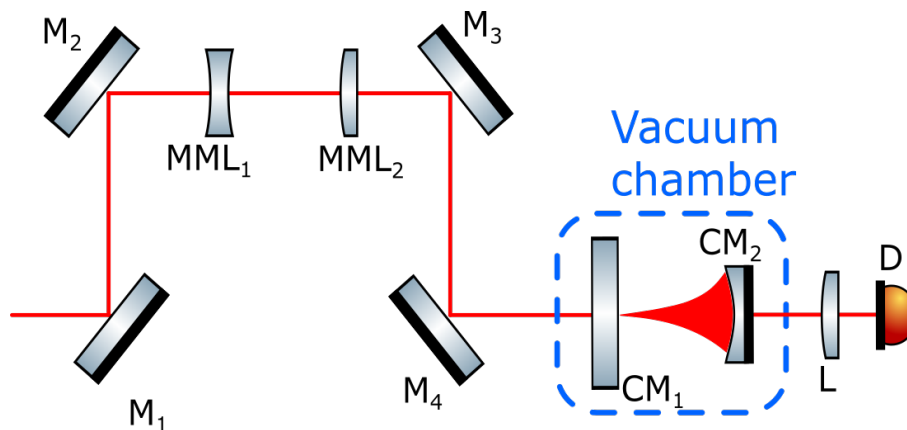


Figure 3.22: Schematic of the components necessary to interface an optical setup with a linear cavity, located inside a vacuum chamber.

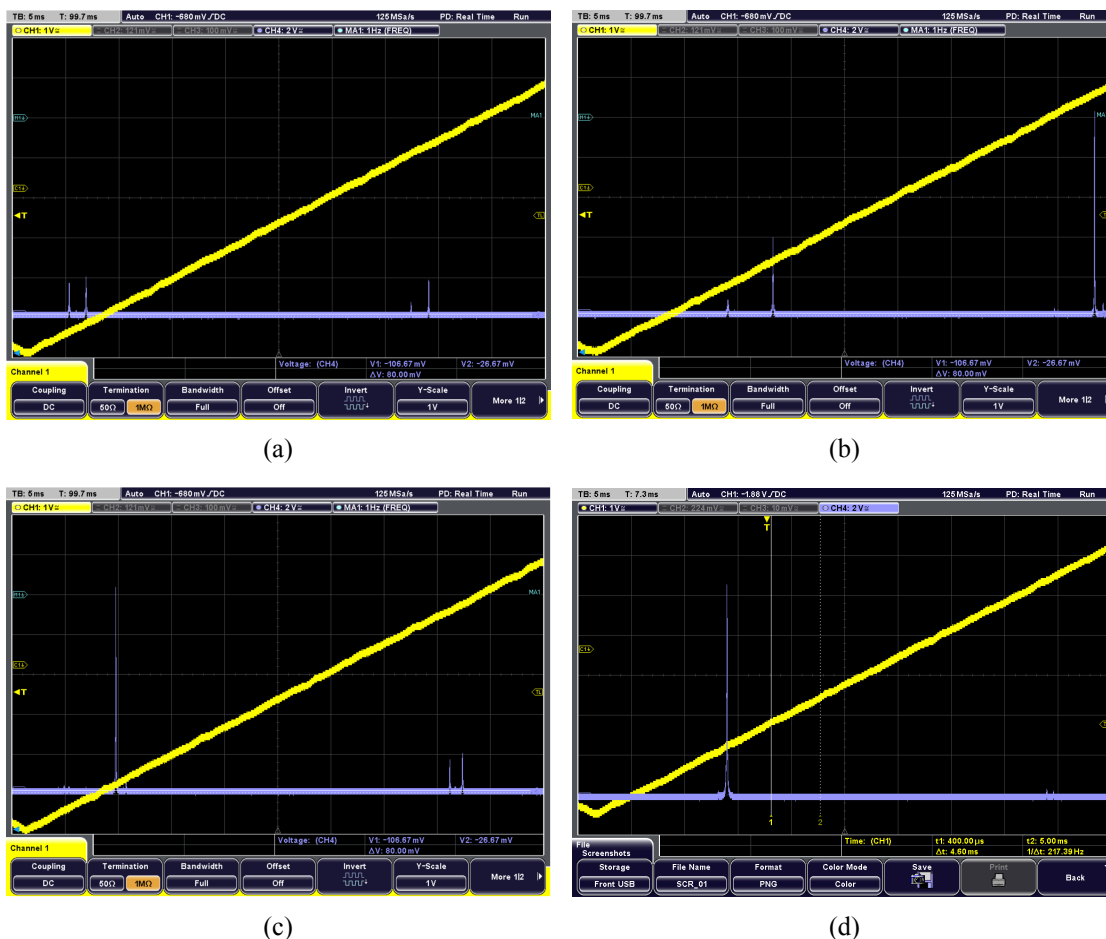


Figure 3.23: Oscilloscope screenshots presenting different stages of cavity alignment. Blue traces correspond to cavity transmission while the yellow ramp is the signal to the internal piezo of the laser. In detail, we display the transmission spectra at a) step 8, b) step 10 and c) step 12. d) shows the final result with  $TEM_{00}$  mode dominating over all the other modes. Scales are not comparable between different plots as the detector gain was frequently adjusted during the process.

We already explained in Sec. 3.3.5 how to choose lenses to mode-match our laser beam to the cavity  $TEM_{00}$  mode. Now we can proceed to explain how a combination of such lenses with mirrors can be used to couple light into the cavity with high efficiency. Our goal is to single out the specific cavity mode  $TEM_{00}$  and transfer (ideally) all input optical power to it. In order to precisely monitor which cavity modes we are exciting, the cavity frequency spectrum needs to be swept through while aligning the laser to it. This can be achieved by continuously varying either the cavity length or the frequency of the probing laser. We use the former approach to couple light to our vertical cavity, whose spherical mirror is bound to a piezo actuator, to which we send a  $\sim 10$  Hz voltage ramp signal. Our horizontal cavities being monolithic, their size cannot be changed and we resort to use a widely-tunable-frequency laser for alignment. We chose a Toptica CTL1550, whose output frequency can be scanned applying a slow ( $\sim 10$  Hz) voltage ramp signal to an internal piezo actuator. As a rule of thumb, the frequency scanning range must be larger than the FSR of the cavity for alignment to be possible. While meeting this criterion is easy in the case of a length-tunable cavity—we only need to choose a piezo of suitable stroke—it is a bit trickier when using a frequency-tunable laser. In most commercial devices, the frequency scanning range never exceeds 35 GHz, while the FSR of our cavities is above 80 GHz, as it can be worked out from the length values reported in Table 3.1. Our Toptica CTL1550 allowed us to solve this issue by varying the central wavelength around which frequency is modulated with a sensitivity of 10 pm. Stitching together several 35 GHz windows enabled us to reconstruct the frequency range equivalent to one cavity FSR. For detection of the transmitted light while aligning, we recommend the use of a photodetector with large area and adjustable gain, such as the PDA50B2 Ge switchable-gain amplified detector.

We can refer to Fig. 3.22 to explain the method we follow for cavity alignment. For educational purposes, here we present the specific example of our horizontal cavity. This method is rather general though, therefore with a few tweaks we can apply it to any linear cavity. We start with a clean optical table and an empty vacuum chamber on it. Here is what come next:

1. we arrange the mirrors outside the chamber to guide light along lines parallel to the screw-hole lattice of the table, paying particular attention to the path between mirrors  $M_2$  and  $M_3$  and inside the chamber;
2. detector D is aligned to the beam after the chamber and a lens L focuses light onto it;
3. the cavity is positioned inside the chamber;
4. mirrors  $M_3$  and  $M_4$  (*steering mirrors*) are used to walk the beam onto its plane mirror—from here on it is necessary to make sure the laser frequency is scanning;
5. when small optical modes appear in the transmitted light, we use  $M_4$  only to maximize their signal and  $M_3$  to overlap the path of the light reflected off the cavity to input light;
6. once an optimum is achieved, the vacuum chamber is sealed and the vacuum pumps are turned on;
7. while air is being removed, cavity mirrors tend to move. After the pressure sets below  $10^{-4}$  mbar repeat step 5;
8. lens  $MML_2$  is positioned, making sure not to suppress the cavity modes (see Fig. 3.23a);
9. lens  $MML_1$  is added to the setup, positioning it in such a way to enhance the cavity modes;
10. the beam is walked using  $M_4$  to maximize the modes' height and  $M_3$  to overlap back-reflected light to the input (see Fig. 3.23b);
11. when an optimum is reached, one mode should dominate over all others;

12. we adjust the position of the lenses while beam walking, trying to enhance this mode and suppress the others (see Fig. 3.23c).

If the highest mode is indeed  $TEM_{00}$ , we should be able to decrease the intensity of the other modes to  $1/50$  times the height of the main one or even make them disappear (see Fig. 3.23d). If this is not possible, we focus on a different mode and repeat the last step.

### 3.3.7 Cavity characterization

After discussing how our cavities were designed, built and aligned, it is about time to go through their characterization. In particular, we measured their escape efficiency, linewidth and FSR using the setup in Fig. 3.24. A  $\frac{\lambda}{2}$  waveplate is used in combination with a PBS immediately after the fiber coupler in order to regulate the input power to the cavity. Separate photodiodes are used to detect light transmitted and reflected from the cavity and their output signal is monitored using a Rohde & Schwarz RTM2054 oscilloscope. A polarization beam splitter followed by a  $\frac{\lambda}{4}$  waveplate is used before the cavity to make sure the reflected light is steered into a different path than the input. For the the measurement of the cavity linewidth a phase modulator is needed. We chose a MPZ-LN-10 electro-optic modulator (EOM) from iXblue Photonics. The RF signal controlling the phase modulation was provided by the internal function generator of our network analyzer E5061B from Keysight.

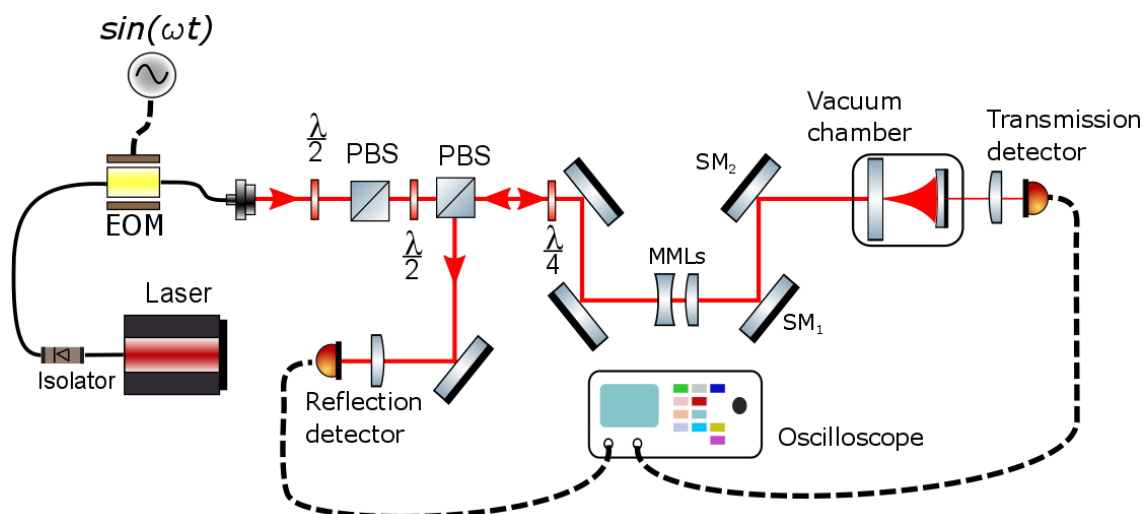


Figure 3.24: Setup used to characterize the optical cavity. Please note that the network analyzer providing the RF input to the EOM is here indicated simply as a function generator to avoid any confusion about its use in this scheme.

#### 3.3.7.1 Cavity escape efficiency

Optical losses due to coupling light to the resonator can be quantified from the time spectrum of the light transmitted through a cavity and reflected from it. In other words, referring to Eq. 3.29 we seek to estimate the ratio between the incoupling and outcoupling losses over the total optical losses of the cavity

$$\eta_{esc} = \frac{k_{ex}}{k} \quad (3.50)$$

where  $\eta_{esc}$  is usually referred to as *escape efficiency* or *overcoupling factor* of the cavity. First of all, we need to quantify the mode-matching efficiency  $\eta_{MM}$  of input light to  $TEM_{00}$ . This is rather straightforward when looking at the time spectrum of light transmitted through the cavity,

as it corresponds to the ratio between the power of the fundamental mode  $P_{TEM_{00}}$  and the sum of the power in all the modes  $P_i$

$$\eta_{MM} = \frac{P_{TEM_{00}}}{\sum_i P_i} \quad (3.51)$$

Assuming a linear behaviour of our detector, converting optical power into voltage, we obtain

$$\eta_{mm} = \frac{V_{TEM_{00}}}{\sum_i V_i} \quad (3.52)$$

The value of  $\eta_{mm}$  is strictly dependent on the input light being well-aligned to the cavity. Mechanical relaxation of the optical components' mounts tends to misalign the beam and this needs to be constantly steered back onto its path. Thus  $\eta_{mm}$  undergoes small changes in the order of few percents over time. This also means that if different light beams are steered into a cavity, the cavity escape efficiency needs to be characterized for each of them independently. In order to avoid any error in our data analysis, transmission and reflection time spectra were recorded for each beam interacting with our cavities immediately before any measurement sensitive to the value of  $\eta_{esc}$ . Here we present some spectra from the horizontal cavity setup as an example in Fig. 3.25. Fitting lorentzian curves to the individual transmission modes, a mode-matching efficiency of 0.97 was obtained for this dataset.

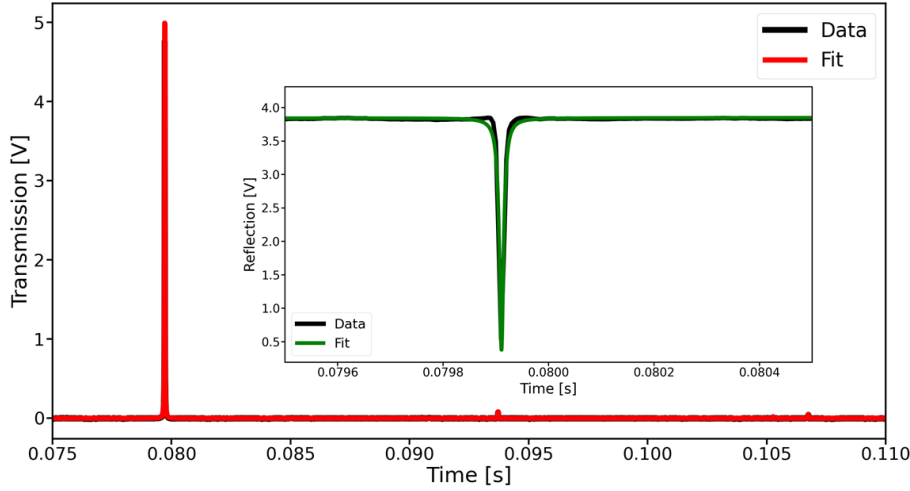


Figure 3.25: Example of transmission time spectra recorded for the horizontal cavity while scanning the frequency of a Toptica CTL1550 laser. Fitting lorentzian functions to the peaks enables to evaluate the mode-matching efficiency  $\eta_{mm}$ . Combining this with the information obtained from the reflection spectrum (see inset) allows to estimate the intracavity losses  $\mathcal{L}$ , hence the cavity escape efficiency.

From the reflection time spectrum, the values of power reflected by the cavity at resonance  $P_{res}$  and the input power  $P_{in}$ —reflected when light is off resonance—can be deduced. The intracavity losses  $\mathcal{L}$  can be calculated

$$\mathcal{L} = \mathcal{T}_{in} \frac{1 - \sqrt{\frac{P_{res} - (1 - \eta_{mm})P_{in}}{\eta_{mm}P_{in}}}}{1 + \sqrt{\frac{P_{res} - (1 - \eta_{mm})P_{in}}{\eta_{mm}P_{in}}}} \quad (3.53)$$

where  $\mathcal{T}_{in}$  is the transmissivity of the incoupling mirror. The escape efficiency is then given by

$$\eta_{esc} = \frac{1 - \sqrt{1 - \mathcal{T}_{in}}}{2 - \sqrt{1 - \mathcal{T}_{in}} - \sqrt{1 - \mathcal{L}}} \quad (3.54)$$

For the case we present here as an example, the intracavity losses add up to  $2 \times 10^{-4}$ , hence we have  $\eta_{esc} = 0.73$ .

### 3.3.7.2 Optical losses and efficiencies

Having estimated the cavity escape efficiency  $\eta_{esc}$ , we now have a complete overview of what the sources of optical loss are in our setup. We can thus define the *total detection efficiency*  $\eta$

$$\eta = \eta_{esc} \nu^2 \eta_{QE} \eta_{opt} \quad (3.55)$$

where  $\nu$  is the visibility of our homodyne setup and  $\eta_{QE}$  is the quantum efficiency of the photodiodes used for homodyne detection.  $\eta_{opt}$  is the efficiency related to losses due to the optical components in the setup.

### 3.3.7.3 Optical linewidth

We previously showed how to use the time spectrum of the light transmitted through the cavity to estimate how efficiently light is coupled in. One more piece of information we would like to extract is the linewidth of the cavity resonance in terms of frequency. In order to achieve this, we need to calibrate the x-axis of our time spectra using a known frequency reference. One way consists in applying a phase modulation with frequency  $f_{mod}$  to the input light through an electro-optic modulator (EOM)—essentially a voltage-controlled waveplate—as shown in Fig. 3.24. Such modulation produces sidebands around the beam carrier appearing at a spacing of  $f_{mod}$  in frequency domain. If the laser frequency or cavity length is scanned slowly enough compared to the cavity ring-down time  $1/k$ , in transmission these sidebands will appear as Lorentzian curves with a spacing of  $t_{mod}$  from the carrier. As varying the modulation frequency changes the distance  $t_{mod}$  proportionally (see Fig. 3.26a), when comparing the frequency spectrum to the one in time domain, we obtain the relation

$$\frac{f_{mod}}{t_{mod}} = \frac{k}{k_t} \quad (3.56)$$

where  $k_t$  is the cavity linewidth in time domain. Fitting Lorentzian curves to the carrier peak and sidebands, the  $f_{mod}$  vs  $\frac{t_{mod}}{k_t}$  curve can be reconstructed (see Fig. 3.26b). A simple linear fit allows us to estimate a linewidth of 15.19 MHz for the vertical cavity. In the horizontal-cavity setup, two different lasers are operated simultaneously, producing what we call *probe* and *cooling* beams. Their wavelength is tuned in such a way that each excites a cavity longitudinal mode separated from the other by at least one FSR. The linewidth corresponding to the two excited modes is not necessarily the same. In the first version of the horizontal cavity, both cavity modes feature a linewidth around 18.07 MHz and no appreciable difference between them. In the second version a linewidth of 18.85 MHz and 18.60 MHz was found for the probe and cooling beam, respectively.

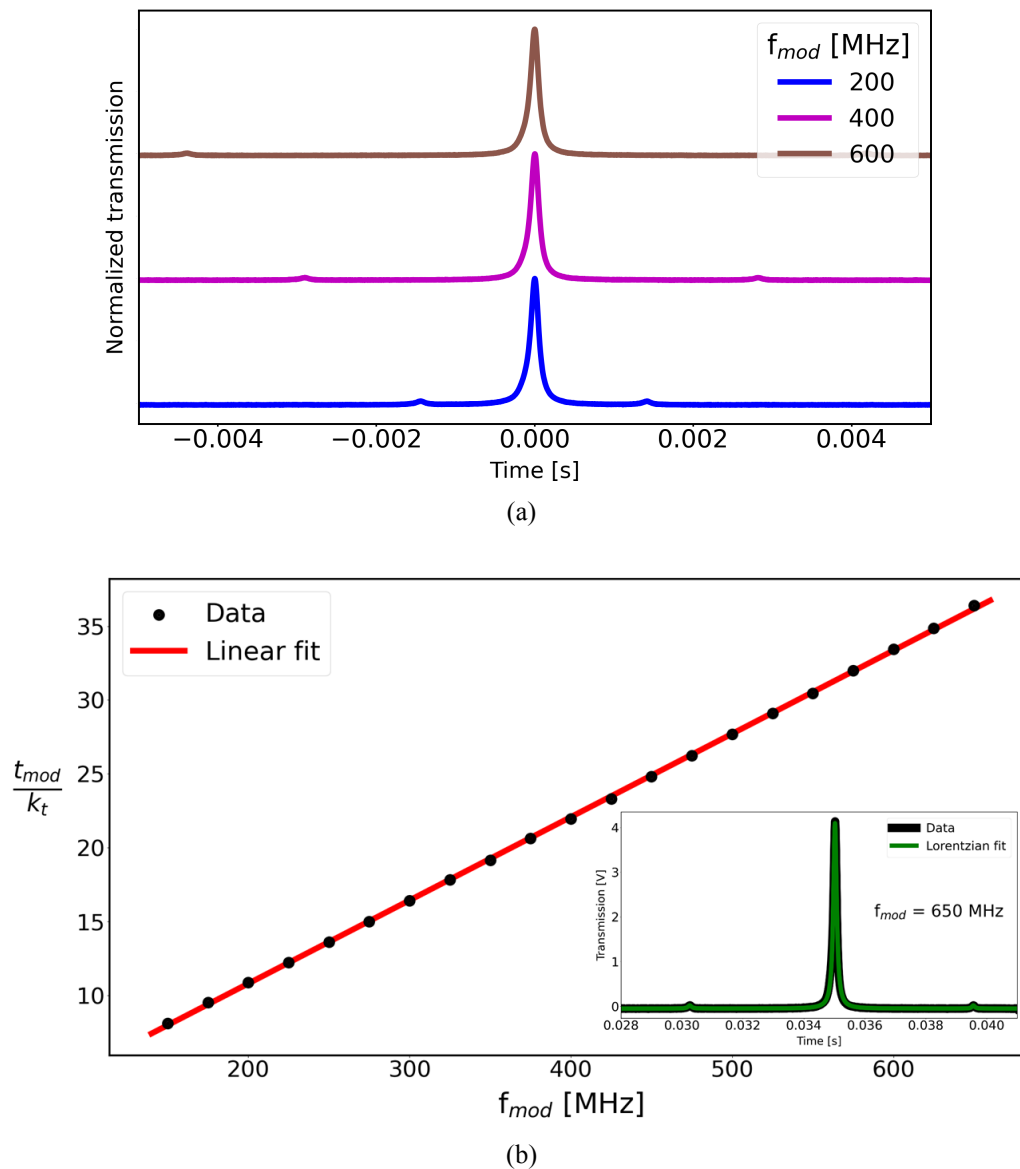


Figure 3.26: a) Phase modulation of the light brings about the appearance of sidebands around the beam carrier at a distance of  $\pm f_{mod}$  in frequency domain. The purple and brown curves were offset with respect to the blue one for better display. b) The horizontal-cavity transmission was recorded for different modulation frequencies and Lorentzian curves were fitted to the carrier and sideband peaks in each time trace (see an example in the inset). The cavity linewidth in terms of frequency can be determined from the slope of a linear fit to the  $f_{mod}$  vs  $\frac{t_{mod}}{k_t}$  data.

## 3.3.7.4 FSR, estimate of effective cavity length and finesse

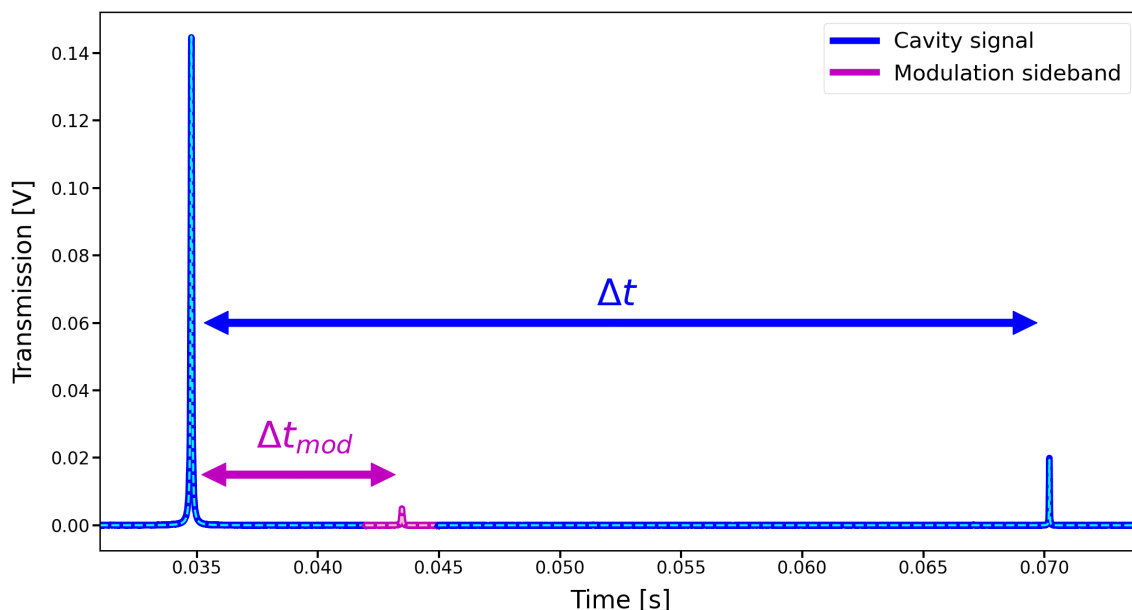


Figure 3.27: Transmission from our second horizontal cavity showing the  $TEM_{00}$  (left, in blue) and  $TEM_{10}$  (right, in blue) modes. The latter is enhanced by inducing a small misalignment of the incoming light path using steering mirrors placed before the cavity. The magenta peak in the middle represents the sideband created by driving the EOM at a fixed frequency of 3 GHz. Peaks were fitted to Lorentzian curves (dashed lines) in order to extract their positions and calculate the time spacing  $\Delta t$  between the fundamental and first higher-order modes. This value is then converted into frequency by comparison with the time spacing  $\Delta t_{mod}$  between the fundamental mode and the sideband produced by phase-modulation of the incoming light.

When presenting the designs of our optomechanical assemblies in Sec. 3.3.4 we gave specific values for the cavity length (see Table 3.1). One might be tempted to accept them as the real ones and derive the cavity FSR from them using Eq. 3.22. This would be a mistake. Several factors affect the cavity length, such as fabrication imprecision, errors in assembling or bending of metal parts under the pressure exerted by the screws. More importantly, the *effective* cavity length is different from its physical length due to the penetration depth of the intracavity field inside the mirror coatings. All these uncertainties bring about the need to carry out an estimation of the FSR through experimental measurements.

Different methods can be used to measure the FSR of an optical cavity. Our approach consists in introducing a small misalignment in the laser beam path to the cavity using the steering mirrors, thus exciting the first higher-order Hermite-Gauss mode  $TEM_{10}$  (see Fig. 3.27). Using Eq. 3.48 we can determine the difference in frequency with respect to the  $TEM_{00}$  mode

$$\delta\nu = |f_{010} - f_{000}| = \frac{c}{2\pi L} \arccos\left(\sqrt{1 - \frac{L}{R}}\right) \quad (3.57)$$

The corresponding time spacing  $\Delta t$  between these two modes can be measured simply by detecting the light transmitted through the cavity while scanning the laser wavelength or cavity length (see Fig. 3.27). A ruler to convert this value into frequency is provided by phase modulating the light at a fixed frequency  $f_{mod}$  and using the relation

$$\frac{\Delta t}{\Delta t_{mod}} = \frac{\delta\nu}{f_{mod}} \quad (3.58)$$

where  $\Delta t_{mod}$  represents the time spacing between the TEM<sub>00</sub> mode and the phase-modulation sideband. Using this method we obtained an effective cavity length of 1.02 mm for our vertical cavity and 1.863 mm and 1.614 mm for the first and second version of our horizontal cavity, respectively. Through Eq. 3.22, these correspond to FSR values of 146.96 GHz, 80.47 GHz and 92.89 GHz, respectively.

A widely-tunable laser was employed to align the light path to our horizontal cavities. This kind of device usually features an internal wavemeter that can be used to characterize the cavity FSR. While scanning the laser frequency, the amplitude of the voltage ramp to the internal piezo is set to the minimum value enabling a scan through the cavity resonance. Smaller amplitudes would lead to a deformation of the resonance shape due to the piezo turnaround. A marker is set at the time position of the fundamental mode peak and the central-wavelength of the frequency scan is recorded. Sweeping its value until a new cavity resonance overlaps to the marker allows to measure the FSR in terms of wavelength difference. For the first horizontal cavity we assembled, resonances were detected at the central wavelength of 1549.7425 nm and 1550.3915 nm. This difference of 0.649 nm corresponds to a FSR of 80.98 GHz and, through Eq. 3.22, to an estimate of the cavity length of 1.851 mm. Analogously, a FSR of 93.28 GHz was estimated for the second horizontal cavity we assembled, corresponding to a cavity length of 1.607 mm. Please note these values are in good agreement with the ones obtained from the former method.

We can now determine the finesse of our cavities, simply using Eq. 3.26. A finesse of 9800 is obtained for our vertical cavity, while values of 4500 and 4928 are computed for first and second version horizontal cavity, respectively. These values are significantly lower than the expected ones reported in Table 3.1. One first reason to that might be damage to the mirrors, increasing their transmissivity. This is probably the case for both the vertical cavity and the second horizontal cavity, whose spherical mirrors appear clearly scratched to close inspection. One must then remember that Eq. 3.28 neglects the effects of losses, assuming almost perfect mirrors. Nevertheless, there might be more to this discrepancy. As a matter of fact, for dispersive optomechanical systems like ours, the mechanical resonator divides the cavity into two smaller, strongly-interacting subcavities. Hence the model on which Eq. 3.28 is based might be oversimplified.

### 3.3.8 Frequency locking

In this chapter we pointed out several times how the cavity resonance features Lorentzian intensity in frequency domain. As a consequence, if the frequency of the laser input differs from the cavity resonance frequency by more than  $\frac{k}{2}$ , most of the input light will not enter the cavity. Unfortunately it is basically impossible to build a macroscopic cavity which is always on resonance with a given single-frequency laser. Nevertheless, most laser devices feature a degree of wavelength tunability that can be used to adjust the frequency to the cavity resonance. Conversely, a cavity mirror can be bound to a piezo actuator to continuously vary the cavity length in order to match the laser wavelength. Even so, a variety of phenomena such as temperature fluctuations or laser gain dynamics will cause the two frequencies to drift away from each other, hence their difference needs to be constantly readjusted to zero. This procedure is usually referred to as *frequency locking*. The idea is rather simple: the frequency difference between the cavity and the laser is continuously monitored, producing a so called *error function* or *error signal*. This is then fed to an electronic controller (typically a PID) which applies the necessary changes to bring its value back to a chosen, fixed level (*feedback*). Different types of frequency-locking schemes can be implemented, depending on how the error function is generated.

## 3.3.8.1 Pound-Drever-Hall scheme

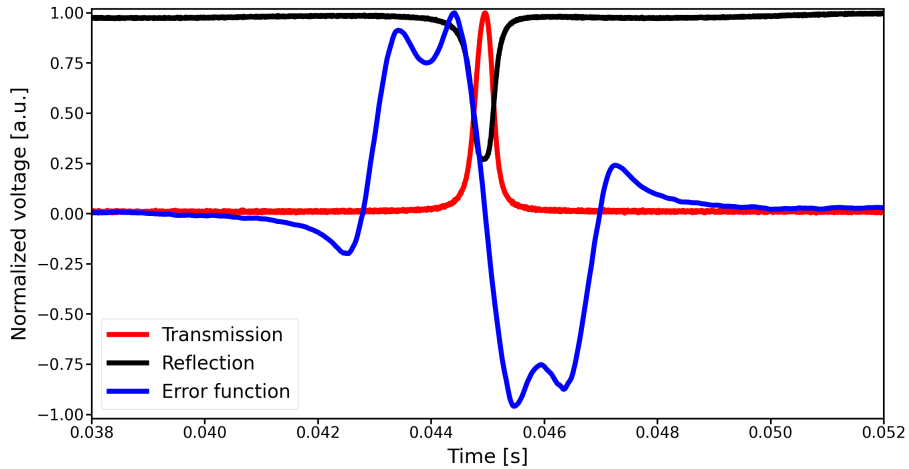


Figure 3.28: Transmission and reflection from the cavity are displayed as they appear while scanning the laser frequency. The blue curve shows the PDH error function obtained demodulating the reflection signal upon phase modulation of the input light. Each curve was normalized to its maximum value.

The main frequency-locking scheme we used for the experiments described in this work is the Pound-Drever-Hall (PDH) technique [30]. A phase modulation of frequency  $\omega_{mod} \gg k$  is applied to the light impinging onto the cavity

$$E_{in} = E_0 e^{i(\omega t + \beta \sin \omega_{mod} t)} \quad (3.59)$$

where  $\beta$  is usually referred to as *modulation depth*. If this modulation is weak (meaning  $\beta$  is small), we can disregard the terms of order higher than 1 in the Jacobi-Anger expansion and rewrite Eq. 3.59 in terms of Bessel functions

$$E_{in} \approx E_0 \left[ J_0(\beta) e^{i\omega t} + J_1(\beta) e^{i(\omega + \omega_{mod})t} - J_1(\beta) e^{i(\omega - \omega_{mod})t} \right] \quad (3.60)$$

This shows how phase modulation brings about three components in the impinging beam: a carrier at frequency  $\omega$  and two (first-order) sidebands at frequencies  $\omega \pm \omega_{mod}$ . The total incident power  $P_0 = |E_0|^2$  is then redistributed among the three components according to

$$P_c = J_0^2(\beta) P_0 \quad (3.61a)$$

$$P_{sb} = J_1^2(\beta) P_0 \quad (3.61b)$$

where  $P_c$  and  $P_{sb}$  represent the power in the carrier and in the sidebands, respectively. A reflection coefficient  $F(\omega)$  can be defined as ratio between the amplitudes of the reflected and input electric fields

$$F(\omega) = \frac{E_{ref}}{E_{in}} = \frac{r \left[ \exp\left(i \frac{\omega}{f_{FSR}}\right) - 1 \right]}{1 - r^2 \exp\left(i \frac{\omega}{f_{FSR}}\right)} \quad (3.62)$$

where a lossless, symmetric cavity has been assumed. Close to resonance,  $F$  is almost purely imaginary, with  $Im [F(\omega)] > 0$  above resonance and  $Im [F(\omega)] < 0$  below resonance. Each of the three components impinging onto the cavity will be reflected with a frequency-dependent coefficient, so that the total reflected power is given by

$$\begin{aligned}
 P_{ref} = & P_c |F(\omega)|^2 + P_{sb} \left[ |F(\omega + \omega_{mod})|^2 + |F(\omega - \omega_{mod})|^2 \right] + \\
 & + 2\sqrt{P_c P_{sb}} \Re [F(\omega) F^*(\omega + \omega_{mod}) - F^*(\omega) F(\omega - \omega_{mod})] \cos \omega_{mod} t + \\
 & + \Im [F(\omega) F^*(\omega + \omega_{mod}) - F^*(\omega) F(\omega - \omega_{mod})] \sin \omega_{mod} t + 2\omega_{mod} \text{ terms}
 \end{aligned} \tag{3.63}$$

The reflected power features a beat pattern with components oscillating at  $\omega_{mod}$  arising from the interference between carrier and sidebands and at  $2\omega_{mod}$  stemming from the interference between sidebands. Attention is then drawn to the  $\omega_{mod}$  terms as they sample the phase of the reflected carrier. Choosing  $\omega \pm \omega_{mod}$  causes the sidebands to be completely reflected when the carrier is near resonance, hence we have

$$F(\omega \pm \omega_{mod}) \approx -1 \tag{3.64}$$

$$F(\omega) F^*(\omega + \omega_{mod}) - F^*(\omega) F(\omega - \omega_{mod}) \approx -2i \Im [F(\omega)] \tag{3.65}$$

As the left-side term in Eq. 3.65 is purely imaginary, only the sine term in Eq. 3.63 will survive. Since  $\Im [F(\omega)]$  is antisymmetric around resonance, we can deduce whether the laser frequency is above or below the cavity resonance from this sine term, simply by demodulating and applying a low-pass filter. Please note that the demodulation is performed by mixing our signal with a different one  $\sin \omega_{mod} t$  from the same modulation source. Our error signal is then

$$\epsilon_{PDH} = -2\sqrt{P_c P_{sb}} \Im [F(\omega) F^*(\omega + \omega_{mod}) - F^*(\omega) F(\omega - \omega_{mod})] \approx 4\sqrt{P_c P_{sb}} \Im [F(\omega)] \tag{3.66}$$

Let us now try to see through the formulas and look at what they mean. In the impinging light beam, the higher-frequency sideband is in phase with the carrier, while the lower-frequency sideband is out of phase by  $\pi$ . In reflection, if there is no phase shift of the carrier or the sidebands with respect to each other, the detected photocurrent will carry no signal at the modulation frequency, as the signals produced by the beating the carrier with the two sidebands cancel each other out. When the carrier crosses the cavity resonance, it acquires a phase shift while the sidebands are unaffected since they are too far away ( $\omega_{mod} \gg k$ ). The signals produced by the interaction between carrier and sidebands will then differ and not cancel each other out, thus yielding a net photocurrent at the modulation frequency.

Fig. 3.28 shows a comparison between reflection (black), transmission (red) and the error function obtained through the PDH scheme (blue). As we can see, the error function is linear within the cavity linewidth, hence it can be used to determine whether the laser is detuned to the red or blue side of the cavity. It can be proven that an error function of the same shape is generated demodulating and low-passing the transmission signal instead of the reflection.

The Pound-Drever-Hall method is designed to prevent several issues [31]. First off, since it is based on phase modulation instead of amplitude modulation, the feedback loop can generally distinguish between the changes in intensity due to the frequency drifting away from resonance and

those caused by fluctuations in the laser intensity, which are not coupled into the error signal. Besides, the PDH scheme allows use of modulation frequencies far above DC, thus bringing about a great reduction of the electronic noise contribution to the error function.

### 3.3.8.2 Different implementations of PDH scheme

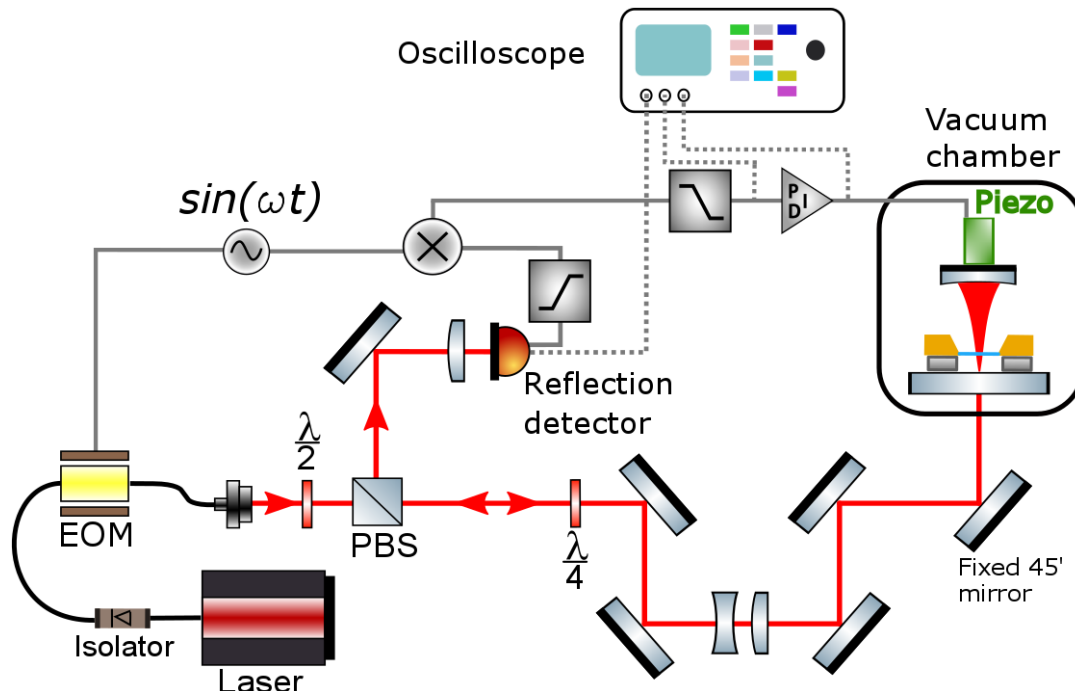


Figure 3.29: Implementation of PDH frequency-lock scheme for our vertical cavity setup. Light reflected off the cavity produces a photocurrent signal which is then demodulated by an analog circuit consisting of a mixer and a low-pass filter. The same function generator provides both the drive signal to the EOM and the beat signal for the demodulation circuit. The error function is fed to an analog PID. This controls the cavity length through a piezo actuator in order to keep its resonance locked to the laser frequency. An oscilloscope monitors the reflection signal, the error function and the output of the PID.

The two feedback-cooling experimental setups we present in this work are based on different implementations of the PDH frequency-lock scheme. In the vertical cavity setup (Fig.3.29), a dual-channel function generator drives an iXblue MPZ-LN-10 EOM at a frequency of 28 MHz. The phase-modulated light beam is reflected off the cavity and detected by a Thorlabs APD430C/M avalanche photodetector. Its output signal is demodulated by mixing with a 28 MHz tone on an analog circuit and then applying a low-pass filter with a cut-off frequency of 1 MHz. It is important to highlight that the same function generator provides both the driving signal to the EOM and the local oscillator for the mixer, so that their relative phase difference does not drift. Moreover, this enables to optimize the shape of the error function by tuning the initial phase of either signal in the function generator, thus compensating for any phase delay in our setup. The error function is then fed to an analog PID controller, whose output controls the cavity length by actuating a Piezomechanik HPSt low-voltage piezo bound to the spherical mirror. The piezo maximum stroke is about 16  $\mu\text{m}$ , enough to scan through several multiples of the cavity FSR. The piezo resonance frequency with no weight load attached is about 30 kHz, high enough to avoid being excited by the PID output. The plane mirror is not piezo-actuated to avoid coupling of the voltage noise to the mechanical resonator. A Rohde & Schwarz RTM2054 oscilloscope monitors the reflection signal, the error function and the PID output.

In the horizontal-cavity setup (Fig.3.30a), an EOM modulates the phase of our NKT Koheras Ad-

justik E15 laser with a frequency of 35 MHz (first horizontal cavity) or 14 MHz (second horizontal cavity). A fiber polarization controller is used to ensure the predefined input polarization direction of the EOM is matched, otherwise residual polarization in the perpendicular direction may result in amplitude modulation of our beam. Light transmitted through the cavity is detected with a Thorlabs APD430C/M avalanche photodetector, whose output is amplified and then passed to a RedPitaya 125-14 FPGA digital controller. We use the software modules from PyRPL, an open-source, Python-based package to run this RedPitaya [21]. In particular, using the IQ module we drive the EOM, high-pass, frequency-mix and then low-pass again the transmission signal, thus generating the PDH error function (see Fig. 3.30b). The PID module is used to lock the laser frequency to our cavity resonance. Since the RedPitaya outputs a single-ended signal between 0 and 2 V while our laser accepts a differential input between 0 and 5 V, a THS4531ADGKEVM evaluation module from Texas Instruments applies a fixed gain of 2.5 and provides an interface between the two devices. Finally, the PyRPL oscilloscope module was used to monitor the transmission signal, the error function and the PID output.

A slightly different version of the PDH technique described so far was applied to lock the Topica CTL1550 laser to our horizontal cavity. In this case the phase modulation to the laser is not provided by an external EOM, but rather modulating the current to the laser diode itself [32]. Detecting the light reflected from the cavity provides a signal which is fed back to the laser controller, whose electronics takes care of the modulation and demodulation operations. The PID controller for the frequency lock is managed by a proprietary software DLC pro Lock. We use a Thorlabs APD430C/M avalanche photodetector to detect the reflected light.

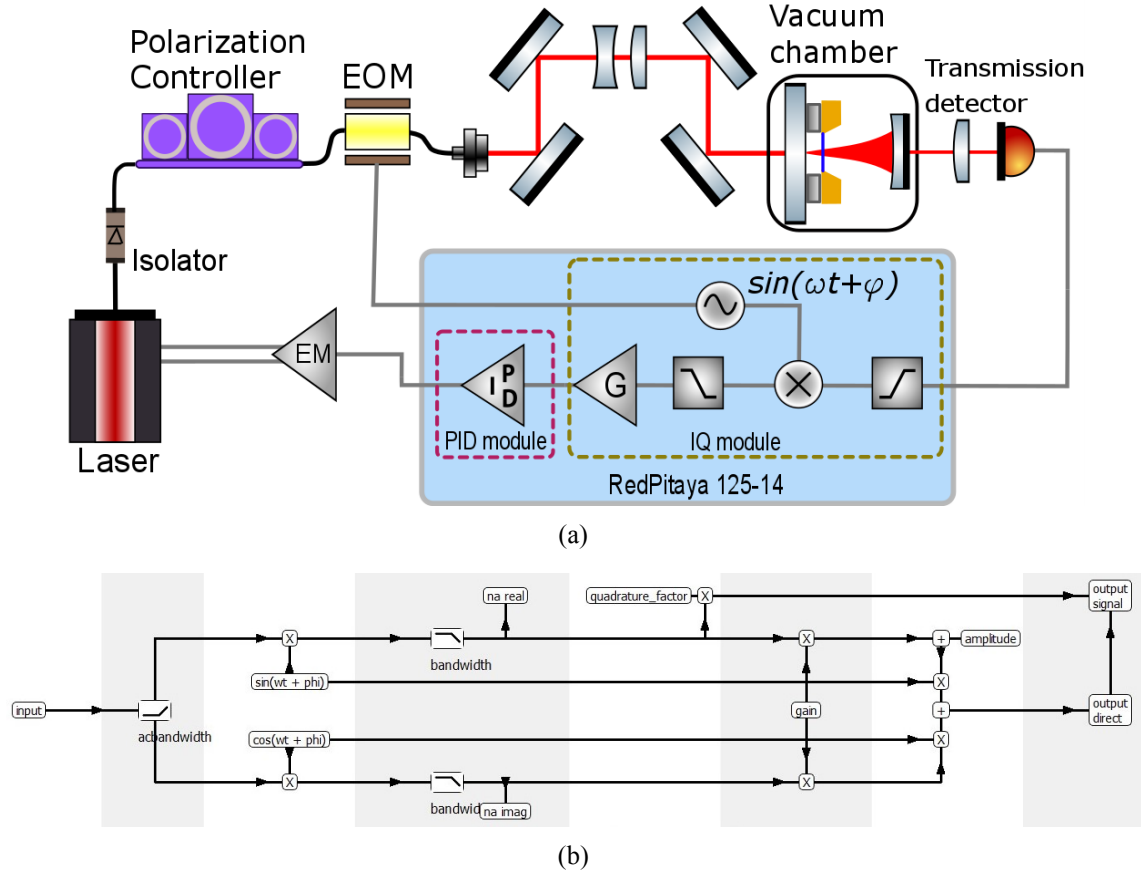


Figure 3.30: Implementation of PDH frequency-lock scheme for our horizontal cavity setup. a) Experimental setup. Light transmitted through the cavity generates the input signal to a RedPitaya which works as function generator, demodulation circuit, PID controller and oscilloscope. Its PID output is passed to an evaluation module which applies a fixed gain and converts the FPGA single-ended output into a differential signal. This controls the laser internal piezo in order to keep the laser frequency locked to the cavity resonance. b) Screenshot of the browser interface for the PyRPL IQ module showing the corresponding schematic. First the input goes through a high-pass filter, then it is split into two signals, one mixed with a sine function, the other with a cosine. Setting the gain to zero cancels the latter component, while the former is low-pass filtered and amplified by a quadrature factor before reaching the *output signal* port, thus providing our error function. The sine function used for down-mixing is multiplied by an *amplitude* factor, then redirected to the *output direct* port, which is used to drive the EOM. Adjusting the phase  $\phi$  of the sine function enables to optimize the shape of the error function.

### 3.3.8.3 Cavity detuning

So far, we mainly discussed the possibility to lock the laser frequency on the cavity resonance or vice versa, fixing the frequency difference between them (*detuning*) to zero. Sometimes applying a non-zero detuning can also be useful, as we will see later in this chapter. We typically do this by locking the frequency on resonance, then applying a voltage offset to the error function before feeding it to the PID. The applied detuning  $\Delta$  can be estimated by comparison of the transmission voltage signal  $V_t$  to its peak value  $V_p$ . The latter is measured by scanning the laser frequency across the cavity resonance. In units of cavity linewidth  $k$ , we obtain

$$\frac{\Delta}{k} = \frac{1}{2} \sqrt{\frac{V_p}{V_t} - 1} \quad (3.67)$$

### 3.4 Ringdown measurements of mechanical quality factor

When dealing with our mechanical resonators in Sec. 3.2.2 we defined their main physical property, that is to say the high quality factor of certain specific modes. We did not go through how this can be quantified because knowledge of the workings of our optical setup was considered necessary. Having covered such topic, it is now time to describe the ringdown method [17], which represents the most common technique to measure a mechanical quality factor.

Our mechanical resonators are designed to feature quality factors in the order of  $10^6$  or higher and vibrational frequencies ranging between 100 kHz and 1.5 MHz. This translates into a mechanical linewidth of hundreds of mHz at most, while the lowest resolution bandwidth a commercial spectrum analyzer can offer is typically 1 Hz. As a consequence, properly resolving our mechanical modes is not possible and direct estimation of the quality factor from the displacement spectrum is prevented. A way around this is found providing a strong excitation to the mechanical mode of interest and then observing its amplitude decay over time.

The time evolution of the mechanical amplitude  $u(t)$  can be described by

$$u(t) = u_0 e^{-\frac{\pi f_M t}{Q}} \quad (3.68)$$

with  $u_0$  being the initial value,  $Q_M$  the quality factor,  $f_M$  the mechanical frequency and  $\frac{\pi f_M}{Q_M}$  the decay rate. It is usually convenient to use decibel-based units, hence we can define

$$u_{dB}(t) = 20 \log_{10}(u(t)) \quad (3.69)$$

whose time derivative is given by

$$\frac{du_{dB}(t)}{dt} = -\frac{20\pi}{\ln 10} \frac{f_M}{Q_M} \approx -27.288 \frac{f_M}{Q_M} \quad (3.70)$$

Eq. 3.70 can then be used to derive the quality factor from the slope of the time decay in dB scale

$$Q_M = -\frac{20\pi}{\ln 10} \frac{f_M}{du_{dB}/dt} \approx -27.288 \frac{f_M}{du_{dB}/dt} \quad (3.71)$$

Fig. 3.31a shows how our horizontal-cavity optical setup was arranged for the characterization of the quality factor of our mechanical resonators. The sensing beam of light is provided by our NKT Koheras Adjustik E15, which is modulated both in phase—to lock its frequency to the cavity where the membrane is located—and in amplitude—to provide the excitation of the mechanical mode of interest. A fiber polarization controller is placed before the amplitude modulator in order to match its accepted input polarization and maximize the output optical power. Homodyne detection of the phase of the light reflected off the cavity enables mechanical displacement measurement. The spectrum is monitored using a spectrum analyzer, whose resolution bandwidth and frequency span are set to 100 Hz and 0 Hz, respectively. When the amplitude modulation is stopped, the time decay can be followed and the quality factor can be estimated. Fig. 3.31b shows the experimental data for the lowest-frequency bandgap mode of the phononic membrane we used in the second version of our feedback cooling experiment. Given a mechanical frequency of about 1.366 MHz, a quality factor of  $2.12 \times 10^6$  was estimated.

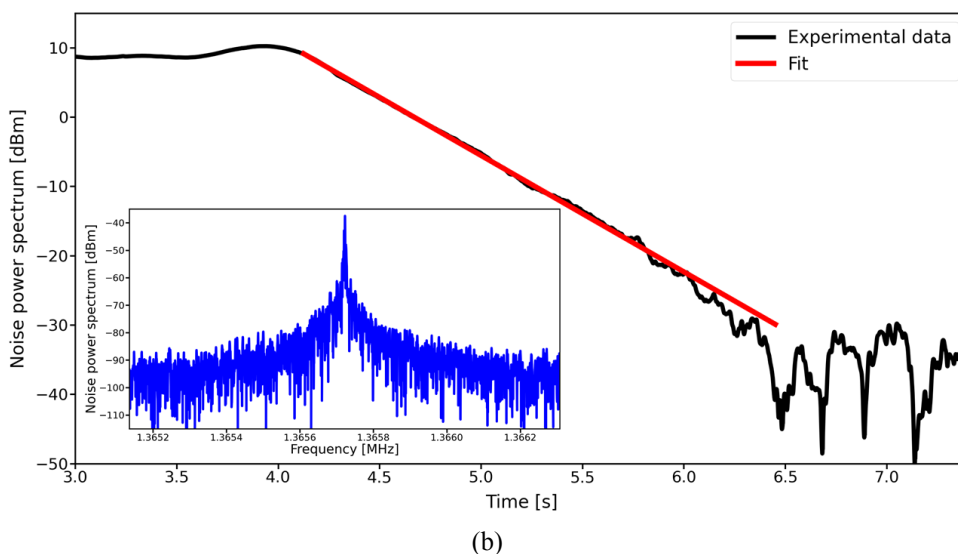
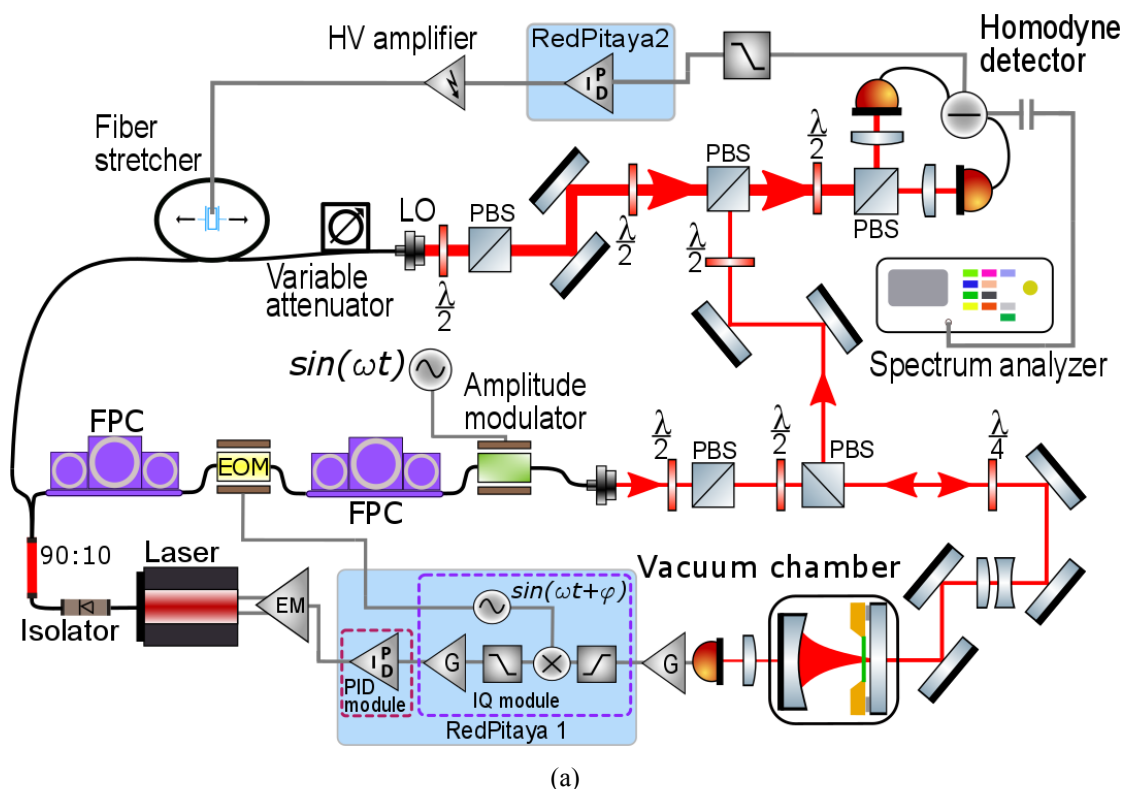


Figure 3.31: Ringdown measurements. a) Experimental setup. RedPitaya 1 and RedPitaya 2 are respectively used to handle the laser PDH frequency lock and the homodyne-detection phase lock. b) Mechanical ringdown measurement of the lowest-frequency bandgap mode in the phononic-crystal patterned membrane used for our feedback cooling experiment. Inset shows the displacement spectrum of the mode of interest.

### 3.5 Single-photon optomechanical coupling

The single-photon optomechanical coupling  $g_0$  is probably the most important experimental parameter in cavity optomechanics, as it quantifies the strength of the interaction between the optical and mechanical-displacement field. Complex models attempt to describe all the factors affecting its magnitude. Here we will refer to a rather simple one [33], considering a square membrane of

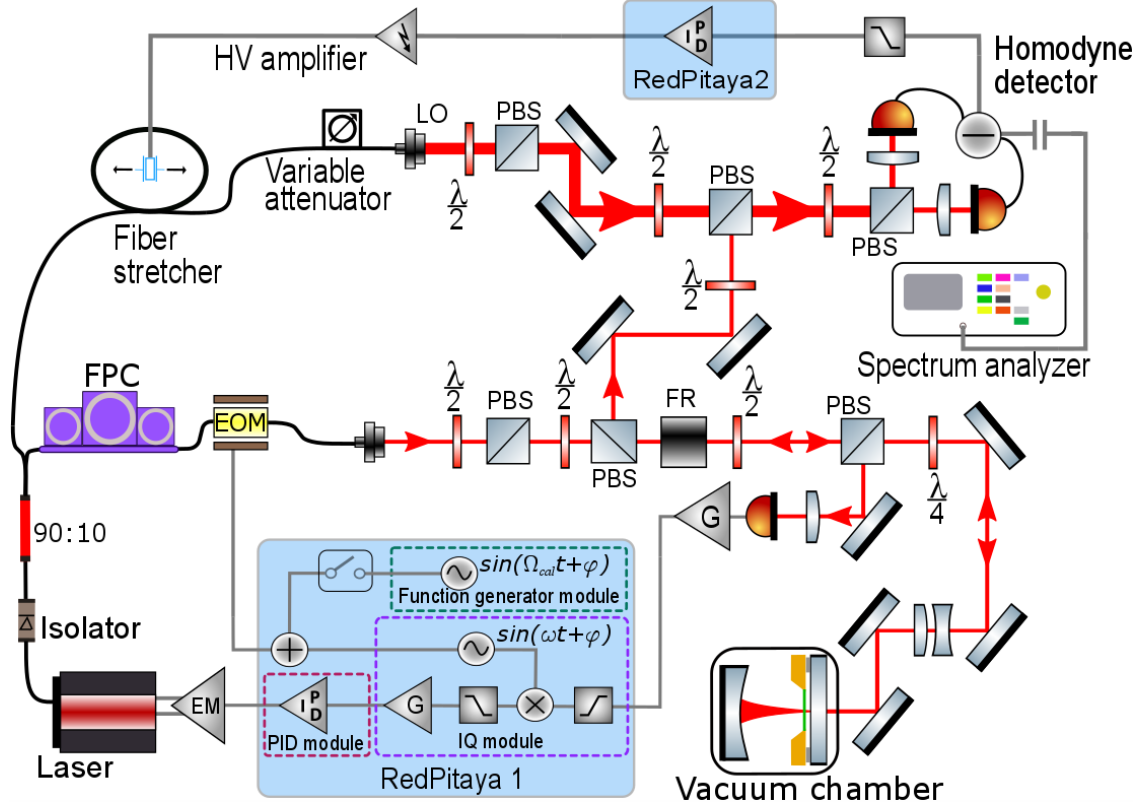


Figure 3.32: Setup arrangement to characterize the single-photon optomechanical coupling in our horizontal-cavity experiment. An analogous scheme was used for the vertical-cavity setup.

side length  $D$  located inside a Fabry-Perot cavity of length  $L$ . The oscillator is assumed to be made of dense material subject to high stress, so that the bending effects are irrelevant and its normalized vibrational normal modes are described by

$$\phi_{ij}(x, y) = \frac{2}{D} \sin\left(\frac{i\pi x}{D} + \frac{i\pi}{2}\right) \sin\left(\frac{j\pi y}{D} + \frac{j\pi}{2}\right) \quad (3.72)$$

with  $i, j = 1, 2, \dots$  and  $|x|, |y| \leq D/2$ . In the plane parallel to the membrane, the intracavity field mode of indices  $\{mnp\}$  features a normalized pattern given by

$$\tilde{T}_{mnp}(x, y) = \frac{H_n(\sqrt{2}x/w_0) H_m(\sqrt{2}y/w_0)}{w_0 \sqrt{\pi} 2^{n+m-1} n! m!} \exp\left(-\frac{x^2 + y^2}{w_0^2}\right) \quad (3.73)$$

where  $H_n(x)$  is the  $n$ th Hermite polynomial and  $w_0$  the cavity waist, while  $p$  defines the different longitudinal modes. The single-photon optomechanical coupling rate between a chosen cavity mode of frequency  $\omega_0$  and the mode  $\{ij\}$  of the membrane oscillating at frequency  $\Omega_{ij}$  is then

$$g_{mnp,ij} = \frac{2\hbar\omega_0}{L} \sqrt{\frac{\hbar}{m_{eff}\Omega_{ij}}} \Theta_{ij,mnp} \Lambda_p \quad (3.74)$$

where  $\Lambda_p$  describes the longitudinal component of the optical field. More importantly,  $\Theta_{ij,mnp}$  is the transverse overlap integral between the cavity mode  $\{mnp\}$  and the mechanical mode  $\{ij\}$

$$\Theta_{ij,mnp} = \frac{D}{2} \int_{-D/2}^{D/2} dx \int_{-D/2}^{D/2} dy \tilde{T}_{mnp} \phi_{ij}(x, y) \tilde{T}_{mnp} \quad (3.75)$$

Given the normalization of the involved mode functions, we have  $|\Theta_{i,mnp}| \leq 1$ . Eq. 3.74 gives us some rather meaningful insight on the nature of  $g_0$ . To begin with,  $g_0$  is inversely proportional to the cavity length, making smaller cavities more suitable for experiments where an intense optomechanical interaction is required. This is the reason why our cavities are designed to be as small as practical considerations allow. Furthermore, the coupling rate describes a one-on-one interaction between a specific cavity mode  $\{mnp\}$  and a specific membrane mode  $\{ij\}$ . For a given oscillator mass and cavity length, the optomechanical coupling primarily depends on the spatial overlap between these modes. This result also provides an a-posteriori justification for us to always work with the fundamental mode of both cavity and mechanics. The quality factor of our membranes is optimized only for their lowest-frequency mode, whose spatial profile has Gaussian shape in the plane perpendicular to the light propagation axis. Since the fundamental cavity mode has Gaussian profile as well, their overlap is expected to be the highest among all light-mechanics mode pairs. Among the several techniques allowing the characterization of  $g_0$ , here we will focus on two, respectively based on the optomechanical spring effect and quantum noise thermometry. Fig. 3.32 shows how our horizontal-cavity setup was rearranged to carry them out. A NKT Koheras Adjustik E15 laser was used. Unlike the other measurement schemes presented in this work, the PDH error function was generated by detecting the reflected light, using a Thorlabs PDA10CF-EC InGaAs photodetector. This choice was due to the need to carry out measurements at very low values of input optical power or to lock with detuning comparable to the cavity linewidth. In both cases, the intensity of the transmitted signal is too weak to produce a stable lock and strong frequency fluctuations appear. Please note that tapping off part of the reflected light and using it for frequency stabilization instead of homodyne measurement is not always a viable option. It is in this context only because the outcome of the characterization techniques presented here is not affected by detection losses. When performing feedback-cooling, optical losses have a detrimental role, hence we will adopt different strategies to avoid this tap-off. One more PBS was introduced before the cavity, followed by a quarter-wave plate. The latter can be rotated in such a way that a fraction of the light reflected by the cavity is also reflected off the PBS and focused onto the detector used for frequency-locking. A Faraday Rotator (FR) is used to change the polarization of the light reflected by the cavity and steer it towards the homodyne-detection setup. For the thermometry measurements, an additional driving signal is sent to the EOM beside the one necessary for PDH locking. The RedPitaya architecture allows to use several PyRPL function-generator modules simultaneously and to sum their outputs directly on the FPGA board. This removes the need for external function generators and analog signal combiners and prevents problems due to impedance mismatch between the different devices.

### 3.5.1 Optomechanical spring effect

Cavity optomechanics is all about the two-level interaction between the intracavity light field and the mechanical resonator. The radiation pressure causes a mechanical displacement, which in return affects the intracavity photon number, hence the intensity of the radiation pressure itself. This dynamical interaction gives rise to a stiffening or softening of the mechanical spring constant which corresponds to a change in the mechanical resonance frequency [34]. Let us consider a 1D model where  $x$  is the amplitude of mechanical motion in a reference system centered at the resonator equilibrium position. Our mechanical resonator is subject to a potential

$$V(x) = \frac{m_{eff} \Omega_M^2}{2} x^2 - \frac{1}{2} \hbar k N_{cav}^{max} \arctan \left( 2 \frac{\frac{g_0}{x_{zpf}} x + \Delta}{k} \right) \quad (3.76)$$

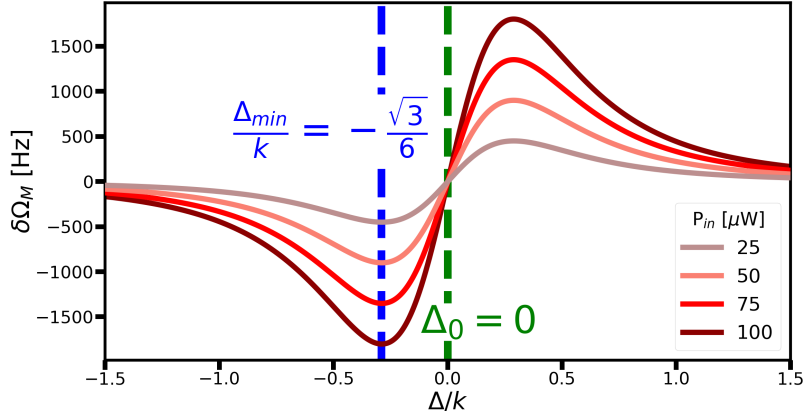


Figure 3.33: Optomechanical spring effect was simulated for different values of input optical power  $P_{in}$  and parameters  $\frac{g_0}{2\pi} = 10$  Hz,  $\eta_{esc} = 1$ ,  $\frac{k}{2\pi} = 15$  MHz and  $\lambda = 1550$  nm. The blue dashed line indicates the value  $\frac{\Delta_{min}}{k} = -\frac{\sqrt{3}}{6}$  corresponding to the minimum frequency shift. On the other hand, when the cavity is on resonance with the incoming light, no frequency shift is induced ( $\Delta_0 = 0$ , green dashed line).

with  $m_{eff}$  being the resonator effective mass and  $\Omega_M$  the mechanical angular frequency.  $N_{cav}^{max} = \frac{4\eta_{esc}}{\hbar\Omega_L k} P_{in}$  represents the maximum number of intracavity photons (obtained at zero detuning) for a given input optical power  $P_{in}$  and laser angular frequency  $\Omega_L$ . Looking at Eq. 3.76, we see  $V(x)$  contains two contributions. The first is given by the intrinsic harmonic restoring potential of our resonator, while the second describes the effect of radiation pressure. The latter term changes the spring constant by an amount  $\delta k_{spring} = \frac{\partial^2 V_{rad}(x_0)}{\partial x^2}$  where  $x_0 \neq 0$  is the new mechanical equilibrium position, with  $\frac{\partial V(x_0)}{\partial x} = 0$ . This phenomenon is usually referred to as *optomechanical spring effect*. The change in spring constant corresponds to a shift in mechanical resonance frequency that can be quantified by imposing  $\frac{\partial^2 V_{rad}(0)}{\partial x^2} = m_{eff} \delta (\Omega_M^2)$ . In the bad cavity regime ( $k \gg \Omega_M$ ) and for low light intensity ( $g_0 \sqrt{N_{cav}} \ll k$ ), we obtain

$$\delta\Omega_M = 8\Delta \left(\frac{g_0}{k}\right)^2 \frac{N_{cav}^{max}}{\left[1 + \left(\frac{2\Delta}{k}\right)^2\right]^2} \quad (3.77)$$

Please note  $\delta\Omega_M$  depends nonlinearly on the detuning but linearly on the input optical power through  $N_{cav}^{max}$ . Fig. 3.33 displays the behaviour Eq. 3.76 and shows the frequency shift is minimum for  $\Delta_{min} = -\frac{\sqrt{3}}{6}k$ . In terms of input power, the minimum frequency shift is

$$\delta\Omega_M^{min} = \delta\Omega_M \Big|_{\Delta_{min} = -\frac{\sqrt{3}}{6}k} = -\frac{3\sqrt{3}\eta_{esc}}{\hbar\Omega_L} \left(\frac{g_0}{k}\right)^2 P_{in} \quad (3.78)$$

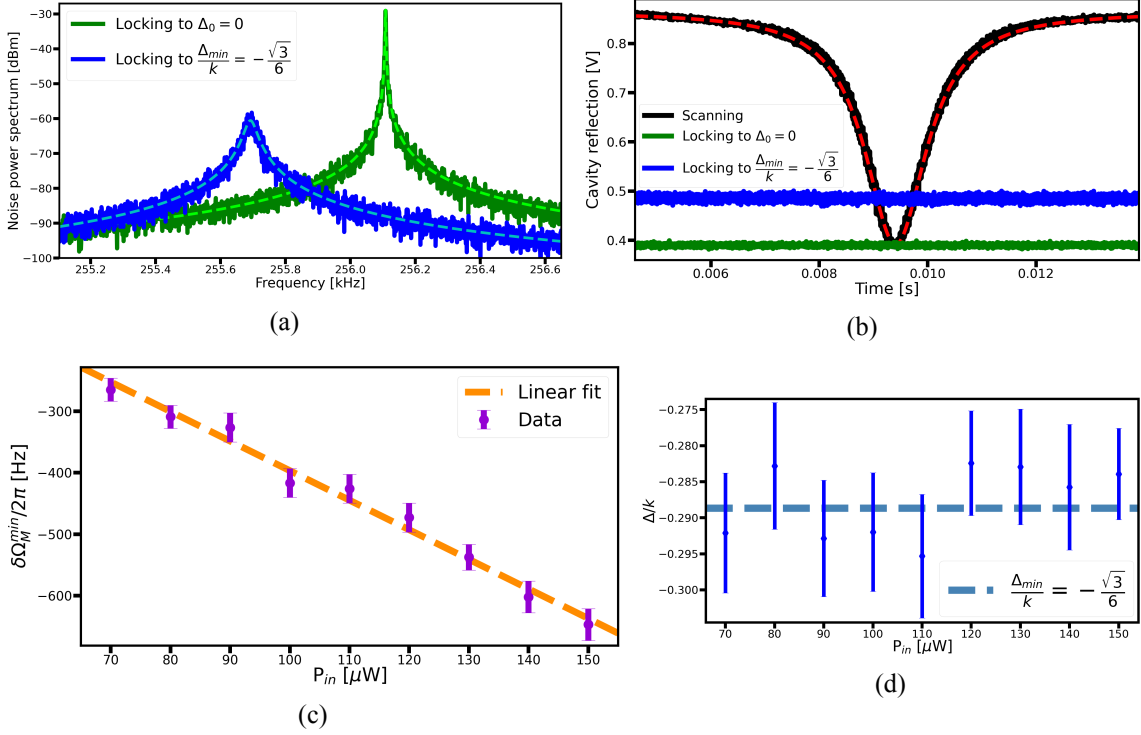


Figure 3.34: Characterization of  $g_0$  through measurement of optomechanical spring-effect of a topology-optimized trampoline in our horizontal-cavity experiment. a) Homodyne measurements of the mechanical spectrum were carried out for both  $\frac{\Delta_{min}}{k} = -\frac{\sqrt{3}}{6}$  (blue trace) and  $\Delta_0 = 0$  (green trace), using light reflected from the cavity to generate the PDH error function (Fig. b). Dashed lines in Figs. a and b represent fitting to Lorentzian functions. c) Measuring the frequency shift  $\delta\Omega_M^{min}$  between the two mechanical peaks for different values of the input power  $P_{in}$  and fitting the data to Eq. 3.78 allows to determine the value of  $g_0$ . d) Detuning values for which the PSD of down-shifted mechanical modes was recorded. All data points fall within one standard deviation from  $\frac{\Delta_{min}}{k} = -\frac{\sqrt{3}}{6}$ .

The optical detuning also results in a change of mechanical damping rate  $\Gamma_M$  into an effective value  $\Gamma_{eff} = \Gamma_M + \Gamma_{opt}$ , with

$$\Gamma_{opt} = g_0^2 \frac{N_{cav}^{max}}{1 + \left(\frac{2\Delta}{k}\right)^2} \left( \frac{k}{\frac{k^2}{4} + (\Delta + \Omega_M)^2} - \frac{k}{\frac{k^2}{4} + (\Delta - \Omega_M)^2} \right) \quad (3.79)$$

As  $\Gamma_{opt}$  can be positive or negative, this leads to either an increase or decrease of the mechanical damping, hence to cooling or amplification of the thermal fluctuations. Such a shift in damping rate is a consequence of the optomechanical dynamical backaction, with the mechanical displacement affecting the force applied by the light on the oscillator itself through radiation pressure. When the incoming laser is detuned from the cavity, a phase delay occurs between the two, creating a force component out of phase with the mechanical motion. In a thermodynamical picture, this means the radiation pressure force applies a non-zero work on the mechanical resonator, corresponding to an increase (amplification) or decrease (cooling) of the stored mechanical energy [34].

The optomechanical spring effect can be exploited to determine the optomechanical coupling. For a given input power value, the laser is locked on resonance with the cavity ( $\Delta_0 = 0$ , green trace in Fig. 3.34b) and a homodyne spectrum of the back-reflected light is recorded, displaying a me-

chanical mode at frequency  $\Omega_M/2\pi$  (green peak in 3.34a). The laser is then red-detuned from the cavity and a down-shift of the mechanical frequency is observed. The amplitude of such detuning is increased until the mechanical frequency hits a minimum at  $(\Omega_M + \delta\Omega_M^{min})/2\pi$ , with  $\delta\Omega_M^{min}$  having negative sign. A new homodyne spectrum is acquired (blue peak in 3.34a) and comparison with the previous one enables to estimate  $\delta\Omega_M^{min}$ . Repeating this measurement for different values of the input optical power  $P_{in}$  and then fitting the experimental data to Eq. 3.78 allows to determine the value of the single-photon optomechanical coupling (Fig. 3.34c). Fig. 3.34d shows the detuning corresponding to the downshifted mechanical mode at different input powers and ensures these all correspond to the expected value  $\frac{\Delta_{min}}{k} = -\frac{\sqrt{3}}{6}$  within a standard deviation. These values were also used to derive the error bars in Fig. 3.34c. Data in Figs. 3.34 were recorded in the second version of our horizontal-cavity setup, featuring a high-finesse cavity and a topology-optimized trampoline (see Fig. 3.7c) and led to an estimate of  $g_0 = 2\pi \times (18.3 \pm 0.6)$  Hz.

### 3.5.2 Quantum noise thermometry

An alternative method to estimate the optomechanical coupling was first pioneered by Gorodetsky, Schliesser *et al.* in 2010 [35] and consists of a small thermometry experiment. The mechanical displacement brings about fluctuations of the cavity resonance frequency which are transcribed into the phase quadrature of the probing light. Homodyne detection allows to measure these fluctuations, as long as the subtraction photocurrent is calibrated into frequency units. This can be done by applying a phase-modulation at frequency  $\Omega_{cal}$  to the light interacting with the cavity, so that the input field  $E_{pr}$  takes the shape

$$E_{pr}(t) = E_0 e^{i\Omega_L t + i\beta \sin \Omega_{cal} t} \quad (3.80)$$

where  $\Omega_L$  and  $E_0$  are the laser frequency and amplitude.  $\beta$  is usually referred to as *modulation depth* and its knowledge is a necessary requirement to carry out our calibration. We will later explain how this parameter was measured for our EOM. The modulation interacts with our cavity and detector and is transformed into a modulation in the homodyne photocurrent according to the transduction function  $K(\Omega)$ . Integrating the PSD of the measured photocurrent  $S_{ii}$  around the calibration tone we can measure the variance of the transduced phase fluctuations  $\sigma_{cal}^2$ . Comparing this to the modulation depth, an estimate of the transduction function is obtained

$$K(\Omega_{cal}) = \frac{\sigma_{cal}^2}{\beta^2} = \frac{1}{\beta^2} \int_{\Omega_{cal}} S_{ii} \frac{d\Omega}{2\pi} \quad (3.81)$$

The transduction function does not vary appreciably over a small frequency range, thus for a calibration tone close to the mechanical mode of interest we can assume  $K(\Omega_{cal}) \approx K(\Omega_M)$ . We can then convert the variance of the phase fluctuations at the mechanical mode frequency  $\sigma_M^2 = \int_{\Omega_M} S_{ii} \frac{d\Omega}{2\pi}$  into terms of frequency fluctuations and obtain

$$\sigma_\omega^2 = \sigma_M^2 \frac{\Omega_M^2}{K(\Omega_M)} \quad (3.82)$$

The cavity frequency fluctuations induced by the mechanical motion have variance  $\langle \delta\Omega_c^2 \rangle = g_0^2 (2n_{th} + 1)$  and since they are imprinted into the phase of the probing light, Eq. 3.82 can be used to quantify them. Thus we obtain

$$\sigma_M^2 \frac{\Omega_M^2}{K(\Omega_M)} = g_0^2 (2n_{th} + 1) \quad (3.83)$$

where  $n_{th} = \frac{k_B T}{\hbar \Omega_M}$  is the number of thermal phonons populating our mechanical mode at temperature  $T$ . Please note that all our experiments are carried out at room temperature, hence  $T = 300$  K. The single-photon optomechanical coupling is then given by

$$g_0^2 = \frac{\Omega_M^2 \beta^2}{(2n_{th} + 1)} \frac{\sigma_M^2}{\sigma_{cal}^2} \quad (3.84)$$

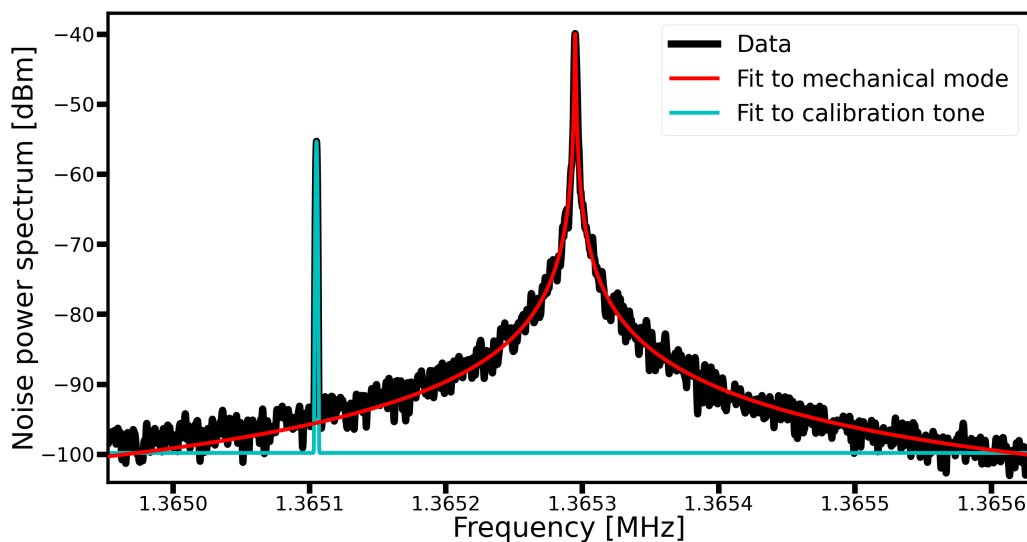


Figure 3.35: Fit to the experimental data from the quantum-noise thermometry measurement performed on a phononic membrane in a high-finesse cavity. Please note that while the mechanical mode was fitted to a Lorentzian function (red, on the right), a gaussian shape was used for the calibration tone (cyan, on the left).

This method was used to estimate the single-photon optomechanical coupling of a phononic membrane (Fig. 3.7b) in a high-finesse cavity and the results are shown in Fig. 3.35. Following the setup schematic shown in Fig. 3.32, an EOM applies phase modulation to the light traveling towards the cavity. The modulation frequency was chosen close to the mechanical mode of interest in order to avoid any relevant change in the transduction function. A spectrum containing both peaks was acquired through homodyne detection and the mechanical resonance was fitted to a Lorentzian curve, while the calibration tone was instead fitted to a Gaussian model [36]. Integrating the area under the two peaks and using Eq. 3.84, a single-photon optomechanical coupling of  $g_0 = 2\pi \times (10.1 \pm 0.8)$  Hz was estimated.

## 3.5.2.1 EOM modulation depth

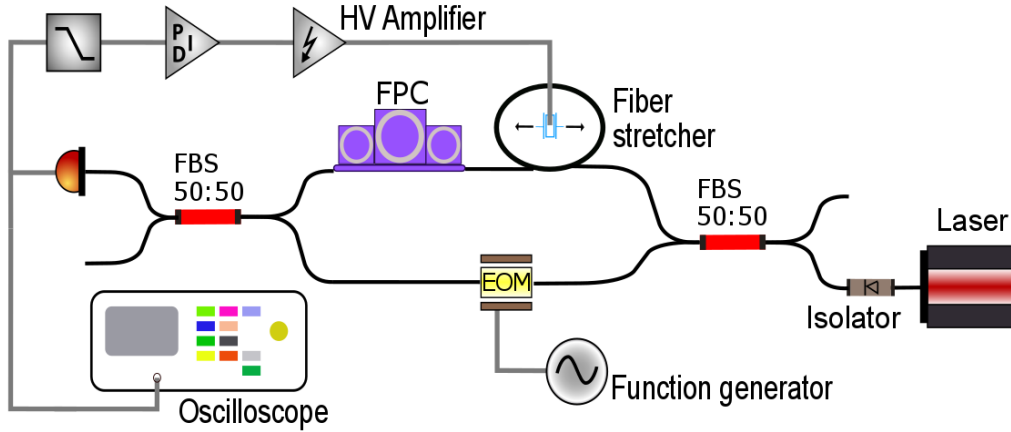


Figure 3.36: Setup used to calibrate the modulation depth of our EOM.

For the sake of completeness, here we will describe how the modulation depth of our EOM was characterized. Electro-optical modulators are typically based on the Pockels effect, that is to say they are made out of crystals whose birefringence can be controlled by an applied electric field  $E$ . The refraction index  $n(E)$  can be modeled as

$$n(E) = n - \frac{1}{2}rn^3E \quad (3.85)$$

where  $r$  is the Pockels coefficient. When an electromagnetic wave goes through the Pockels cell, it undergoes a phase change  $\Delta\phi$  depending on the voltage applied to the modulator

$$\Delta\phi \approx -\pi \frac{V_{in}}{V_{\pi}} \quad (3.86)$$

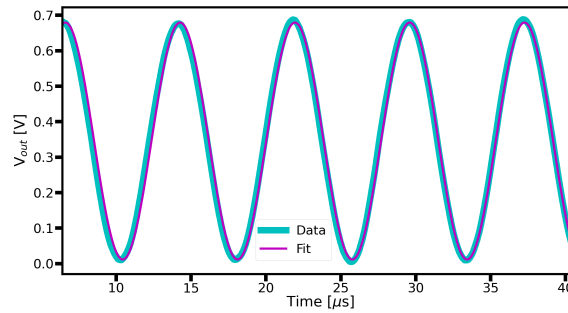
where  $V_{\pi}$  is the half-wave voltage, the voltage required to induce a phase shift of  $\pi$ . The maximum phase shift is then known as *modulation depth*

$$\beta = \Delta\phi_{max} \quad (3.87)$$

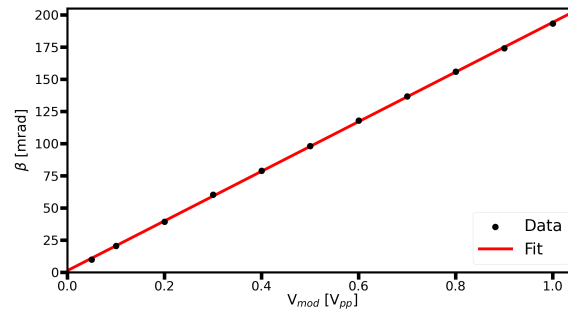
and it can be measured by a small interference experiment. Fig. 3.36 shows the setup we used to this goal, featuring a fiber-based Mach-Zehnder interferometer. Light is injected through a first 50/50 fiber beam splitter (FBS). Our EOM was placed in one of the arms and a fiber stretcher in the other. A fiber polarization controller (FPC) ensures the polarization of light in the two arms is matched, so that when the interference is maximum when the two optical signals recombine in a second 50/50 fiber beam splitter closing the interferometer. A Thorlabs PDA10CF-EC InGaAs detector is placed in one of the FBS outputs. The stroke of the fiber stretcher piezo is such that the relative phase between the two arms can be changed by several multiples of  $\pi$ . If the EOM is driven by a voltage modulation  $V_{mod}(t) = V_{mod} \sin(\omega_{mod}t)$  of amplitude  $V_{mod}$  and frequency  $\omega_{mod}$ , the interferometer transforms the phase modulation into amplitude modulation. The signal detected at the output of the interferometer is then

$$P_{out}(V_{in}) = \alpha \frac{P_{in}}{2} [1 + \cos(\phi_0 + \beta \sin \omega_{mod}t)] \quad (3.88)$$

where  $\alpha$  represents the insertion losses and  $P_{in}$  the input optical power.  $\phi_0 = n\Delta L \frac{\Omega L}{c}$  is the phase contribution related to the difference in path length  $\Delta L$  between the arms of the interferometer, with  $n$  being the refractive index of the fiber material [37]. In order to obtain the maximum amplitude of modulation at the output of the interferometer,  $\phi_0$  can be stabilized around  $\pi/2$  using a feedback circuit similar to the one used for homodyne detection (see Sec. 3.1.2.1). The DC signal from the detector is fed to a PID controller, whose output—after amplification—actuates a fiber stretcher. The locking point is found simply by turning off the EOM modulation, sending a ramp to the piezo and then selecting the voltage corresponding to half the maximum of the detected signal. The output of the interferometer displays then interference fringes that can be fitted to a sine function (Fig. 3.37a), allowing to estimate  $\beta$  for the specific modulation amplitude applied to the EOM. Varying this voltage, we can observe a linear dependence of the modulation depth on it (Fig. 3.37b).



(a)



(b)

Figure 3.37: a) Interference fringes obtained sending a  $V_{mod} = 1$  V modulation to the EOM. Fitting data to a sine function enables to estimate the modulation depth  $\beta$  for this specific modulation amplitude. b) Linear dependence between the modulation depth and the amplitude of the driving signal.



## 4 Optomechanical feedback cooling

We get now to the heart and soul of this thesis. This chapter will explain in detail what optomechanical feedback cooling is, how to run an experiment based on its protocol and what results can be obtained. In particular, our goal is to approach the motional ground state of macroscopic mechanical resonators—whose sizes range from millimeters to hundreds of micrometers—operating at room temperature, without using cryogenic equipment.

After an introduction to the theoretical framework and the working principles, the history of our experiment will be explained. Two versions will be presented. The first was designed by Jan Bilek, who carried out his PhD in our group [16]. I started out my work taking over from him, refining the performance of the setup he built and carrying out meaningful measurements that will here be discussed. Later, I designed and built my own setup, in order to achieve even better results. This second version of the experiment will be presented in the latter half of this chapter. The criteria I followed in planning what changes to make will be explained and the results I obtained will be reported.

### 4.1 Theory of feedback cooling

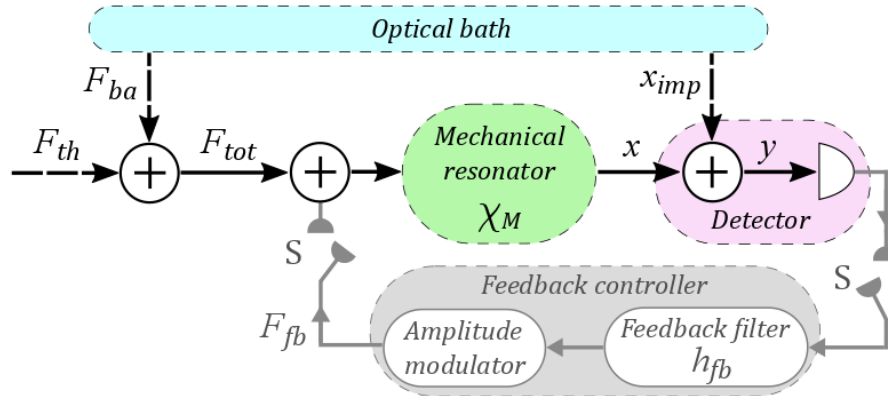


Figure 4.1: Scheme of the feedback cooling of a mechanical resonator. A beam of light monitors the displacement of a mechanical resonator in a continuous fashion. The readout signal is processed by a controller which actuates an additional feedback force acting on the mechanical resonator.

An optomechanical feedback cooling scheme is a two-sided protocol. On one hand, the position of a mechanical oscillator is continuously measured, while on the other a negative-derivative force damping is applied to its motion. The most usual approach consists of sensing the oscillator displacement by a *probe* light so that information about the amplitude of the mechanical motion is transcribed into the phase of the electromagnetic field. This information can then be accessed using a phase-sensitive detection scheme such as balanced homodyne detection and used to produce a *feedback force* which is engineered to minimize the mechanical displacement itself [38]. This force is typically proportional to the time derivative of the mechanical displacement, so its effect is that of a viscose damping acting on the oscillator. In the experiments presented here the feedback force is applied through a secondary beam of light named *cooling* beam. Other options have been explored in literature though, such as piezo-driven [39] or electrical actuators [40]. Furthermore, our scheme relies on the enhancement of the optomechanical interaction by an optical cavity. In our opinion this represents the most effective approach to boost the sensitivity of displacement

measurements. It prevents the readout signal from falling below the fundamental noise of the system by increasing the number of interactions between every photon and the mechanical oscillator [23]. Nevertheless, using a cavity is not strictly necessary for an optomechanical experiment and the possibilities of cavity-free feedback cooling have recently been explored [41].

Fig. 4.1 describes the dynamics of our optomechanical system. We first consider a simple case, without feedback loop. When the oscillator position is measured, the total force  $F_{tot}$  driving the mechanical motion consists of two contributions: a thermal force  $F_{th}$  and the quantum backaction force  $F_{ba}$ , stemming from the amplitude-quadrature fluctuations of the radiation pressure force. In frequency domain, the mechanical displacement  $x$  is then

$$(\Omega_M^2 - \Omega^2 - i\Omega\Gamma_M) x(\Omega) = m_{eff}^{-1} F_{tot}(\Omega) \quad (4.1)$$

where  $F_{tot}(\Omega) = F_{th}(\Omega) + F_{ba}(\Omega)$  and we define  $\chi_M = [m_{eff}(\Omega_M^2 - \Omega^2 - i\Omega\Gamma_M)]^{-1}$  as the mechanical susceptibility. Upon detection of the mechanical displacement, the optical shot noise brings about a phase contribution which sets the fundamental noise floor and can be modeled as an effective displacement imprecision noise  $x_{imp}$ . Although backaction and imprecision noise both originate from the light beam itself, they are uncorrelated in the case of a probe beam resonant with the cavity, that is to say for zero detuning. Taking the extra noise term into account, the measured mechanical displacement  $y$  will be

$$y(\Omega) = x(\Omega) + x_{imp}(\Omega) \quad (4.2)$$

When the switches S in Fig. 4.1 are closed, the measurement outcome is fed to a controller of transfer function  $h_{fb}(\Omega)$  which applies a feedback force  $F_{fb}(\Omega) = h_{fb}(\Omega) y(\Omega)$  to the mechanical oscillator through radiation pressure. The system dynamics is then modified into

$$x(\Omega) = \frac{\chi_M(\Omega)}{1 - \chi_M(\Omega) h_{fb}(\Omega)} [F_{tot}(\Omega) + h_{fb}(\Omega) x_{imp}(\Omega)] = \chi_{eff}(\Omega) [F_{tot}(\Omega) + F_{imp}(\Omega)] \quad (4.3)$$

$$y(\Omega) = \frac{\chi_M(\Omega) F_{tot}(\Omega) + x_{imp}(\Omega)}{1 - \chi_M(\Omega) h_{fb}(\Omega)} \quad (4.4)$$

$$\chi_{eff}(\Omega) = \frac{\chi_M(\Omega)}{1 - \chi_M(\Omega) h_{fb}(\Omega)} \quad (4.5)$$

The controller transforms the measurement imprecision noise  $x_{imp}(\Omega)$  into an additional force term  $F_{imp}(\Omega) = h_{fb}(\Omega) x_{imp}(\Omega)$ . On the other hand, the response of the oscillator to the driving force is affected by the controller, with the initial mechanical susceptibility changing into an effective one  $\chi_{eff}(\Omega)$ . The result is an effective mechanical damping rate

$$\Gamma_{eff} = \Gamma_M + \frac{\text{Im}[h_{fb}(\Omega_M)]}{m_{eff}\Omega_M} + \Gamma_{opt} \quad (4.6)$$

where the effect of dynamical backaction  $\Gamma_{opt}$  has been taken into account too. An appropriate choice of the transfer function  $h_{fb}(\Omega_M)$ , can then lead to the mechanical mode being damped and cooled. Based on Eq. 4.3, the symmetrized singled-sided noise spectrum of the actual displacement  $x$  is given by

$$\bar{S}_{xx}(\Omega) = |\chi_{eff}(\Omega)|^2 \left( \bar{S}_{FF}^{tot}(\Omega) + |h_{fb}(\Omega)|^2 \bar{S}_{xx}^{imp}(\Omega) \right) \quad (4.7)$$

while the outcome of a measurement of the mechanical displacement is described by

$$\bar{S}_{yy}(\Omega) = |\chi_{eff}(\Omega)|^2 \left( \bar{S}_{FF}^{tot}(\Omega) + |\chi_M(\Omega)|^{-2} \bar{S}_{xx}^{imp}(\Omega) \right) \quad (4.8)$$

We see that both these power spectral densities feature two contributions, one  $\bar{S}_{FF}^{tot}(\Omega)$  related to the sum of backaction and thermal force acting on the mechanical oscillator, the other  $\bar{S}_{xx}^{imp}(\Omega)$  coming from the imprecision noise of the measurement. In the jargon of feedback cooling experiments, the power spectral densities described by Eqs. 4.7 and 4.8 are referred to as *out-of-loop* and *in-loop* spectra, respectively. Under the hypothesis of validity of the equipartition theorem, the effective phonon occupancy of the mechanical mode of interest can then be estimated from from Eq. 4.7

$$\bar{n} = \frac{1}{2} \left( \frac{\langle \delta p^2 \rangle}{2p_{zpf}^2} + \frac{\langle \delta x^2 \rangle}{2x_{zpf}^2} - 1 \right) \approx \int_0^\infty \frac{\bar{S}_{xx}(\Omega)}{2x_{zpf}^2} \frac{d\Omega}{2\pi} - \frac{1}{2} \quad (4.9)$$

Our goal throughout this work is to engineer the parameters of our feedback cooling protocol so as to minimize the area under the out-of-loop spectrum  $\bar{S}_{xx}(\Omega)$ , hence the number of phonons  $\bar{n}$ . We will start at room temperature and attempt to get as close as possible to the regime where  $\bar{n} < 1$ , representing the motional ground state of our mechanical resonator. The amplitude of the typical feedback control transfer function is proportional to a tunable gain  $g_{fb}$ , whose value can be optimized in order to maximize the effect of optomechanical cooling. Increasing the gain above its optimal value drives the system into a regime where  $|h_{fb}(\Omega)| \gg |F_{imp}(\Omega)/x_{imp}(\Omega)|$  and the imprecision force heats the mechanical resonator. Such a behaviour usually manifests as a squashing of the noise floor below the shot-noise level in the in-loop spectrum  $\bar{S}_{yy}(\Omega)$ , induced by the appearance of correlations between the oscillator displacement  $x$  and the imprecision noise  $x_{imp}$  [38]. Please note that this effect does not appear in the out-of-loop spectrum  $\bar{S}_{xx}(\Omega)$ , whose area actually increases consistently with the rise in phonon number.

#### 4.1.0.1 Driving forces

At the mechanical-mode frequency, the power spectral densities  $\bar{S}_{xx}^{imp}$  and  $\bar{S}_{FF}^{tot}$  can be expressed in terms of multiples of quanta of the mechanical zero-point fluctuations, thus defining the corresponding imprecision-noise phonons  $n_{imp}$  and force-noise phonons  $n_{tot}$

$$\bar{S}_{xx}^{imp}(\Omega_M) = n_{imp} \frac{8x_{zpf}^2}{\Gamma_M} \quad (4.10)$$

$$\bar{S}_{FF}^{tot}(\Omega_M) = n_{tot} \frac{8p_{zpf}^2}{\Gamma_M} \quad (4.11)$$

For a resonant probe ( $\Delta = 0$ ) and in the bad cavity regime ( $k \gg \Omega_M$ ), the imprecision noise in balanced homodyne detection of the light coming out of an optomechanical cavity is given by

$$\bar{S}_{xx}^{imp}(\Omega_M) = \frac{x_{zpf}^2}{4\eta\Gamma_M C} \quad (4.12)$$

The imprecision phonon number can then be estimated by comparison with peak position spectral density in the ground state  $S_{xx}^{zp} = \frac{4x_{zpf}^2}{\Gamma_M}$

$$n_{imp} = \frac{\bar{S}_{xx}^{imp}(\Omega_M)}{S_{xx}^{zp}} = \frac{1}{16\eta C} = \frac{1}{16\eta(n_{th} + \frac{1}{2})C_q} \quad (4.13)$$

where we defined the quantum cooperativity  $C_q = C / (n_{th} + \frac{1}{2})$  related to the interaction between the optomechanical cavity and the probe beam. Please note how in the presence of losses  $\eta < 1$ , we have an increase of the imprecision noise.

The effect of the radiation-pressure amplitude noise is to increase the force acting on the mechanical resonator. When the feedback loop is closed, one more force term  $F_{fb}$  is added, so that  $F_{tot}(\Omega) = F_{th}(\Omega) + F_{ba}(\Omega) + F_{fb}(\Omega)$  and  $S_{FF}^{tot}(\Omega) = S_{FF}^{th}(\Omega) + S_{FF}^{ba}(\Omega) + S_{FF}^{fb}(\Omega)$ . At resonance with the mechanical mode, each term of the total-force power spectral density carries a contribution proportional to  $S_{xx}^{zp}$  through a phonon number

$$\bar{S}_{FF}^{tot}(\Omega_M) = \left(n_{th} + \frac{1}{2} + n_{ba} + n_{fb}\right) \frac{4p_{zpf}^2}{\Gamma_M} = n_{tot} \frac{4p_{zpf}^2}{\Gamma_M} \quad (4.14)$$

where  $n_{th} = \frac{1}{2} \coth \frac{\hbar\Omega_M}{2k_B T} \approx \frac{k_B T}{\hbar\Omega_M}$  and  $n_{ba} = |C|$ . We also have  $n_{fb} = |C^{cool}|$  where  $C^{cool}$  is the cooperativity related to the interaction between the optomechanical cavity and the cooling beam. A corresponding quantum cooperativity  $C_q^{cool} = C^{cool} / (n_{th} + \frac{1}{2})$  can be defined. We then obtain

$$n_{tot} = \frac{\bar{S}_{FF}^{tot}(\Omega_M)}{2S_{xx}^{zp}m_{eff}^2|\chi_M(\Omega_M)|^2} = n_{th} + \frac{1}{2} + C + C^{cool} = \left(n_{th} + \frac{1}{2}\right) \left(1 + C_q + C_q^{cool}\right) \quad (4.15)$$

## 4.2 Feedback controller

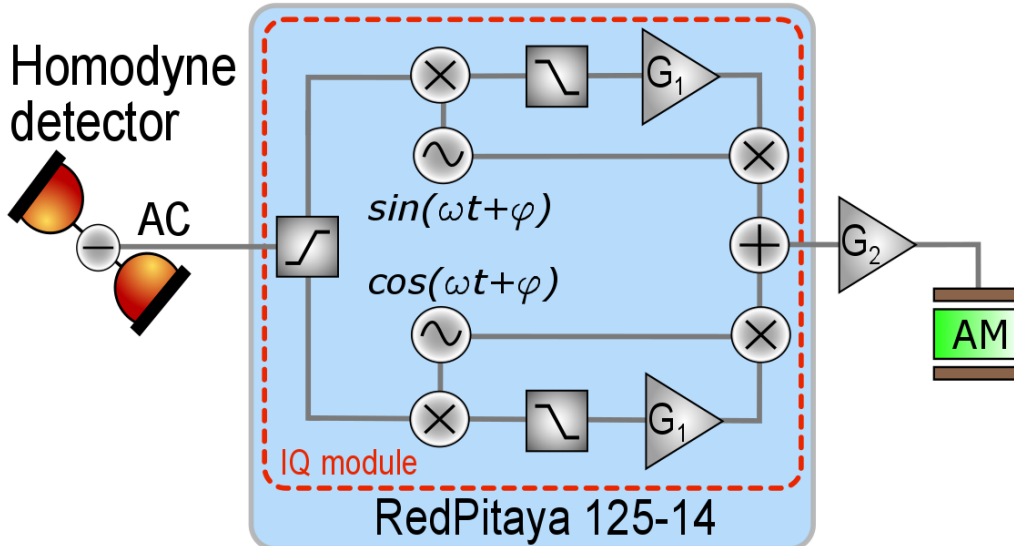


Figure 4.2: Schematic of our feedback controller. We detect the phase of the light emerging from the cavity by homodyne detection and the resulting photocurrent is fed to a RedPitaya 125-14. This hosts the PyRPL IQ software module that works as a digital bandpass filter with variable gain  $G_1$ . Its output goes through a low-noise amplifier of fixed gain  $G_2$  before providing an RF signal to our amplitude modulator (AM).

In feedback cooling, a fundamental role is played by the controller applying the feedback force. In our experimental scheme, this function is performed by a digital filter which receives the homodyne-detection AC photocurrent and produces the error function for the amplitude modulation of a secondary beam of light (*cooling beam*) interacting with the optomechanical cavity (see Fig. 4.2). The filter output is first amplified, then it drives an electro-optical amplitude modulator MXAN-LN-10 from iXblue Photonics, whose operational bandwidth ( $\approx 10$  GHz) is much broader than the mechanical frequencies we work with ( $< 1.5$  MHz). Considering that also the bandwidths of our detectors and amplifiers are in the order of tens of MHz, the controller operation is mainly defined by the digital filter. We chose a bandpass Lorentzian filter and implemented it using a PyRPL IQ software module hosted by a FPGA RedPitaya 125-14. This solution offers a wide tunability in terms of central frequency, bandwidth and gain. The transfer function of such a filter is described by 4.1

$$h_{fb}(\Omega) = g_{fb} e^{i\Omega\tau - i\Phi} \left[ \frac{\Gamma_{fb}\Omega}{\Omega_{fb}^2 - \Omega^2 - i\Gamma_{fb}\Omega} \right]^2 \quad (4.16)$$

where  $\Omega_{fb}$  and  $\Gamma_{fb}$  represent the filter central frequency and linewidth. The gain  $g_{fb}$  is measured in units of  $\text{kg Hz}^2$  as it represents not only the electronic gain provided by the FPGA and the amplifier but also all the factors related to the transduction of amplitude modulation into force.  $\tau$  is the delay time representing the sum of the propagation time through electronic components and the computation time of the digital filter. The overall phase  $\Phi$  is adjusted experimentally through a digital phase delay in the IQ module in order to get  $\arg[h_{fb}(\Omega_M)] \approx \frac{\pi}{2}$ . Under such condition the effect of the applied force at  $\Omega_M$  can be described as a viscous damping while any deviation from it will bring about a change in spring constant that corresponds to a shift in mechanical resonance frequency. When performing feedback cooling, we usually start by setting  $\Omega_{fb} \approx \Omega_M$  and the digital gain  $G_1$  to a value such that its product with the fixed amplifier gain  $G_2$  is  $G_1 G_2 \ll 1$ . The phase is then optimized and afterwards the filter bandwidth is adjusted by tuning the cutoff frequency of the low-pass filters in the IQ module in order to maximize the induced mechanical broadening. The resulting linewidth  $\Gamma_{fb}$  can be quantified by a separate measurement of the filter transfer function, together with the delay time. As an example, we report the amplitude and phase of the transfer function of the digital filter used to feedback cool the fundamental mode of a trampoline at 132 kHz (Figs. 4.3). In this case, we measured  $\Gamma_{fb} = 9.72$  kHz and  $\tau = 380$  ns. Once the filter phase and bandwidth have been optimized, increasing the gain cools the targeted mechanical mode reducing its phonon occupation.

### 4.3 Calibration of mechanical spectra

Before presenting our experimental results, it will be necessary to explain how to calibrate the photocurrent spectra recorded using our spectrum analyzer into units of mechanical displacement [23]. We begin by normalizing the measured open-feedback-loop photocurrent power spectral density  $\bar{S}_{ii}(\Omega)$  so that the shot noise  $\bar{S}_{ii}^{SN}(\Omega)$  equals 1/2

$$\bar{S}_{ii}^{norm}(\Omega) = \frac{\bar{S}_{ii}(\Omega) - \bar{S}_{ii}^{DN}(\Omega)}{2[\bar{S}_{ii}^{SN}(\Omega) - \bar{S}_{ii}^{DN}(\Omega)]} \quad (4.17)$$

where  $\bar{S}_{ii}^{DN}(\Omega)$  represents the detector dark noise. Focusing on the PSD value at mechanical resonance, we can use Eq. 4.17 as a measure of the *SNR*

$$SNR = 2\bar{S}_{ii}^{norm}(\Omega_M) - 1 \quad (4.18)$$

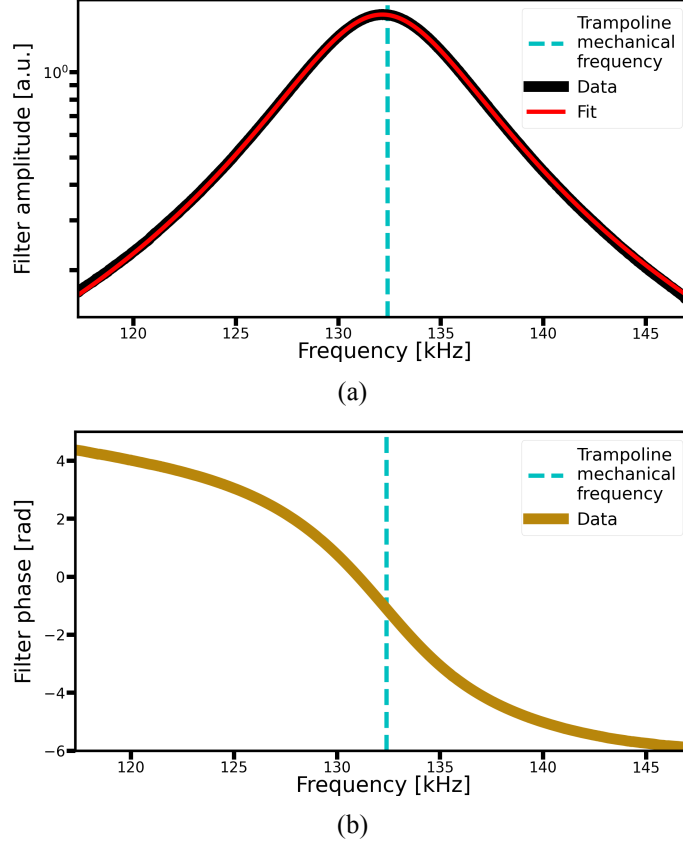


Figure 4.3: a) Amplitude and b) phase of the transfer function of the digital filter used to feedback-cool the fundamental mode of a trampoline at  $\Omega_M = 2\pi \times 132$  kHz. The red curve in Fig. a) was obtained fitting the experimental data to Eq. 4.16. A network analyser Agilent E5061B was used for this characterization. The vertical dashed line indicates the frequency of the fundamental mode of a trampoline.

Please note that here we defined the  $SNR$  as the ratio between the normalized-signal peak value minus the normalized noise floor—given by the shot noise—and the normalized shot noise. On the other hand, for a probe resonant with the cavity, at the mechanical peak frequency the normalized homodyne detection spectrum of mechanical displacement is given by

$$\bar{S}_{ii}^{norm}(\Omega_M) = \frac{1}{2} + 8\eta |C_{eff}(\Omega_M)| \left( n_{th} + \frac{1}{2} + |C_{eff}(\Omega_M)| \right) \quad (4.19)$$

where  $|C_{eff}(\Omega_M)| = \frac{C}{1+(2\Omega_M/k)^2}$ . We then have

$$SNR = 16\eta |C_{eff}(\Omega_M)| \left( n_{th} + \frac{1}{2} + |C_{eff}(\Omega_M)| \right) \quad (4.20)$$

With a bit of algebra we obtain

$$|C_{eff}(\Omega_M)| = \frac{1}{2} \left( n_{th} + \frac{1}{2} \right) \left[ -1 + \sqrt{1 - \frac{SNR}{4\eta \left( n_{th} + \frac{1}{2} \right)^2}} \right] \quad (4.21)$$

We first use Eqs. 4.21 and 4.12 to estimate the imprecision noise of our measurement, which corresponds to the calibrated shot noise. Then using the same normalization we defined at the beginning, we can calibrate our mechanical spectrum into units of displacements simply by

$$\bar{S}_{yy}(\Omega) = 2\bar{S}_{ii}^{norm}(\Omega) \bar{S}_{xx}^{imp}(\Omega) \quad (4.22)$$

## 4.4 Optomechanical feedback cooling I

The first experimental setup I worked on during my PhD was built by my predecessor Jan Bilek and it was based on a trampoline oscillator located within the vertical-cavity optomechanical assembly described in Sec. 3.3.6.1. After a description of both the optical setup and the mechanical resonator, experimental results will be presented.

### 4.4.1 Experimental setup

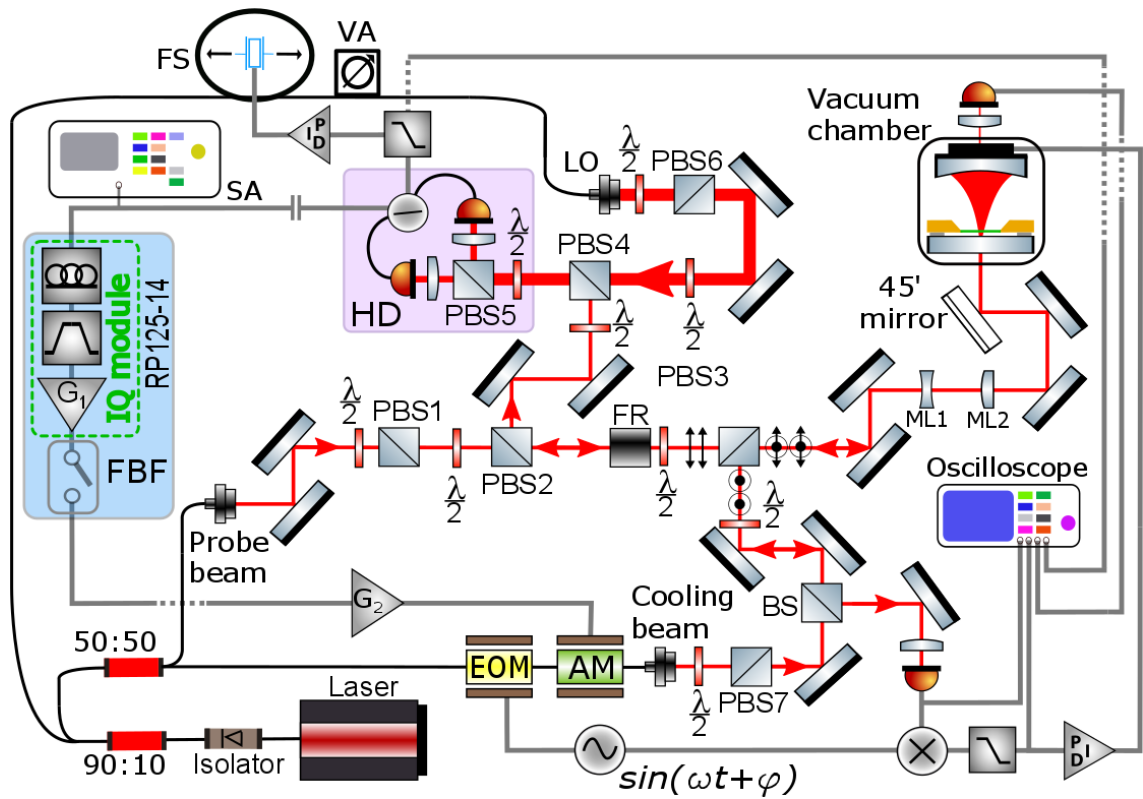


Figure 4.4: The experimental setup employed for feedback-cooling of a trampoline. Acronyms: electro-optic modulator (EOM), amplitude modulator (AM), half-wave plate ( $\frac{\lambda}{2}$ ), polarization beam splitter (PBS), Faraday Rotator (FR), beam splitter (BS), mode-matching lens (ML), local oscillator (LO), homodyne detection (HD), spectrum analyser (SA), feedback filter (FBF), RedPi-taya 125-14 (RP125-14), fiber stretcher (FB), variable attenuator (VA).

Fig. 4.4 shows the experimental setup employed for feedback cooling of a trampoline. A fiber-coupled laser NKT Koheras BASIK E15 emits light at a wavelength around 1550 nm which then propagates through an isolator before being split with a ratio of 90:10 by a fiber beam splitter. The weaker light beam goes through a second fiber beam splitter and is divided in two halves of equal power. One of them is directly outcoupled in free space and provides our probing beam. This crosses a half-wave plate ( $\lambda/2$ ) and PBS (PBS1) which are used to tune its power. It then goes through several other optical components and reaches the plane mirror of our hemispherical cavity, whose axis is oriented perpendicular to the optical table. Right before the cavity, two lenses (ML1

and ML2) are placed to match its profile to the intracavity field, followed by two mirrors on tip-tilt mounts. These steer the light in the plane of the optical table before a mirror mounted at a fixed angle of  $45^\circ$  redirects it onto the direction perpendicular to the table. Inside the cavity, our mechanical resonator sits on top of the incoupling mirror, from which it is separated by a small silicon spacer. Due to the need to minimize the gas damping of the mechanical motion, the optomechanical assembly is located inside a vacuum chamber operated at a pressure around  $10^{-7}$  mbar. The chamber windows are standard Thorlabs VPCH42-C, AR-coated for light at wavelength around 1550 nm. A large-area photodiode Thorlabs PDA50B2 is placed above the cavity curved mirror for alignment purposes. This can be replaced by a CCD camera in order to image the mechanical resonator and tune the relative position of the cavity axis. Light reflected from the cavity travels back through PBS3 and a Faraday Rotator (FR) which rotates its polarization by  $90^\circ$ , so that the beam is reflected off PBS2 and steered into our homodyne detection setup. Here it is spatially overlapped with the local oscillator (LO) on PBS4. A half-wave plate rotates both their polarizations by  $45^\circ$ , so that PBS5 splits the total optical power in equal halves, which are then focused on the two photodiodes of our homodyne detector (HD). The final waveplate is also used to compensate for small electronic offsets in the two detection channels, so that the DC part of the subtraction photocurrent perfectly equals the electronic zero of the detector. The local oscillator is provided from the 90% optical power emerging from the 90:10 fiber beam splitter. This propagates through a fiber stretcher (FS) and a fiber variable attenuator (VA) before being outcoupled in free space, where a halfwave plate and PBS6 fine-tune its power. Please note that since the local oscillator is transmitted through PBS4 while the probe is reflected off it, the two beams have orthogonal polarization and do not interfere before the final waveplate applies a  $45^\circ$  rotation. One more waveplate is placed in the path of each beam to make sure its polarization matches the axis of PBS4 and minimize the optical losses. The missing half of the optical power emerging from the 50:50 fiber beam splitter propagates through fiber modulators of phase (EOM) and amplitude (AM) before being outcoupled into free space and producing our cooling beam. This goes through a half-wave plate and PBS7 where its power is adjusted, then a beam splitter, a waveplate rotating its polarization by  $90^\circ$  and finally it is spatially overlapped to the probe beam on PBS3. Please note that their electric fields have orthogonal polarization, as one is transmitted through and other reflected off PBS3. The respective polarization directions are indicated by perpendicular arrows in Fig. 4.4. As a consequence, although the cooling beam overlaps with the probe while propagating towards the cavity, there is no interference between the two fields. Furthermore, the orthogonal polarization allows them to be separated again by PBS3 after being reflected back, with the cooling beam being steered towards its outcoupler. A beam splitter then taps off half of its power and steers it towards a Thorlabs photodiode APD430C/M. This is used in combination with the EOM, the dual-channel function generator, the multiplexer, a low-pass filter and an analog PID controller to produce a Pound–Drever–Hall (PDH) scheme and lock the cavity frequency to the laser through actuation of the piezo element holding the cavity curved mirror. Details on this scheme have been provided in Sec. 3.3.8.2. The amplitude of the cooling beam is modulated by the feedback controller. More in detail, the AC homodyne photocurrent is monitored by a spectrum analyser Keysight N9000B CXA (SA) and fed to the RedPitaya (RP125-14) hosting the feedback filter (FBF) and a switch. The filter functions as a delay line followed by a band-pass filter and an amplifier of tunable gain  $G_1$ . A fixed gain  $G_2$  is applied by an external amplifier whose output provides the RF signal to the amplitude modulator. The DC component of the homodyne photocurrent provides the error function for an analog PID controller that actuates the fiber stretcher and locks the phase difference between probe and local oscillator to  $\pi/2$  allowing detection of pure phase quadrature.

### 4.4.2 Trampoline

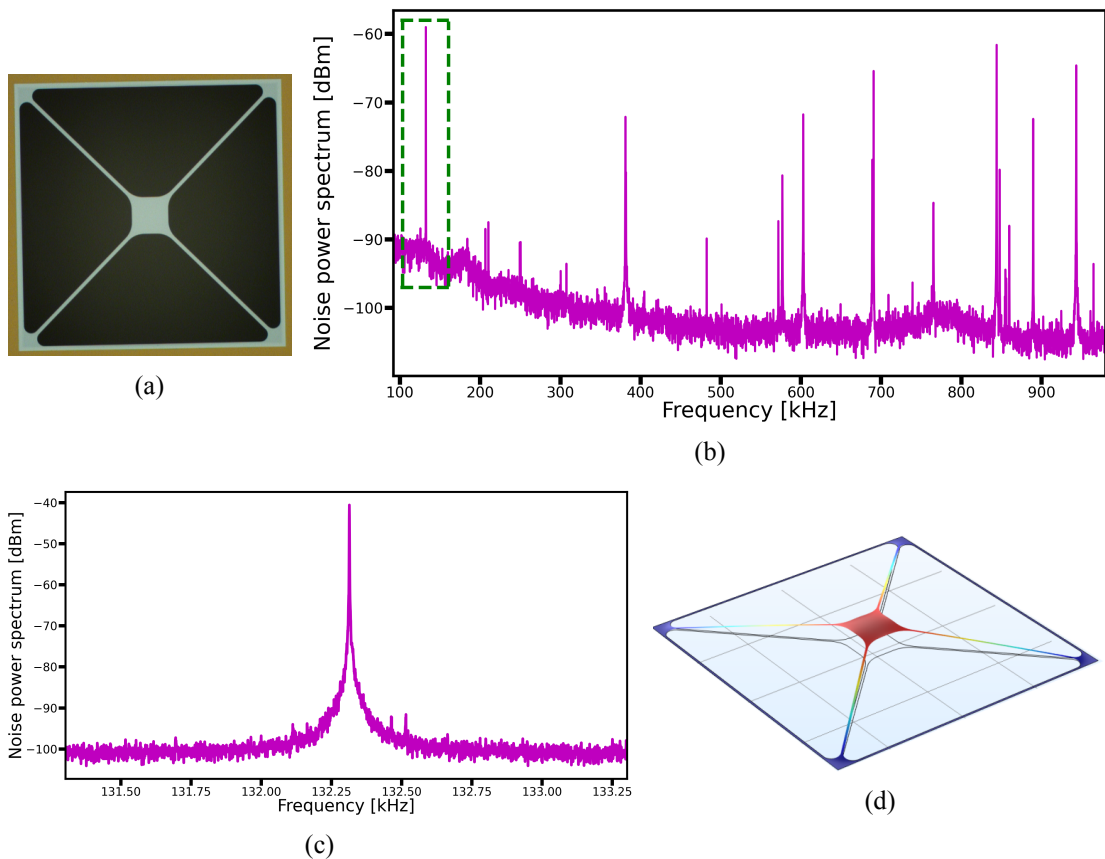


Figure 4.5: a) Microscope image of our tethered membrane (*trampoline*). b) Power spectral density of the Brownian noise of our trampoline, showing discrete modes at a spacing comparable to the frequency of the fundamental mode. The green square singles out the fundamental mode, which is then displayed in Fig. c). d) Simulation of the out-of-plane displacement of the trampoline central pad occurring at the fundamental-mode frequency.

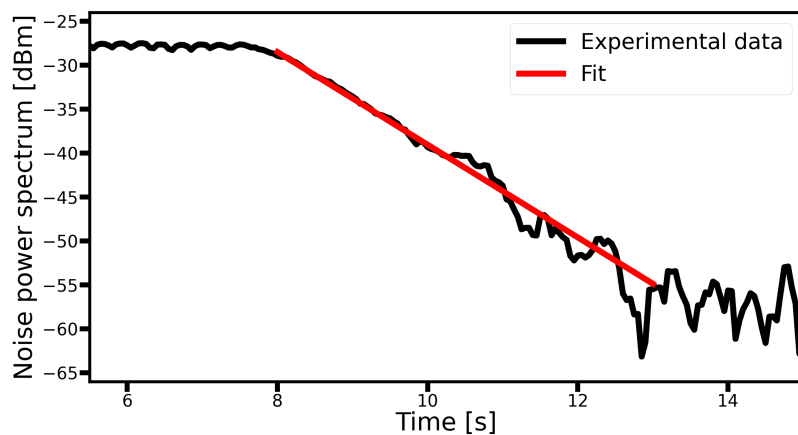


Figure 4.6: Results from the mechanical-ringdown measurement for the trampoline fundamental mode at 132 kHz. A quality factor of  $Q = 0.7 \times 10^6$  was measured.

The mechanical resonator used in this version of the experiment is a stressed silicon-nitride membrane located at the center of a  $1 \text{ mm} \times 1 \text{ mm}$  square window etched through a silicon chip. The membrane is composed of a  $150 \text{ }\mu\text{m} \times 150 \text{ }\mu\text{m}$  central pad connected to the window frame by  $5 \text{ }\mu\text{m}$ -wide tethers and is depicted in Fig. 4.5a. This design was adapted from the work of Gröblacher’s group at TUDelft [42], tailoring its parameters to our experiment. The resulting structures are usually referred to as *trampolines* and exhibit a Brownian-noise power spectral density featuring discrete modes whose frequency spacing is comparable with their fundamental vibrational frequency, as we show in Fig. 4.5b. In our mechanical resonator, the thickness of  $50 \text{ nm}$  brings about an effective mass of  $3.56 \text{ ng}$ —inferred from a COMSOL finite element simulation—and a fundamental vibrational frequency  $\Omega_M/2\pi \cong 132 \text{ kHz}$  (4.5c). The low thickness of the membrane and the ultra-high stress of the silicon-nitride layer provide a low energy dissipation rate for the phonons of the fundamental mode. Using the ringdown technique described in Sec. 3.4, the corresponding mechanical quality factor was measured to be  $Q = 0.7 \times 10^6$ . The measurement data are displayed in Fig. 4.6.

#### 4.4.3 Experimental parameters

Experimental parameters		
Laser wavelength		1550 nm
Cavity FSR		146.96 GHz
Cavity linewidth	$k$	$2\pi \times 15.19 \text{ MHz}$
Cavity finesse	$\mathcal{F}$	9675
Escape efficiency	$\eta_{esc}$	0.7
Efficiency of optical components	$\eta_{opt}$	0.68
Homodyne visibility	$\nu$	0.80
Quantum efficiency of homodyne detection	$\eta_{QE}$	0.76
Total homodyne-detection efficiency	$\eta_D = \eta_{opt}\nu^2\eta_{QE}$	0.33
Total efficiency	$\eta = \eta_D\eta_{esc}$	0.31
Mechanical oscillator frequency	$\Omega_M$	$2\pi \times 132 \text{ kHz}$
Mechanical quality factor	$Q$	$0.7 \times 10^6$
Mechanical linewidth	$\Gamma_M$	0.189 Hz
Effective mass	$m_{eff}$	3.56 ng
Mechanical zero-point displacement amplitude	$x_{zpf}$	4.2 fm
Single-photon optomechanical coupling	$g_0$	$2\pi \times 3.3 \text{ Hz}$
Feedback filter linewidth	$\Gamma_{fb}$	$2\pi \times 9.72 \text{ kHz}$
Feedback filter delay	$\tau$	380 ns
Mechanical bath temperature	$T$	300 K
Thermal phonon occupancy number	$n_{th} = k_B T / \hbar \Omega_M$	$\approx 4.7 \times 10^7$

Table 4.1: Specifications of the optomechanical setup used for feedback cooling of a trampoline.

Table 4.1 reports the main specifications of the experimental setup used for feedback cooling of our trampoline’s fundamental mechanical mode. At the laser wavelength of  $\approx 1550 \text{ nm}$ , the short cavity size of  $\approx 1 \text{ mm}$  corresponds to an FSR of  $2\pi \times 146.96 \text{ GHz}$ . The low transmission of the mirrors (namely 200 ppm and 10 ppm for the plane and curved mirror respectively) brings about a high finesse. Having found an optical linewidth of  $2\pi \times 15.19 \text{ MHz}$  for our cavity, the finesse is estimated to be around 9675. Please note the high ratio between cavity linewidth and mechanical frequency  $\Omega_M = 2\pi \times 132 \text{ kHz}$  places our system deep into the unresolved sideband (bad cavity) regime, where  $k \gg \Omega_M$ . The high asymmetry between the two mirrors’ reflectivities yields an escape efficiency  $\eta_{esc} = 0.7$ .

The total homodyne-detection efficiency is  $\eta_D = 0.33$  and it is mainly limited by three factors. First off, the light reflected from our cavity needs to go through many optical components, whose intrinsic properties result in an optical efficiency  $\eta_{opt} = 0.68$ . Most of this power loss is supposed to come from the Faraday Rotator, PBS3 and the vacuum chamber windows, whose transmissions are respectively 0.92, 0.95 and 0.94. Reflection of both PBS2 and PBS4 is around 0.99. The homodyne visibility  $\nu = 0.80$  stems from a suboptimal mode-matching of the probe to the local oscillator. The long distance between the mode-matching lenses and the incoupling mirror of the cavity ( $\approx 35$  cm) combined with the out-of-plane geometry of our setup brings about spherical aberrations of the beam profile of the back-reflected light which limit the mode-matching to the local oscillator, hence the visibility. Finally, the photodiodes used for homodyne detection are standard Thorlabs FDGA05, whose quantum efficiency is  $\eta_{QE} = 0.76$ . This means almost one fourth of the impinging optical power is not detected. The total efficiency of the measurement is then  $\eta = \eta_D \eta_{esc} = 0.23$ .

The single-photon optomechanical coupling was measured using the spring effect as explained in Sec. 3.5.1, obtaining a value of  $g_0 = 2\pi \times (3.3 \pm 0.2)$  Hz. The measurement results are shown in Fig. 4.7.

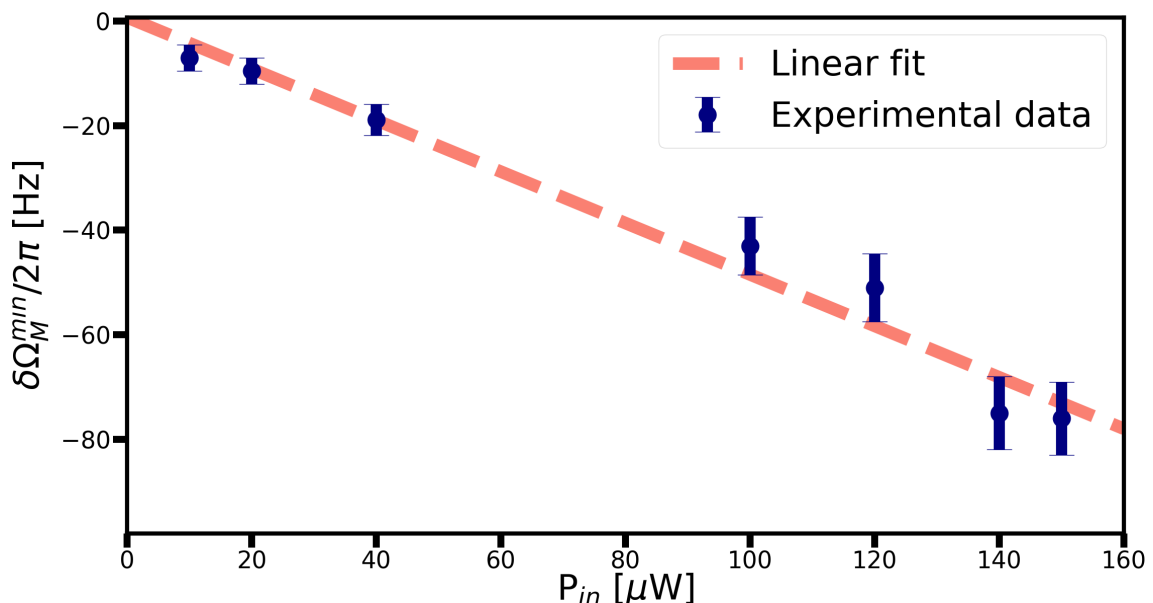


Figure 4.7: Determination of the single-photon optomechanical coupling through spring effect. For our vertical cavity containing a trampoline, a value of  $g_0 = 2\pi \times (3.3 \pm 0.2)$  Hz was found.

#### 4.4.4 Results

We can finally present our first feedback cooling results. The spectra presented in Figs. 4.8a-b were acquired using our spectrum analyser, whose resolution and video bandwidth were both fixed to 1 Hz. Every spectrum represents an average over 30 consecutive traces acquired under the same experimental conditions. All these measurements were performed while locking the cavity on resonance with our laser ( $\Delta = 0$ ) and the homodyne quadrature angle to  $\pi/2$  in order to detect pure phase quadrature. A power of  $P_{LO} = 3$  mW was chosen for the local oscillator. Leaving the feedback-controller switch open, a noise spectrum of the mechanical mode is first acquired at room temperature, where the phonon occupancy number is  $n_{th} = k_B T / \hbar \Omega_M \approx 4.7 \times 10^7$ . The switch is then closed and the filter gain  $G_1$  of the RedPitaya IQ module is set to such a value that the overall electronic gain is  $G_1 G_2 \ll 1$ . Phase and bandwidth of the feedback filter are thus adjusted to maximize the mechanical-mode broadening and minimize the mechanical-shift given by deviations from the condition  $\arg[h_{fb}(\Omega_M)] = \pi/2$ . Afterwards, the electronic gain

is increased by discrete steps and the effect is observed monitoring the mechanical mode on the spectrum analyser. Fig. 4.8a shows the in-loop mechanical-displacement noise spectrum measured for different gain values and an input optical power of  $P_{in}^p = 1 \mu\text{W}$  and  $P_{in}^c = 100 \mu\text{W}$  for the probe and cooling beam, respectively. Please note the shot noise appears as a flat line because all spectra were normalized to it before calibration as explained in Sec. 4.3. The inset shows the uncalibrated data. As we can see, our measurements are not shot-noise limited. Therefore, the calibrated power spectral density cannot be fitted to Eq. 4.8, which considers the shot noise as the sole source of non-resonant noise. We find a simple way around this problem by introducing a ratio  $r_{nf}(\Omega)$  between the measurement noise floor and the shot noise. Eq. 4.8 is then modified into

$$\bar{S}_{yy}(\Omega) = |\chi_{eff}(\Omega)|^2 \left( \bar{S}_{FF}^{tot}(\Omega) + r_{nf}(\Omega) |\chi_M(\Omega)|^{-2} \bar{S}_{xx}^{imp}(\Omega) \right) \quad (4.23)$$

Recalling Eqs. 4.13 and 4.15, the in-loop spectra were then fitted to Eq. 4.23 using  $n_{imp}$  and  $n_{tot}$  as fitting parameters, as well as the filter gain  $g_{fb}$  and phase  $\Phi$  defined in Eq. 4.16. The results can be used to infer the actual mechanical-displacement spectrum  $\bar{S}_{xx}(\Omega)$  described by Eq. 4.7. Fig. 4.8b shows a comparison between the measured in-loop spectrum  $\bar{S}_{yy}(\Omega)$  (solid lines), curves obtained fitting to Eq. 4.23 (dashed lines) and the inferred out-of-loop spectra  $\bar{S}_{xx}(\Omega)$  (dashed-dotted lines). For an electronic gain of 100, we observe the in-loop noise floor squashing below the shot noise level. This happens when the filter gain exceeds its optimal value and imprecision noise is fed back to the mechanics [43]. Please note that this noise reduction at the mechanical frequency only pertains to the measured power spectral density  $\bar{S}_{yy}(\Omega)$ , while the actual mechanical-displacement spectrum  $\bar{S}_{xx}(\Omega)$  still appears as a broad Lorentzian (brown dash-dotted line in the plot). Integrating the area under the out-of-loop power spectral density allows to determine the phonon occupancy  $\bar{n}$  of our mechanical mode of frequency  $\Omega_M$  (see Eq. 4.9). Fig. 4.9 displays the results in the form of a  $\bar{n}$  vs  $\Gamma_{eff}$  graph. Error bars are not showed as their size is smaller than the markers representing data. The lowest phonon occupancy  $\bar{n}^{min} = 39300 \pm 800$  was achieved for an electronic gain of 50 and an effective mechanical linewidth of  $2\pi \times 360$  Hz (purple octagon in the plot). Such phonon number represents the minimum value achieved in this version of the feedback cooling experiment. Increasing the gain above this value leads to the imprecision force heating up the mechanics and to the squashing phenomenon described above, hence to an increase in phonon occupancy (orange octagon in the plot). Our results are compared with a theoretical prediction computed using the  $n_{imp}$  and  $n_{tot}$  values estimated for zero gain and assuming  $\arg[h_{fb}(\Omega_M)] = \pi/2$ . This is displayed as a solid grey line in Fig. 4.9 and its minimum phonon occupancy  $\bar{n}_{th}^{min} = 38789$  lies within a standard deviation from the minimum value we find experimentally.

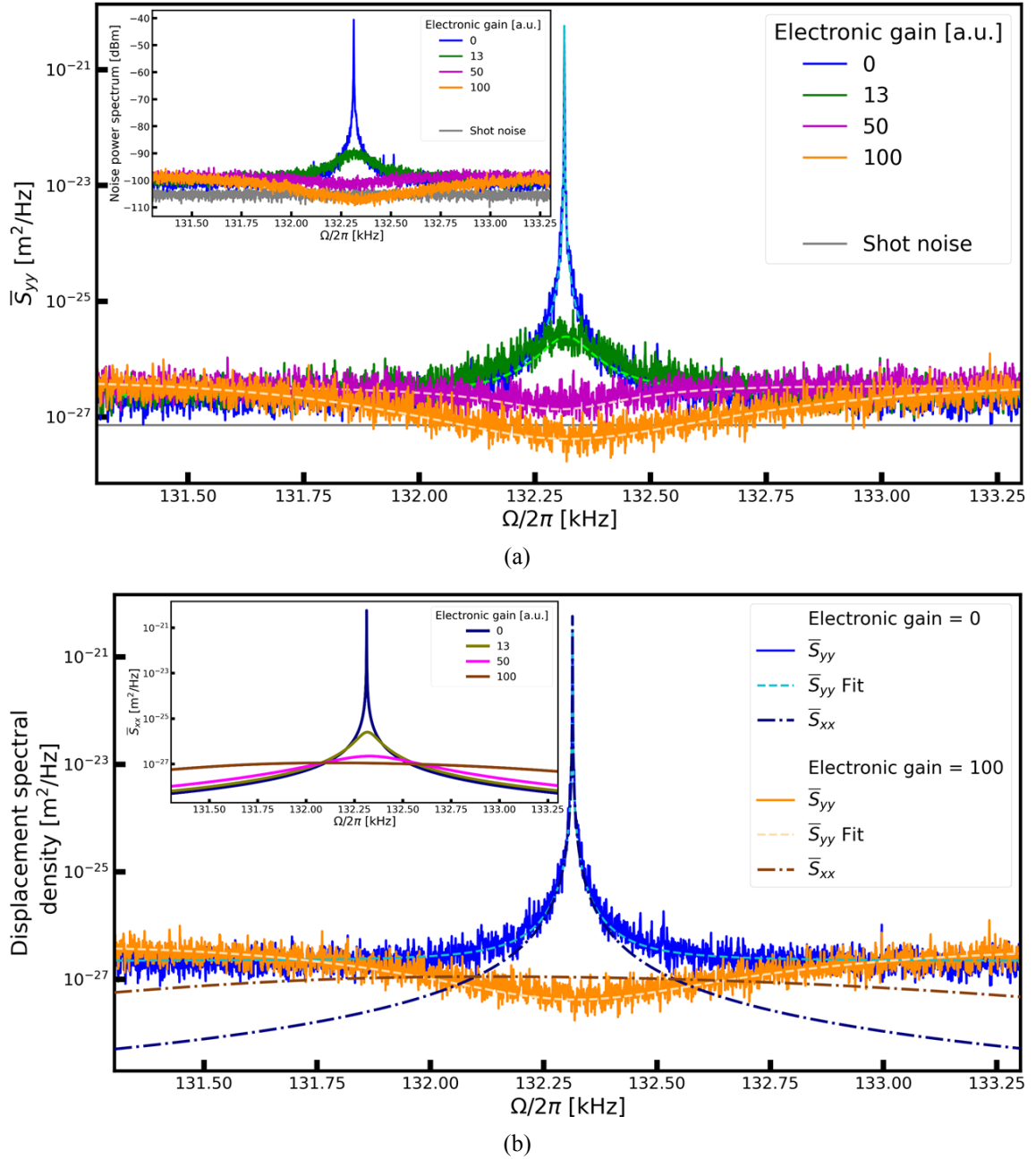


Figure 4.8: Feedback cooling. a) Spectra of the in-loop mechanical-displacement noise acquired for different electronic gains. The dashed lines are obtained fitting the data to Eq. 4.23. The shot noise (grey) appears as a flat line because in our calibration method all spectra are normalized to it. Inset shows the corresponding uncalibrated power spectral densities. b) Comparison between measured in-loop noise spectrum  $\bar{S}_{yy}(\Omega)$  (solid lines), fit to Eq. 4.23 (dashed lines) and the inferred out-of-loop displacement spectral density  $\bar{S}_{xx}(\Omega)$  (dashed-dotted lines) for two values of the electronic gain. Inset shows the inferred out-of-loop spectra obtained from the data in Fig. a.

#### 4.4.5 Conclusions: how to move forward

The results presented above are encouraging. The phonon occupancy number of our mechanical mode at frequency  $\Omega_M/2\pi = 132$  kHz was decreased from its room-temperature value around  $4.7 \times 10^7$  down to  $\bar{n}^{min} = 39300$ . Although we are still far from the ground state ( $\bar{n}_{gs} < 1$ ), this represents approximately a fourfold improvement with respect to the lowest occupancy number

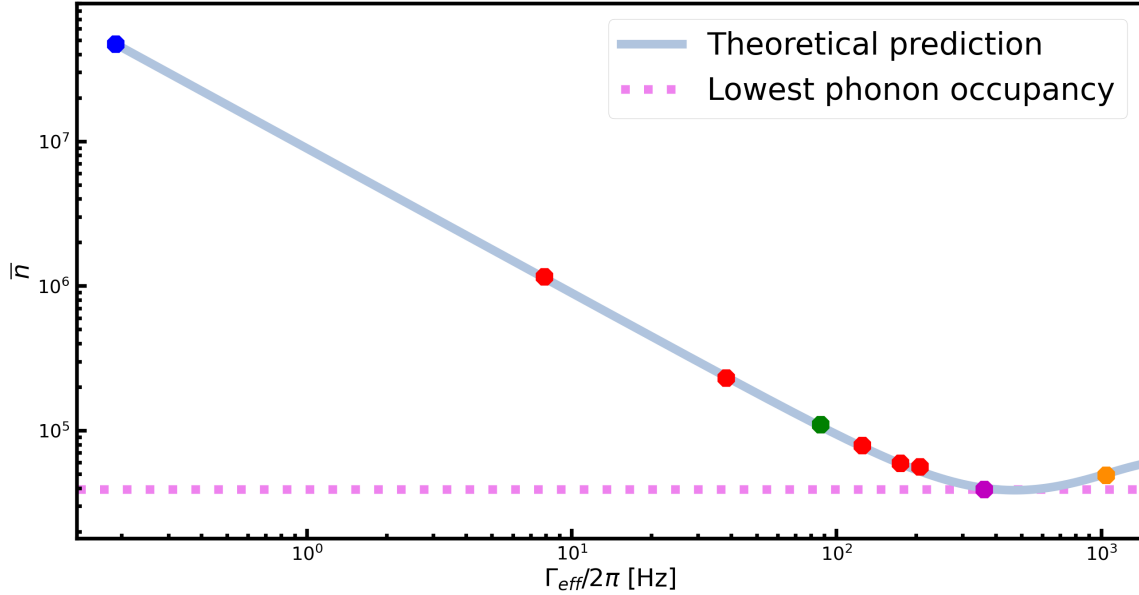


Figure 4.9: Phonon number occupancy  $\bar{n}$  as a function of the effective mechanical linewidth  $\Gamma_{eff}$ . Blue, green, purple and orange octagons represent the values extracted from the spectra in Figs. 4.8a-b. The red markers describe the values computed for other spectra from the same dataset. The dotted pink line marks the lowest measured phonon occupancy  $\bar{n}^{min} = 39300 \pm 800$ , represented by the purple octagon. For higher gain, the phonon number increases again (orange octagon) due to the imprecision noise correlating with the mechanics. Results are compared with a theoretical prediction (grey line) obtained using the  $n_{imp}$  and  $n_{tot}$  values estimated for zero gain and assuming  $\arg[h_{fb}(\Omega_M)] = \pi/2$ .

reported by Jan Bilek [16], who initiated our experiment on feedback-cooling of a trampoline and harvested the first data during his time at QPIT. I started out my PhD taking over his experimental setup and working to enhance its performances. It is relevant to discuss what changes I made, as such considerations draw the roadmap I followed in designing my own version of the feedback cooling experiment, whose results are presented in Sec. 4.5

In Jan's experiment the same light beam was used to both sense the mechanical motion and apply the feedback force. Half of the optical power reflected off the cavity was steered towards the homodyne detector. The rest was used to produce the PDH error function and lock the cavity frequency to the incoming laser. Such a scheme is very inconvenient, as small fluctuations of the homodyne phase-lock result in detection of the intense amplitude modulation resonant with the mechanical mode. Besides, tapping off half of the light for PDH locking results in massive optical losses, detrimental to the efficiency of our feedback-cooling protocol. Both these problems are solved using different beams to probe the mechanical motion and apply the feedback force. Direct detection of the reflected cooling beam is then used to produce the PDH error function, avoiding the increase of losses along the probe path. The two beams come from the same laser and feature orthogonal polarizations, allowing their reflection to be separated by a PBS. However, due to the imperfect extinction ratio of the PBSs, small fractions of each reflected beam leak into the path of the other with an intensity of tens of nanowatts. This is enough for the cooling beam to be detected in our homodyne scheme and for the probe beam to introduce an interference pattern in the PDH-locking signal, making the frequency lock unstable. These side-effects can be minimized operating at low power, at the cost of imposing an upper boundary to the setup performances. In the version of the feedback-cooling experiment presented in Sec. 4.5, the cooling beam is produced by a different laser than the probe and local oscillator, with the wavelengths of the two lasers differing by an amount corresponding to several FSRs of the cavity. As the cooling beam cannot interfere

with the probe nor the local oscillator, the PDH lock is not hindered and homodyne detection of the cooling beam is not possible. Please note that in this case the two lasers rely on independent locking schemes. Light transmitted through the cavity is detected to frequency-lock the probe laser so that no tap-off of its reflection is required.

Optical losses need to be minimized in order to enhance the performance of our feedback cooling scheme, tackling all their sources. To begin with, sub-optimal optical components must be replaced by less lossy ones. The same goes for the photodiodes used in homodyne detection, which need to be replaced with higher quantum-efficiency ones. Some effort went into increasing the visibility, which was ultimately limited to 0.80 due to spherical aberrations in the back-reflected probe profile. Improving the alignment of back-reflected light through the mode-matching lenses while keeping a high mode-matching efficiency of the cavity is rather cumbersome, due to the long distance between the lenses and the cavity and to the out-of-plane geometry of the setup. The next version of our feedback cooling experiment is based on cavities whose axis is parallel to the optical table. The new optomechanical assembly and vacuum chamber were designed to minimize the distance of the incoupling mirror from the mode-matching lenses. This allows to increase the visibility above 0.9. The cavity escape efficiency can be increased by decreasing the reflectivity of the incoupling mirror, although in this case a trade-off must be found in order to avoid a stark decrease in optomechanical cooperativity.

As a rule of thumb, feedback cooling into the ground state requires the measurement-induced quantum back-action to affect the mechanical motion at a rate  $\Gamma_{ba} = 4 \frac{g_0^2 N_{cav}}{k}$  faster than the thermal decoherence rate  $\gamma_{th} = \Gamma_M (\bar{n} + 1/2)$ . This translates into a condition on the optomechanical quantum cooperativity

$$\frac{\Gamma_{ba}}{\gamma_{th}} = \frac{4 \frac{g_0^2 N_{cav}}{k}}{\Gamma_M (\bar{n} + 1/2)} = C_q \geq 1 \quad (4.24)$$

Under the experimental conditions of our experiment, an optical power of 1  $\mu$ W produces a cooperativity of about  $2 \times 10^{-7}$ , very far from our target. At first one might think such a low value can be compensated for by increasing the input optical power, hence the intracavity photon number. This is actually not experimentally feasible. The polarization-leakage problems discussed above prevent us from using arbitrarily intense beams and homodyne detection requires a high power ratio between local oscillator and signal (ideally at least 100 times). Since our detector's electronics typically saturates for an input power higher than few milliwatts, this brings about a limit to the maximum probe power we can use. Other routes to increase cooperativity were thus explored. To begin with, the cavity linewidth was decreased to 15 MHz, lower by a factor of 32 with respect to Jan Bilek's experiment. Please note that decreasing the optical linewidth increases cooperativity not only through their inverse proportionality relation, but also indirectly by increasing the number of intracavity photons per unit of input optical power. Unfortunately, further linewidth reduction is not possible as the mirrors used so far already represent the lowest-transmission option on the market for a wavelength of 1550 nm.

The most convenient way for us to enhance  $C_q$  is through an increase the single-photon optomechanical coupling  $g_0$ , given the quadratic relation between them. Eq. 3.74 shows  $g_0 \propto \Theta$  with  $\Theta$  quantifying the spatial overlap between the mechanical and optical modes of choice. Recalling Eq. 3.75, we can easily simulate the behaviour of the optomechanical coupling for different positions of the trampoline central pad with respect to the light propagation axis inside the cavity. As we can see from Fig. 4.10, steering the optical field away from the center of the trampoline results in a dramatic reduction of coupling. For this computation, the mechanical mode shape was imported directly from the FEM simulation used to design the trampoline instead of using Eq. 3.72. Given the strong impact of the spatial overlap over the optomechanical coupling, quite some effort went into improving the alignment between our cavity and the trampoline. A value of  $g_0 = 2\pi \times 3.3$  Hz

measured, representing a fourfold increase with respect to what reported by Jan Bilek. Our optomechanical assembly allows the cavity spherical mirror to be moved around in the plane perpendicular to the light propagation axis using an xy stage, whose precision is in the order of fractions of a millimeter. This is not good enough, considering the side length of a trampoline central pad is around  $150\ \mu\text{m}$  and the beam waist inside the cavity is approximately  $40\ \mu\text{m}$ , while the side length of the chip windows of our mechanical resonators ranges between  $0.7$  and  $3\ \text{mm}$ . A better approach is found by designing an optomechanical assembly with no degrees of freedom, where the alignment between the mechanical resonator and the cavity is defined by matching references etched into the oscillator silicon chip and carved into the metal assembly. The alignment precision is then limited by the error in the CNC machining of the assembly, which is estimated to be lower than  $15\ \mu\text{m}$ . The optomechanical cavities presented in the next section were built following this approach.

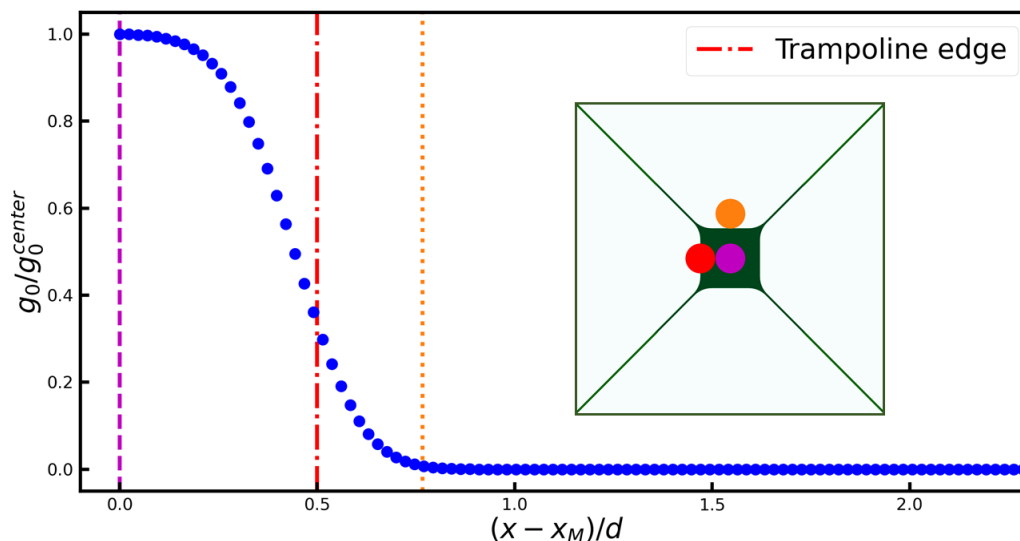


Figure 4.10: Optomechanical coupling as a function of the distance between the cavity axis and the center of our trampoline. Coupling was normalized to its peak value at the center of the trampoline, while distance was normalized to the trampoline side length  $d$ . Inset shows the beam positions corresponding to the vertical lines.

Taking all changes into account, an increase of optomechanical cooperativity of around 500 times per unit of intracavity photons was achieved with respect to Jan Bilek’s experiment. While we both worked with the same trampoline, quantum optomechanical cooperativity can also be enhanced by engineering the properties of the mechanical resonator, given the direct proportionality to its mechanical quality factor. The two membranes presented in the next half of this chapter have been designed bearing this criterion in mind.

## 4.5 Optomechanical feedback cooling II

The second half of my PhD was focused on designing and building an experimental setup capable of producing better results than the previous one, thus feedback-cooling a mechanical mode even closer to the ground state. This new setup was conceived around the idea of using a different, in-plane cavity geometry and new kinds of mechanical resonators yielding higher quality factors. In particular, a phononic membrane and a topology-optimized trampoline (TOTrampoline) were placed in optical cavities with different properties. In the following, experimental results obtained on both systems will be presented.

## 4.5.1 Experimental setup

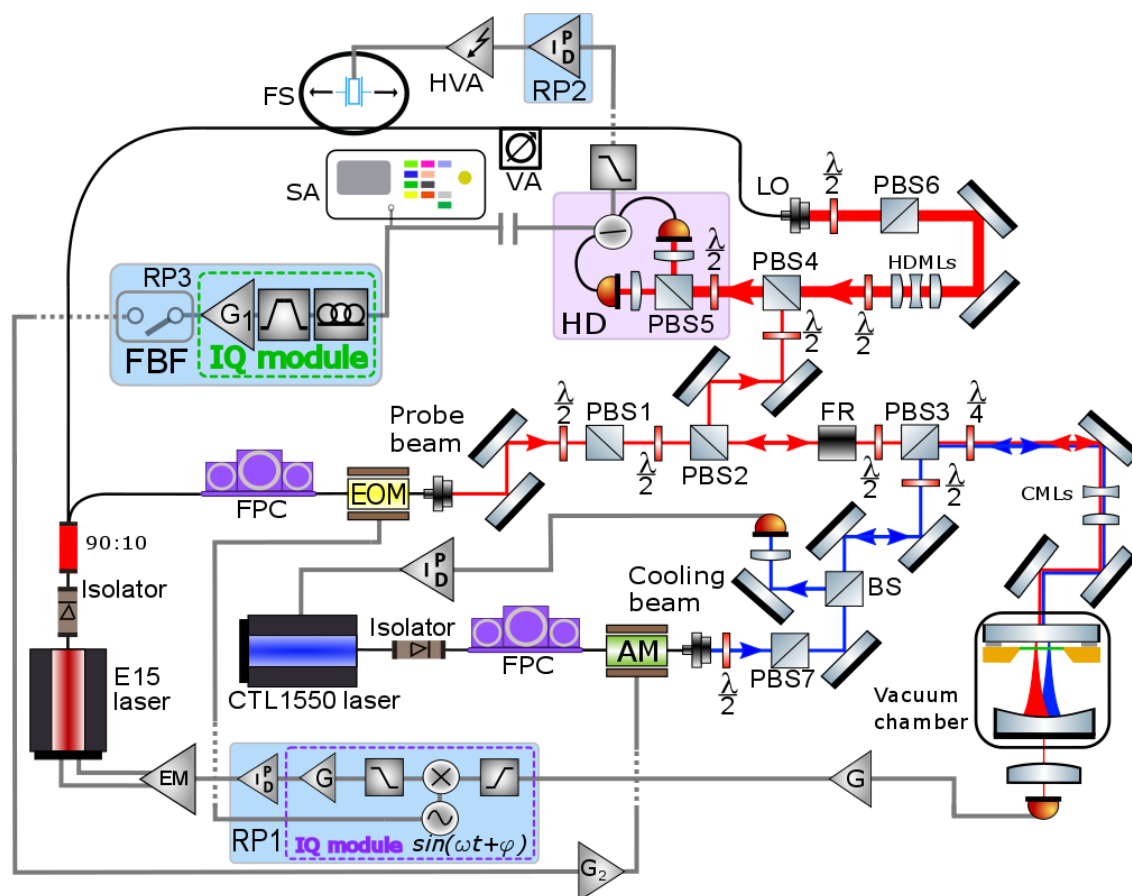


Figure 4.11: Experimental setup used for the second version of our feedback cooling experiment. Acronyms: evaluation module (EM), fiber polarization controller (FPC), electro-optic modulator (EOM), amplitude modulator (AM), polarization beam splitter (PBS), beam splitter (BS), Red Pitaya (RP), feedback filter (FBF), amplification gain (G), half-wave plate ( $\lambda/2$ ), quarter-wave plate ( $\lambda/4$ ), Faraday rotator (FR), homodyne mode-matching lenses (HDMLs), cavity mode-matching lenses (CMLs), homodyne detector (HD), spectrum analyser (SA), fiber stretcher (FS), high-voltage amplifier (HVA), variable attenuator (VA), 90/10 fiber beam splitter (90:10).

Fig. 4.11 shows the setup used for the second version of our feedback-cooling experiment, which is largely similar to the one described in Sec. 4.4.1 with some major differences. To begin with, the axis of the cavity is parallel to the optical table, thus removing the need for a  $45^\circ$ -mirror steering light onto the vertical direction. Combined with the smaller vacuum chamber, this allows for a much shorter distance between the steering mirrors placed before the cavity and the incoupling mirror, making mode-matching easier. The optomechanical assembly we use is described in detail in Sec. 3.3.6.2. Matching references etched into the mechanical-resonator carrier chip and machined into the assembly enable to precisely steer light through the center of the oscillator. As mentioned above, separate lasers were used to sense the mechanical motion and apply the feedback force. Given the need for low-phase noise, a NKT Koheras Adjustik E15 (red laser in Fig. Fig. 4.11) was chosen for the probe and 90% of its output power was tapped off using an asymmetric fiber beam splitter to provide a local oscillator (LO) for homodyne detection. A fiber polarization controller (FPC) ensures the laser polarization matches the optical axis of an EOM and prevents the perpendicular polarization component from generating amplitude modulation of the light. The phase modulator is used to implement a PDH scheme to lock the laser frequency to the cavity. As

the the optomechanical assembly allows no degrees of freedom for the cavity mirrors, frequency stabilization is achieved actuating the internal piezo of the laser. The PDH error function is generated detecting light transmitted through the cavity by a photodiode Thorlabs APD430C/M and feeding it to a Red Pitaya 125-14 (RP1) after a fixed gain  $G$  is applied. The digital device carries out the function of signal generator, demodulation circuit and PID controller and its output goes through an evaluation module (EM) providing an electronic interface with the laser. A Toptica CTL 1550 (blue laser in Fig. Fig. 4.11) was chosen to provide the feedback force due to its low amplitude noise and wide frequency tunability, which was exploited to align light to the cavity. A photodiode Thorlabs PDA10CF-EC detects reflected light and its output is fed to the Toptica laser controller, whose electronics generates the error function for frequency locking to the cavity. More details about the two frequency-stabilization schemes are given in Sec. 3.3.8. Although the laser beams are overlapped in free space onto PBS3 and have orthogonal polarization, small power leakages generate the interference issues described in Sec. 4.4.5. We then take advantage of the wide tunability of the Toptica laser and operate it at a wavelength corresponding to a spacing of one cavity FSR from the NKT laser frequency, thus preventing interference. A quarter-wave plate is placed before the cavity mode-matching lenses to maximize the probe light back-reflected into the homodyne setup. Lenses (HDMLs) were added to the path of the local oscillator to increase the homodyne visibility. The analog PID controller previously in use for phase lock in homodyne detection was replaced by a digital one, hosted by a Red Pitaya 125-10 (RP2). A separate Red Pitaya 125-10 (RP3) operates the feedback filter (FBF).

## 4.5.2 Phononic membrane

The first mechanical resonator we deal with is a phononic membrane, fabricated according to a design proposed by Schliesser et al. in 2017 [24]. Fig. 4.12a shows a microscope image of it, displaying a  $3\text{ mm} \times 3\text{ mm}$  silicon nitride layer within which a honeycomb hole pattern is fabricated. The membrane thickness of approximately 20 nm yields a mass around 0.4 ng, whose value was estimated by finite-element modeling. Due to the honeycomb structure, a phononic bandgap opens within the continuum of out-of-plane vibrational modes of the membrane. Engineering a defect at the center of the resonator causes the appearance of localized modes corresponding to frequencies within the bandgap itself, as showed in Fig. 4.12b. These modes are usually referred to as *soft-clamped* modes as their shape gradually decays into the periodic structure, unlike the modes of an unpatterned membrane surrounded by a rigid frame. Combined with the stress redistribution brought about by the phononic crystal, this causes the localized modes to feature a high quality factor. Our membrane, whose bandgap opens approximately between 1.27 and 1.5 MHz, was engineered to maximize the quality factor of the lowest-frequency bandgap mode at  $\Omega_M = 2\pi \times 1.366\text{ MHz}$ , which exhibits a Gaussian profile (see simulation Fig. 4.12d). This mode is the subject of our feedback-cooling experiment. Ringdown measurements have been performed on it both while the membrane was part of a large silicon wafer and after dicing this into small  $1\text{ cm} \times 1\text{ cm}$  chips. A decrease of the mechanical quality factor was observed from an original value of  $3.0 \times 10^7$  down to  $2.1 \times 10^6$ . This drop of one order of magnitude was not investigated thoroughly, but two hypotheses were made. To begin with, it could be due to contamination of the chip. This explanation seems to be supported by a  $\approx 60\text{ kHz}$  decrease of the mode frequency observed after dicing the wafer, which may stem from particles depositing on the membrane and increasing its mass. A second possibility is given by the different clamping technique used for the diced chip, which might open more channels of phonon tunneling. This explanation is considered less likely as phononic-crystal structures usually prevent such behaviour, isolating the bandgap modes from the environment.

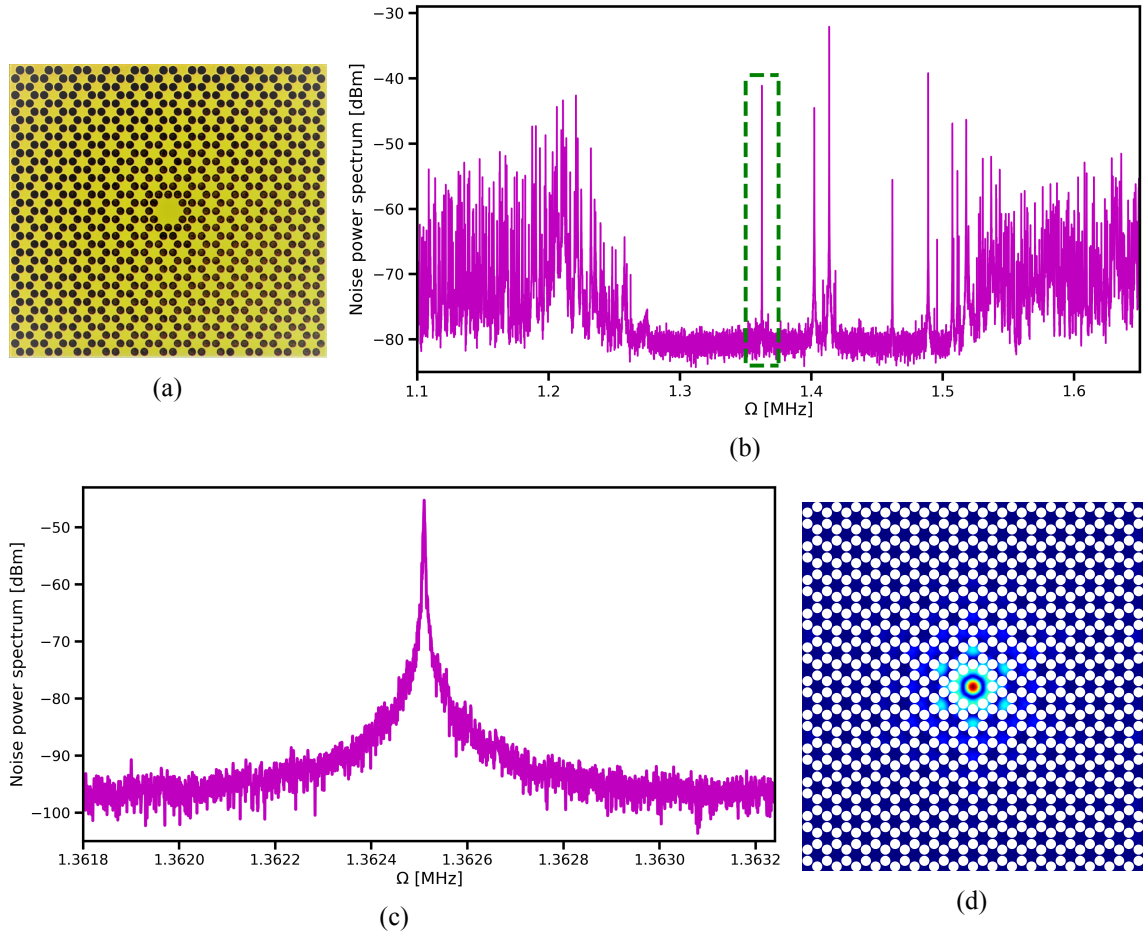


Figure 4.12: a) Microscope image of our phononic membrane, showing its honeycomb pattern and the central defect. b) Noise power spectrum of our membrane, displaying the bandgap opening amidst the continuum of vibrational modes. The green dashed square highlights the lowest-frequency bandgap mode at  $\Omega_M = 2\pi \times 1.366$  MHz, which is the subject of our experiments. c) Zoom-in on the lowest-frequency bandgap mode. d) Simulation of the vibrational out-of-plane motion of the lowest-frequency bandgap mode, featuring a Gaussian profile.

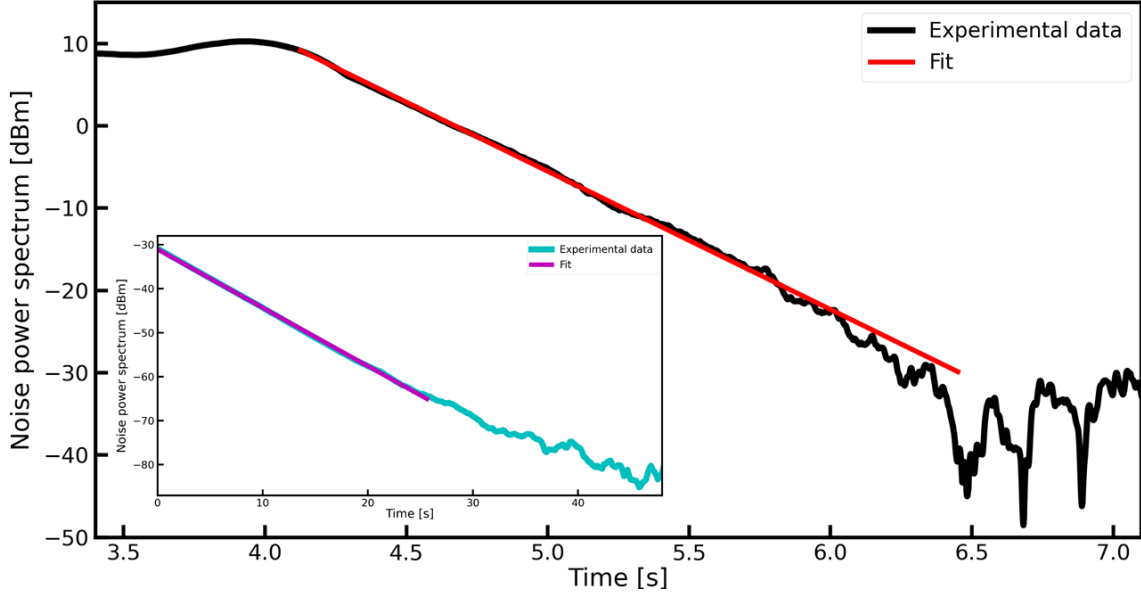


Figure 4.13: Ringdown measurement of the lowest-frequency bandgap mode of our phononic membrane after dicing the wafer into chips, corresponding to a quality factor of  $2.1 \times 10^6$ . Inset shows results of the same measurement performed before dicing, which yield a quality factor of  $3.0 \times 10^7$ .

### 4.5.3 Phononic membrane: Experimental parameters

Table 4.2 reports the main parameters of our experimental setup. Due to practical considerations in manufacturing and assembling, the cavity is about 1.85 mm long, almost twice the size of the previous one. This value includes the thickness of a 420  $\mu\text{m}$  silicon spacer placed between the membrane and the incoupling mirror to prevent them from touching each other. At a wavelength around 1550 nm, such length corresponds to an FSR of 80.47 GHz. The plane and spherical mirrors of the cavity feature a nominal transmission of 400 ppm and 200 ppm, respectively, leading to a cavity linewidth of  $\approx 2\pi \times 18.08$  MHz at the operating wavelength of both lasers. The cavity finesse is around 4453 and, given the mechanical mode frequency of  $\Omega_M = 2\pi \times 1.366$  MHz, we see that our system still lies within the unresolved sideband regime. The escape efficiency was measured for both probe and cooling beam, obtaining values of 0.83 and 0.78, respectively. These show an increase with respect to the 0.7 value obtained for the vertical-cavity setup.

Optical losses along the path of the probe light reflected off the cavity amount to an efficiency of  $\eta_{opt} = 0.89$ . In order to achieve this increase with the respect to the 0.68 value of the previous setup, all the optical components have been either cleaned or replaced by new ones. Particular attention was paid to the lossier components, such as the Faraday rotator and the PBSs. The former was replaced by a new Thorlabs I1550R5 with 0.98 transmission. The standard Thorlabs PBSs used in the previous experiment have been replaced by custom-made ones from Altechna, ensuring minimum values of 97% for the transmission of p-polarization and 99.5% for the reflectance of s-polarization. Using lenses to mode-match the local oscillator profile to the probe, visibility is increased from the previous value of 0.8 to 0.9. This improvement was possible also thanks to the horizontal-cavity geometry, which helps preventing spherical aberrations in the back-reflected light. Photodiodes were not replaced for this experiment, so their quantum efficiency is still 0.76. These numbers add up to an overall homodyne detection efficiency of  $\eta_D = 0.55$  and to a total efficiency of  $\eta = \eta_D \eta_{esc} = 0.45$ .

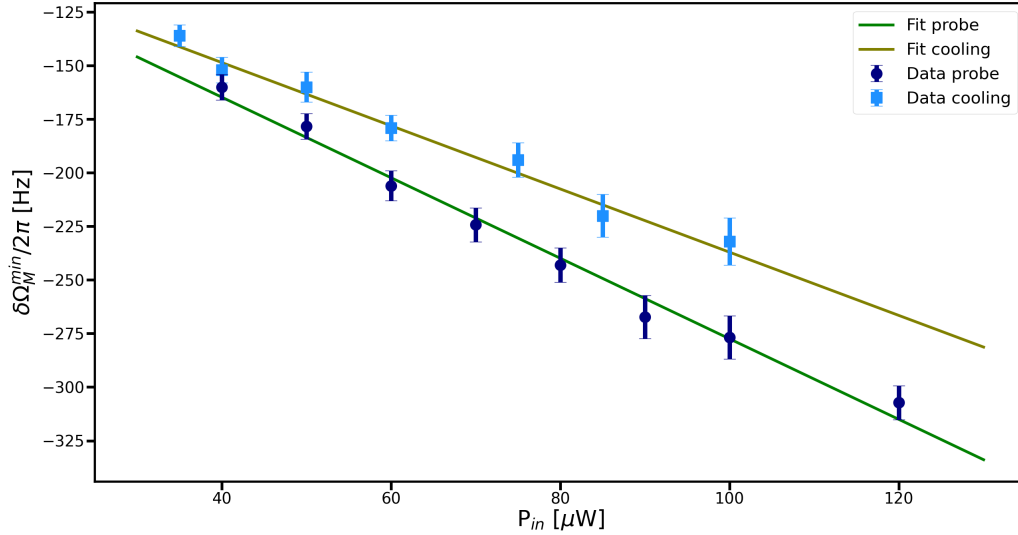
The single-photon optomechanical coupling  $g_0$  between the lowest-frequency bandgap mode and the fundamental intracavity mode at 1550.17 nm was measured by both spring effect and quantum noise thermometry. The values obtained from these two techniques are  $2\pi \times (10.5 \pm 0.3)$  Hz and  $2\pi \times (10.1 \pm 0.8)$  Hz, respectively, and show a threefold increase with respect to the previous

experiment. Measurement results are presented in Figs. 4.14a-b. It is remarkable that the two techniques yield compatible results, at they are based on rather different assumptions. As the CTL1550 laser is locked to a different longitudinal cavity mode at a wavelength of 1550.87 nm, the coupling rate of the cooling field needs to be evaluated independently. We do so using the spring effect again. In this case we first lock the E15 laser on resonance with the cavity and perform homodyne detection of the probe beam observing the zero-detuning mechanical mode, then the CTL1550 is locked on the red side of the cavity. Sweeping the cooling-beam power we observe a proportional downshift of the mechanical frequency, from which we can infer a single-photon optomechanical coupling of  $g_0^{cool} = 2\pi \times (9.6 \pm 0.5)\text{Hz}$ . Please note that given the  $\approx 150 \mu\text{m} \times 150 \mu\text{m}$  size of the membrane central defect compared to the  $\approx 3 \text{mm} \times 3 \text{mm}$  chip window, good alignment between the cavity axis and the oscillator is even more critical than in the case of trampolines, whose chip window was approximately 1 mm wide. Attempts to feedback-cool the motion of a phononic membrane in our vertical cavity were previously carried out with very unsatisfactory results, as the poor spatial overlap between light and mechanical displacement field yields a coupling rate below  $2\pi \times 1 \text{Hz}$ .

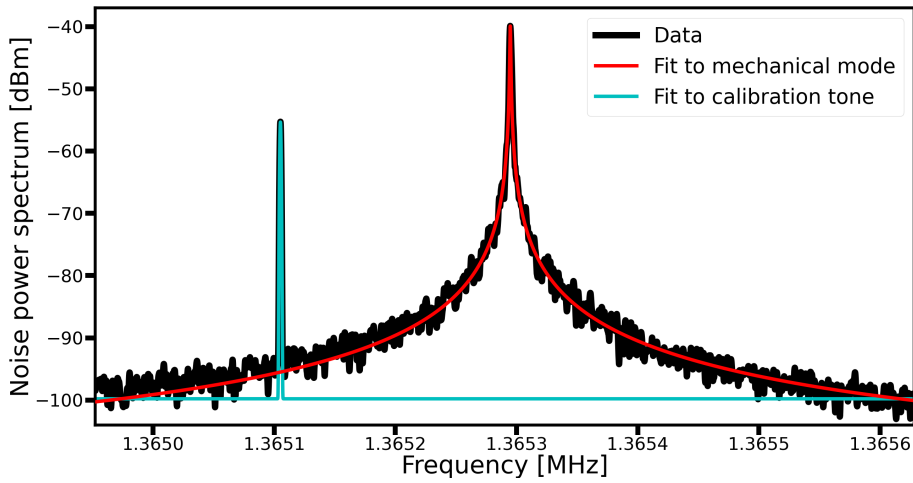
Figs. 4.15a and b present a measurement of the amplitude and phase of the bandpass filter used for feedback cooling of the lowest-frequency bandgap mode. A bandwidth of  $\Gamma_{fb} = 2\pi \times 9.15 \text{kHz}$  and a group delay of  $\tau = 280 \text{ns}$  were measured.

<b>Experimental parameters</b>		
E15 laser wavelength		1550.17 nm
CTL1550 laser wavelength		1550.87 nm
Cavity FSR		80.47 GHz
Cavity linewidth at 1550.17 nm	$k_p$	$2\pi \times 18.07 \text{MHz}$
Cavity linewidth at 1550.87 nm	$k_c$	$2\pi \times 18.08 \text{MHz}$
Cavity finesse	$\mathcal{F}$	4453
Escape efficiency of probe beam at 1550.17 nm	$\eta_{esc}^p$	0.83
Escape efficiency of cooling beam at 1550.87 nm	$\eta_{esc}^c$	0.78
Efficiency of optical components	$\eta_{opt}$	0.89
Homodyne visibility	$\nu$	0.90
Quantum efficiency of homodyne detection	$\eta_{QE}$	0.76
Total homodyne-detection efficiency	$\eta_D = \eta_{opt}\nu^2\eta_{QE}$	0.55
Total efficiency	$\eta = \eta_D\eta_{esc}$	0.45
Mechanical oscillator frequency	$\Omega_M$	$2\pi \times 1.366 \text{MHz}$
Mechanical quality factor	$Q$	$2.1 \times 10^6$
Mechanical linewidth	$\Gamma_M$	0.65 Hz
Effective mass	$m_{eff}$	0.4 ng
Mechanical zero-point displacement amplitude	$x_{zpf}$	3.9 fm
Single-photon optomechanical coupling, probe beam	$g_0$	$2\pi \times 10.3 \text{Hz}$
Single-photon optomechanical coupling, cooling beam	$g_0^{cool}$	$2\pi \times 9.6 \text{Hz}$
Feedback filter linewidth	$\Gamma_{fb}$	$2\pi \times 9.15 \text{kHz}$
Feedback filter delay	$\tau$	280 ns
Mechanical bath temperature	$T$	300 K
Thermal phonon occupancy number	$n_{th} = k_B T / \hbar \Omega_M$	$\approx 4.58 \times 10^6$

Table 4.2: Specifications of the optomechanical setup used for feedback cooling of the lowest-frequency bandgap mode of our phononic membrane.



(a)



(b)

Figure 4.14: Measurement of the single-photon optomechanical coupling of between the lowest-frequency bandgap mode of our phononic membrane and the fundamental mode of the intracavity field through a) spring effect and b) quantum noise thermometry. The values obtained are respectively  $2\pi \times (10.5 \pm 0.3)\text{Hz}$  and  $2\pi \times (10.1 \pm 0.8)\text{Hz}$ . Coupling rate of the feedback field at a wavelength of 1550.87 nm to the mechanical mode was measured independently through spring effect, obtaining a value of  $g_0^{cool} = 2\pi \times (9.6 \pm 0.5)\text{Hz}$ .

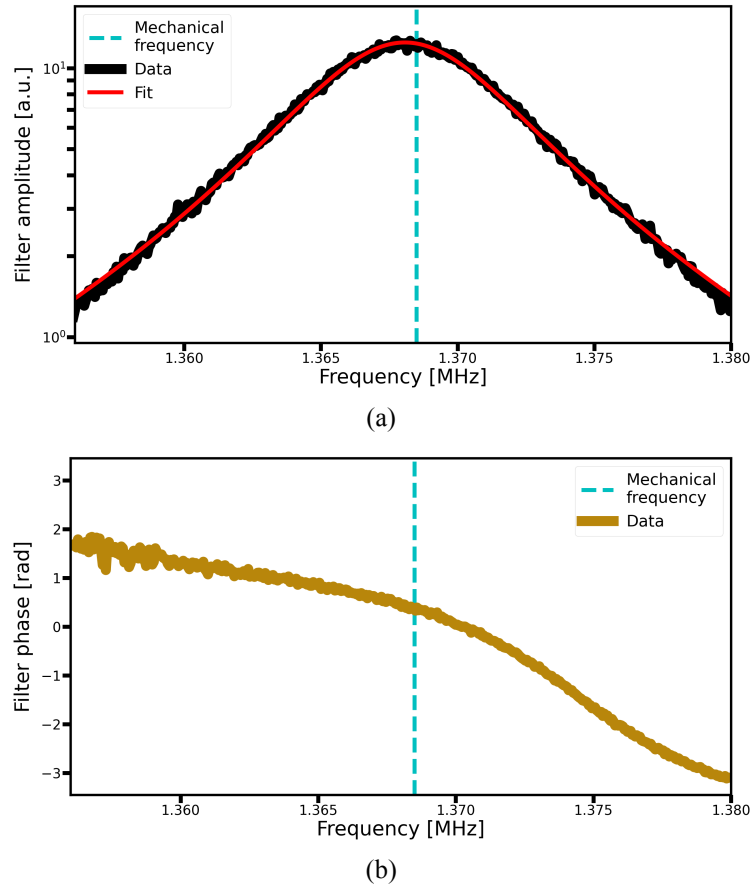
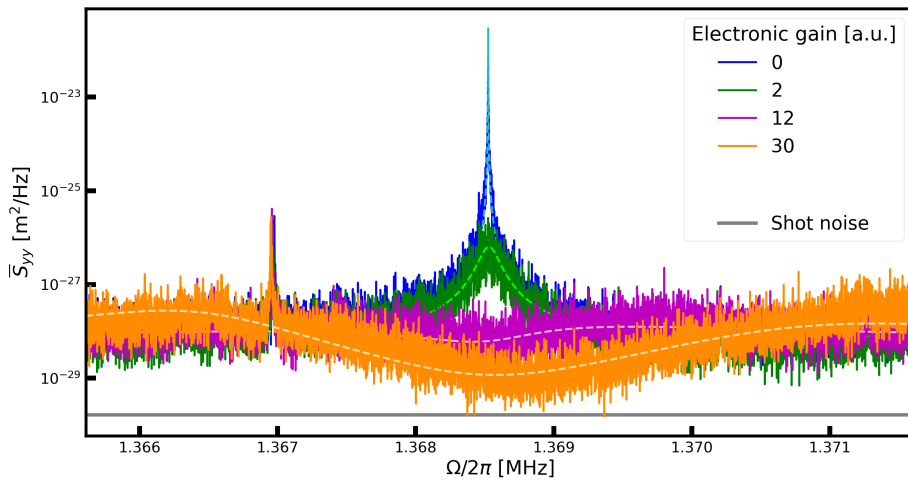


Figure 4.15: a) amplitude and b) phase of the bandpass filter used for feedback cooling of the lowest-frequency bandgap mode of our phononic membrane. The dashed cyan line indicates the vibrational-mode frequency of interest. A filter linewidth of  $\Gamma_{fb} = 2\pi \times 9.15$  kHz and a group delay of  $\tau = 280$  ns were measured.

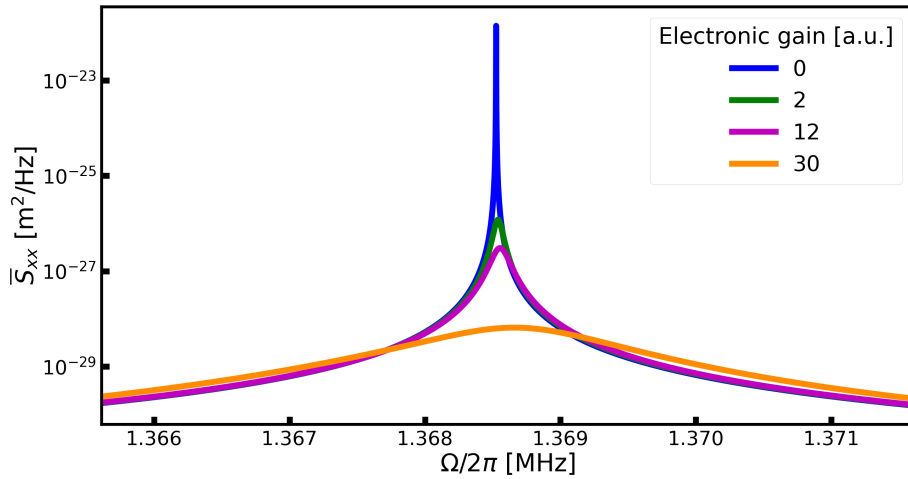
#### 4.5.4 Phononic membrane: Results

Figs.4.16a-b shows our best results for feedback cooling of the lowest-frequency bandgap mode of a phononic membrane. Measurements were carried out following the same method explained for the trampoline in the previous section. The input power of probe and cooling beam was set to  $100 \mu\text{W}$  each and the two lasers were locked on resonance with the cavity. Spectra of the in-loop mechanical displacement were acquired averaging over 10 traces and setting both the resolution and video bandwidth to 1 Hz. As we can see from Fig.4.16a, our measurement is once again not shot-noise limited. The shot noise appears as a flat line (grey in figure) because in our calibration method all spectra are normalized to it. We detect the presence of a small mode around 1.367 MHz. Although this lies within the  $2\pi \times 9.15$  kHz linewidth of our feedback filter, it is not subject to feedback cooling due to its weak coupling to the light. Data were fitted to Eq. 4.23 in order to infer the out-of-loop mechanical-displacement spectra displayed in Fig. Fig.4.16b. Increasing the electronic gain decreases the area underneath the out-of-loop spectra, hence the phonon occupancy number. Fig.4.17 shows a comparison between the  $\Gamma_{eff}$  vs  $\bar{n}$  data measured experimentally and a theoretical model obtained using the  $n_{imp}$  and  $n_{tot}$  estimated from the zero-gain mechanical displacement and setting  $\arg[h_{fb}(\Omega_M)] = \pi/2$ . Good agreement is found between theory and experiment, with the initial phonon occupancy number of  $n_{th} = 4.58 \times 10^6$  being cooled down to a minimum of  $\bar{n}^{min} = 1800 \pm 200$  for an effective linewidth of  $\Gamma_{eff} = 2\pi \times 3.39$  kHz and electronic gain of 30 (orange octagon). The minimum occupancy number predicted by our theoretical model

is 1899. Increasing the electronic gain above the minimum-occupancy value causes squashing of the in-loop mechanical displacement spectrum and heating of the mechanical resonator.



(a)



(b)

Figure 4.16: a) In-loop mechanical-displacement noise spectra of the lowest-frequency bandgap mode of a phononic membrane acquired for different electronic gains. The dashed lines are obtained fitting the data to Eq. 4.23. The shot noise (grey) appears as a flat line because in our calibration method all spectra are normalized to it. The corresponding inferred out-of-loop spectra are displayed in Fig.b.

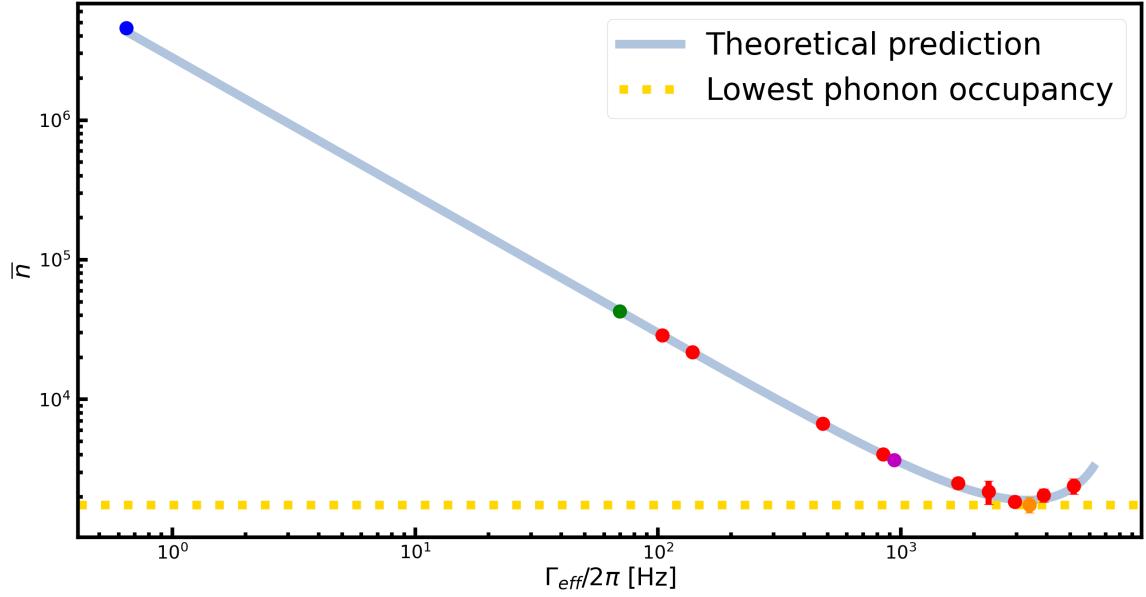


Figure 4.17: Feedback cooling of the lowest-frequency bandgap mode of a phononic membrane. Phonon number occupancy  $\bar{n}$  as a function of the effective mechanical linewidth  $\Gamma_{eff}$ . Blue, green, purple and orange octagons represent the values extracted from the spectra in Figs. 4.16a-b. The red markers describe the values computed for other spectra from the same dataset. The dotted yellow line marks the lowest measured phonon occupancy  $\bar{n}^{min} = 1800 \pm 200$ , represented by the orange circle. Results are compared with a theoretical prediction (grey line) obtained using the  $n_{imp}$  and  $n_{tot}$  values estimated for zero gain and assuming  $\arg[h_{fb}(\Omega_M)] = \pi/2$ .

## 4.5.5 Topology-optimized trampoline

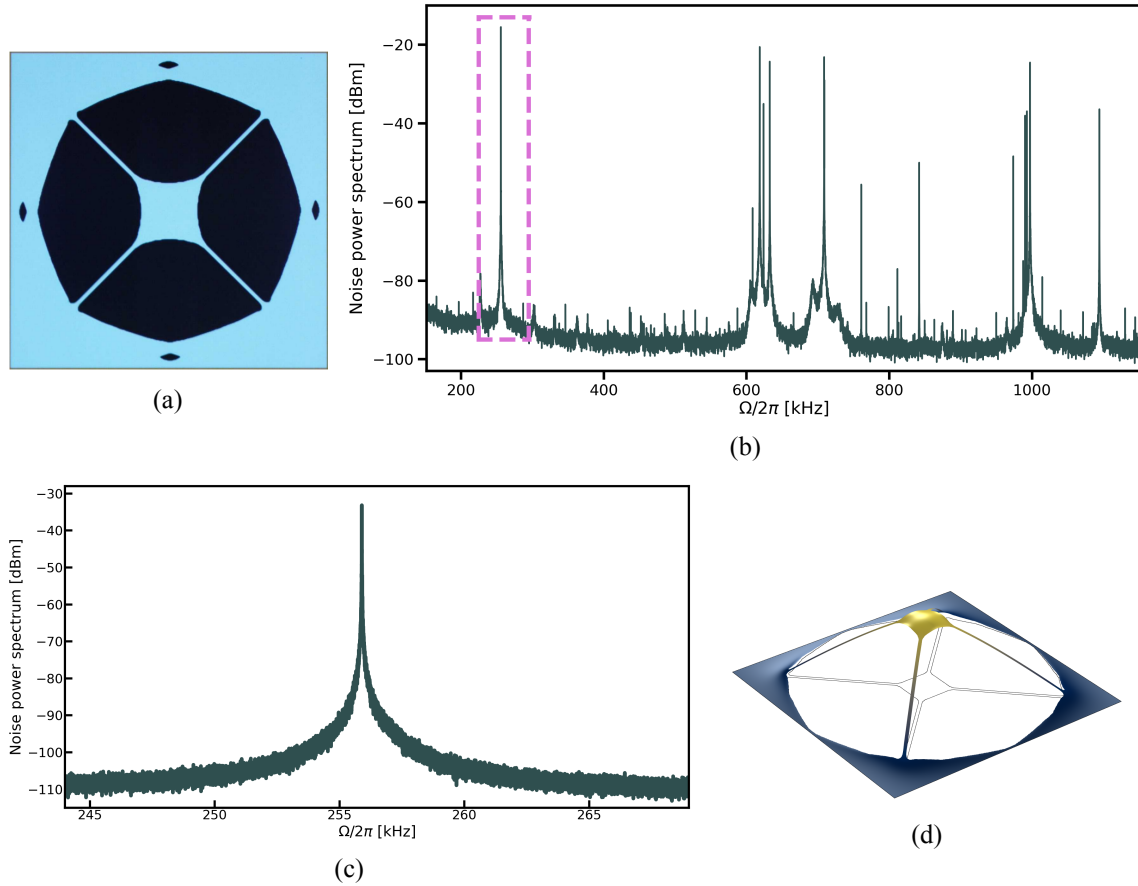


Figure 4.18: a) Microscope image of our topology-optimized trampoline (TOT). b) Noise power spectrum of our TOT, displaying discrete modes at a spacing comparable to the fundamental-mode frequency. The pink dashed square highlights the fundamental vibrational mode at  $\Omega_M = 2\pi \times 256$  kHz, which is the subject of our experiments. c) Zoom-in on the fundamental mode. d) Simulation of the vibrational out-of-plane motion of the fundamental mode.

The last mechanical resonator presented in this work is a topology-optimized trampoline (TOT or TOTrampoline). This consists of a tethered membrane designed following a computational method proposed by Dennis Høj while working in our group [17]. Optimization of the shape and proportions of oscillators aiming at the enhancement of their coherence is usually performed following human intuition and knowledge of approximative analytical solutions or simply by trial and error in fabrication. This approach is inherently inefficient, as it leads to essentially overlook many potential designs with better performances. On the other hand, topology optimization is a computational procedure widely used in engineering [44, 45] to determine the best geometry and material distribution of a structure within a prescribed design domain. This technique can be applied and fine-tuned to design mechanical resonators with fundamental vibrational modes of unprecedented  $Qf$  product [46]. Dennis Høj's algorithm follows a gradient-wise computational method based on a physical model of the system. Material is redistributed within the structure through many iterations in order to reach an optimal design minimizing or maximizing a particular figure of merit.

Fig. 4.18a shows a microscope image of our our TOTrampoline, featuring a  $100 \mu\text{m} \times 100 \mu\text{m}$  central pad connected by tethers to the  $700 \mu\text{m} \times 700 \mu\text{m}$  window of the carrier chip. Upon designing the resonator these dimensions were fixed, while the remaining space within the window frame was free to evolve following the topology optimization algorithm. The noise power spectrum of

our TOTrampoline is depicted in Fig. 4.18b and displays discrete modes as in the case of the old-generation trampoline presented in Section 4.4.2. The membrane thickness of 16 nm makes for an effective mass of 1.06 ng, which combined with the high tensile strain of the silicon nitride layer yields a frequency of  $\Omega_M = 2\pi \times 256$  kHz for the fundamental mode (see Fig. 4.18c).

Similarly to the phononic membrane, we observe a strong decrease of the mechanical quality factor after dicing the silicon wafer into chips. This dropped from an original value of  $1.1 \times 10^8$  down to  $1.7 \times 10^6$ , as we show in Fig. 4.19. At the same time, the fundamental mode frequency lowered from 268 kHz to 256 kHz. It is still unknown to us whether such decrease is due to contamination of the samples during the dicing process or this is a result of the different clamping techniques used for the whole silicon wafers and the single chips.

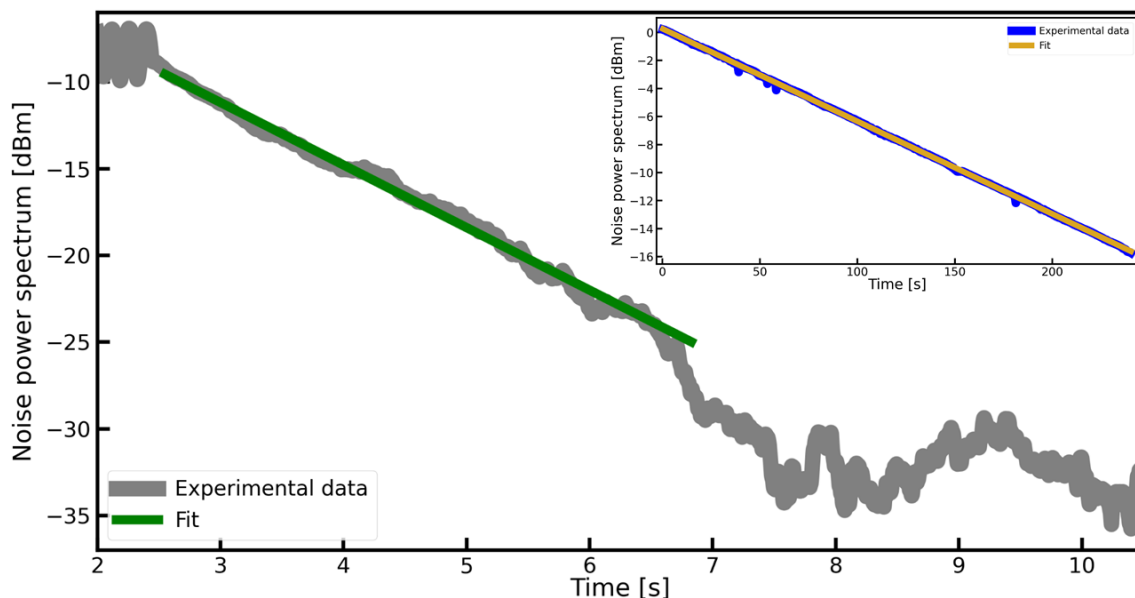


Figure 4.19: Ringdown measurement of the fundamental vibrational mode after dicing the wafer into chips, corresponding to a quality factor of  $1.7 \times 10^6$ . Inset shows results of the same measurement performed before dicing, which present a quality factor of  $1.1 \times 10^8$ .

#### 4.5.6 TOTrampoline: Experimental parameters

Table 4.3 reports the experimental parameters used for feedback cooling of the TOTrampoline. We used the same setup as in the case of our phononic membrane (see Secs. 4.5.1 and 4.5.3), although some changes were made. The cavity length was modified replacing the 420  $\mu\text{m}$ -thick silicon ring spacer with one of thickness 200  $\mu\text{m}$ , thus increasing the FSR to 92.89 GHz. The plane and spherical mirrors of the cavity were replaced by new ones featuring a transmission of 400 ppm and 10 ppm, respectively. The E15 and CTL1550 lasers were operated at a wavelength around 1550.28 nm and 1551.01 nm, respectively. This results in a cavity linewidth of  $2\pi \times 18.85$  MHz and a finesse of 4928 for the probe beam and to a linewidth of  $2\pi \times 18.60$  MHz and a finesse of 4994 for the cooling beam. Cavity escape efficiencies of  $\eta_{esc}^p = 0.83$  and  $\eta_{esc}^c = 0.76$  were measured for the probe and cooling beam, respectively.

As no other optical component was replaced along the probe path, the intrinsic optical losses still add up to an efficiency  $\eta_{opt} = 0.89$ . More effort was put into optimizing the mode-matching between probe and local oscillator, resulting in a homodyne visibility of 0.95. The standard InGaAs Thorlabs photodiodes used in homodyne detection were replaced by custom-made ones with 0.99 quantum efficiency manufactured at the Fraunhofer Heinrich Hertz Institute of Berlin. The homodyne detection efficiency is then  $\eta_D = 0.79$  and we obtain a total measurement efficiency of  $\eta = 0.66$ .

The single-photon optomechanical coupling  $g_0$  between the TOTrampoline fundamental mode and the intracavity mode to which the probe beam with wavelength 1550.25 nm is locked was once again measured by both spring effect and quantum noise thermometry. The values obtained are respectively  $2\pi \times (18.3 \pm 0.6)$ Hz and  $2\pi \times (18.6 \pm 0.9)$ Hz, showing good agreement between them. Figs. 4.20a and b show the experimental data. As the CTL1550 was locked to a different longitudinal cavity mode at a wavelength of 1551.01 nm, the coupling rate of the cooling field was measured independently using spring effect, obtaining a value of  $g_0^{cool} = 2\pi \times (17.5 \pm 0.4)$ Hz. Finally, the feedback filter linewidth was optimized to  $\Gamma_{fb} = 2\pi \times 77.33$  kHz and a group delay of 340 ns was measured. Figs. 4.21a and b display the measured amplitude and phase of the filter.

<b>Experimental parameters</b>		
E15 laser wavelength		1550.28 nm
CTL1550 laser wavelength		1551.01 nm
Cavity FSR		92.89 GHz
Cavity linewidth at 1550.28 nm	$k_p$	$2\pi \times 18.85$ MHz
Cavity linewidth at 1551.01 nm	$k_c$	$2\pi \times 18.60$ MHz
Cavity finesse at 1550.28 nm	$\mathcal{F}_p$	4928
Cavity finesse at 1551.01 nm	$\mathcal{F}_c$	4994
Escape efficiency of probe beam at 1550.28 nm	$\eta_{esc}^p$	0.83
Escape efficiency of cooling beam at 1551.01 nm	$\eta_{esc}^c$	0.76
Efficiency of optical components	$\eta_{opt}$	0.89
Homodyne visibility	$\nu$	0.95
Quantum efficiency of homodyne detection	$\eta_{QE}$	0.99
Total homodyne-detection efficiency	$\eta_D = \eta_{opt}\nu^2\eta_{QE}$	0.79
Total efficiency	$\eta = \eta_D\eta_{esc}$	0.66
Mechanical oscillator frequency	$\Omega_M$	$2\pi \times 256$ kHz
Mechanical quality factor	$Q$	$1.7 \times 10^6$
Mechanical linewidth	$\Gamma_M$	0.15 Hz
Effective mass	$m_{eff}$	1.1 ng
Mechanical zero-point displacement amplitude	$x_{zpf}$	5.6 fm
Single-photon optomechanical coupling, probe beam	$g_0$	$2\pi \times 18.5$ Hz
Single-photon optomechanical coupling, cooling beam	$g_0^{cool}$	$2\pi \times 17.5$ Hz
Feedback filter linewidth	$\Gamma_{fb}$	$2\pi \times 77.33$ kHz
Feedback filter delay	$\tau$	340 ns
Mechanical bath temperature	$T$	300 K
Thermal phonon occupancy number	$n_{th} = k_B T / \hbar \Omega_M$	$\approx 24.42 \times 10^6$

Table 4.3: Specifications of the optomechanical setup used for feedback cooling of the fundamental mode of our topology-optimized trampoline (TOT).

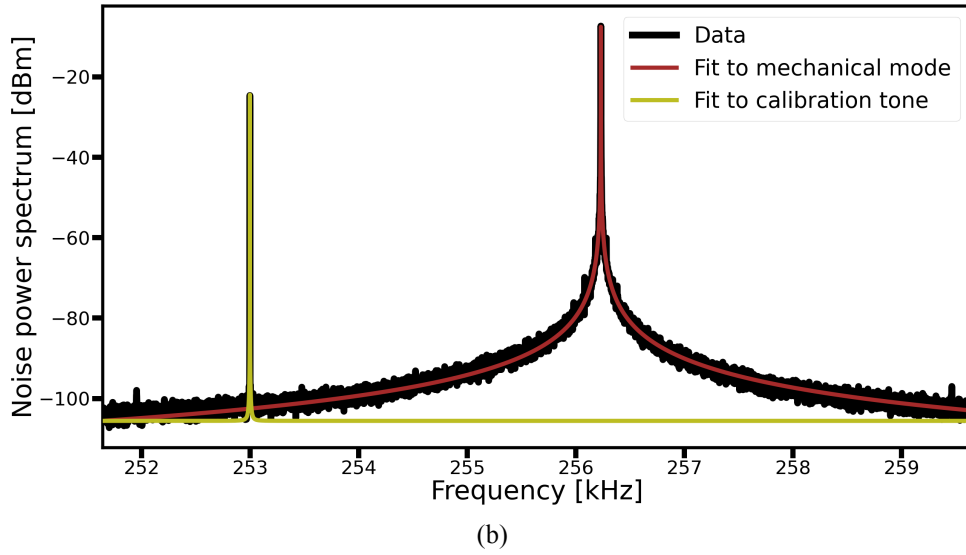
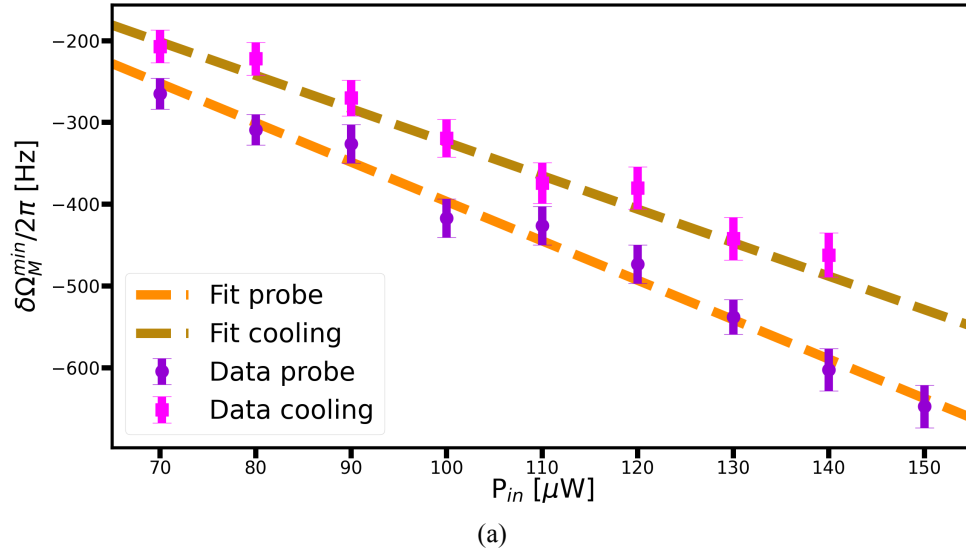


Figure 4.20: Measurement of the single-photon optomechanical coupling  $g_0$  of between the fundamental vibrational mode of our topology-optimized trampoline and the fundamental mode of the intracavity field at a wavelength of 1550.28 nm through a) spring effect and b) quantum noise thermometry. The values obtained are respectively  $2\pi \times (18.3 \pm 0.6)$  Hz and  $2\pi \times (18.6 \pm 0.9)$  Hz. Coupling rate was measured also for the cooling field at 1551.01 nm using the spring effect, obtaining  $g_0^{cool} = 2\pi \times (17.5 \pm 0.4)$  Hz.

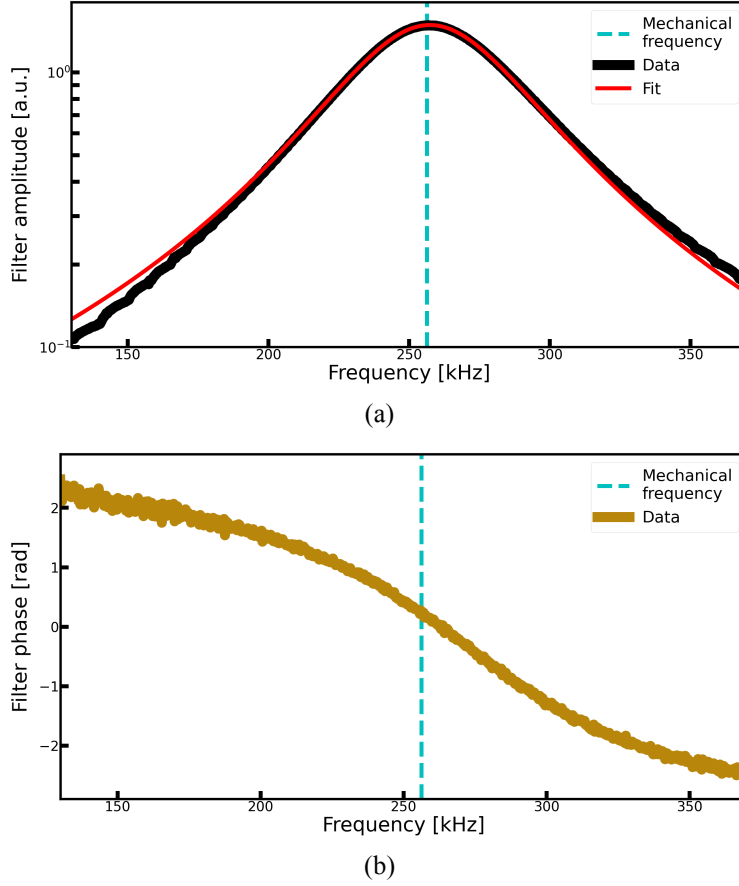


Figure 4.21: a) amplitude and b) phase of the bandpass filter used for feedback cooling of the fundamental vibrational mode of our topology-optimized trampoline. The dashed cyan line indicates the vibrational-mode frequency of interest. A filter linewidth of  $\Gamma_{fb} = 2\pi \times 77.33$  kHz and a group delay of 340 ns were measured.

#### 4.5.7 TOTrampoline: Results

Unlike the previous experiments, measurements on the TOTrampoline are close to being shot-noise limited, with the excess noise lying only about 1 dB above the shot noise, as we show in Fig. 4.22a. Although the precise cause of this excess-noise reduction was not investigated, we remark these measurements were carried out under different conditions of optical power, visibility and photodiode quantum efficiency, hence direct comparison with the case of our trampoline and phononic membrane is not possible.

Fig. 4.22b shows the results obtained for feedback cooling of the fundamental mode of a TOTrampoline with an input power of  $20 \mu\text{W}$  and  $5 \mu\text{W}$  for the probe and cooling beam, respectively. Both lasers were locked on resonance with the cavity. Spectra of the in-loop mechanical displacement were acquired averaging over 30 traces and setting both the resolution and video bandwidth to 1 Hz. Data were fitted to Eq. 4.23 and the out-of-loop spectra were thus inferred (Fig. 4.22c). Integrating the area under these, the phonon occupancy number  $\bar{n}$  was computed. Fig. 4.23 shows the  $\Gamma_{eff}$  vs  $\bar{n}$  curve, with  $\Gamma_{eff}$  being the effective mechanical linewidth. Cooling of the fundamental mode from  $n_{th} = 24.42 \times 10^6$  down to  $\bar{n}^{min} = (2940 \pm 40)$  was achieved for an electronic gain of 9 and effective linewidth of  $2\pi \times 2.5$  kHz, representing our best result for this kind of mechanical resonators. Errorbars were omitted as their length is smaller than the diameter of the dots representing the experimental data. Comparing with the theoretical model given by the  $n_{imp}$  and  $n_{tot}$  values inferred at room temperature and assuming  $\arg[h_{fb}(\Omega_M)] = \pi/2$ , we obtain a good agreement,

with a predicted minimum phonon occupancy of  $\bar{n}_{theory}^{min} = 2974$ .

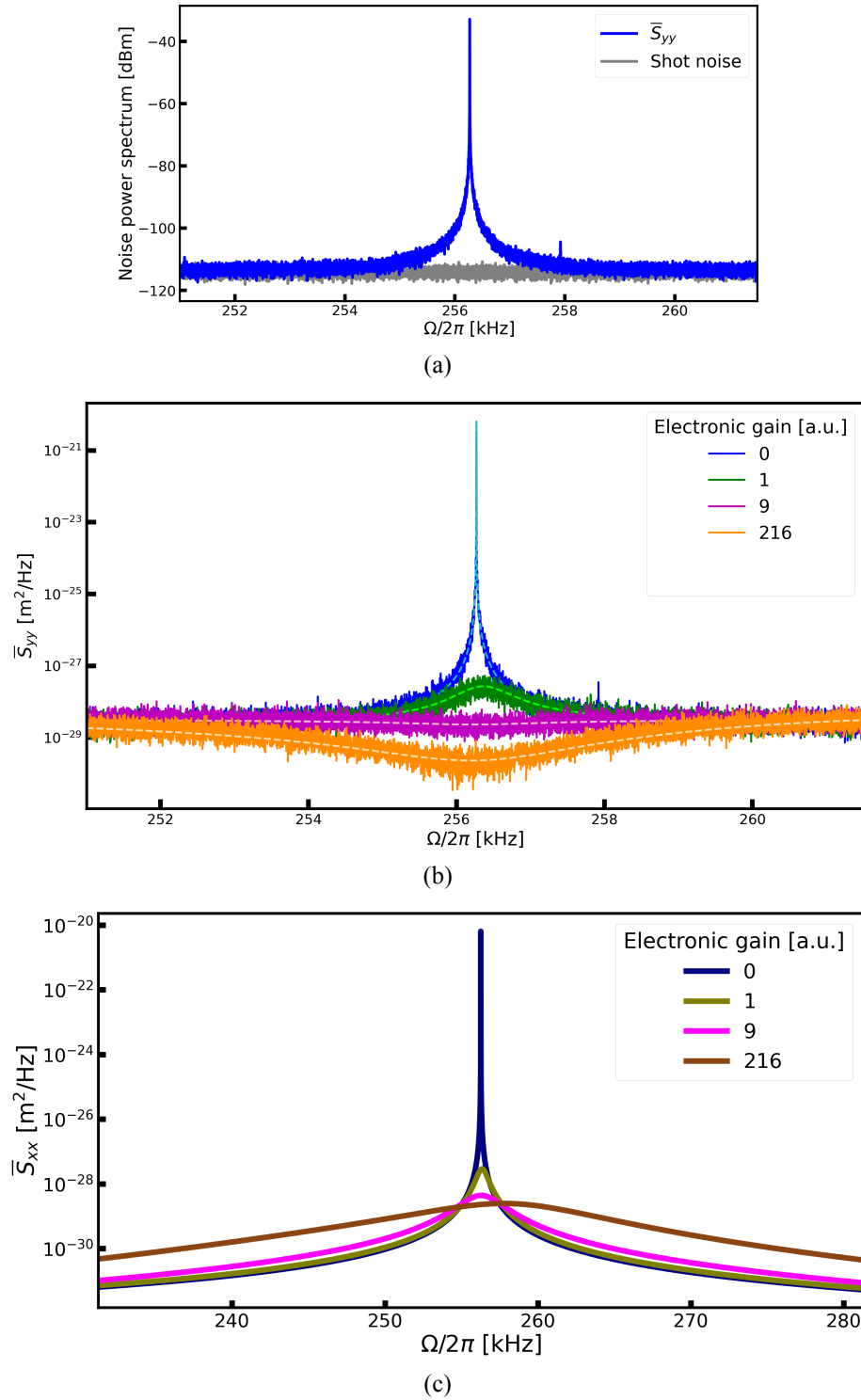


Figure 4.22: a) In-loop mechanical displacement spectrum in the absence of feedback cooling. The excess noise lies about 1 dB above the shot noise level. b) In-loop mechanical-displacement noise spectra of the fundamental mode of our TOTrampoline for different electronic gains. The dashed lines are obtained fitting the data to Eq. 4.23. The corresponding out-of-loop spectra are shown in Fig. c.

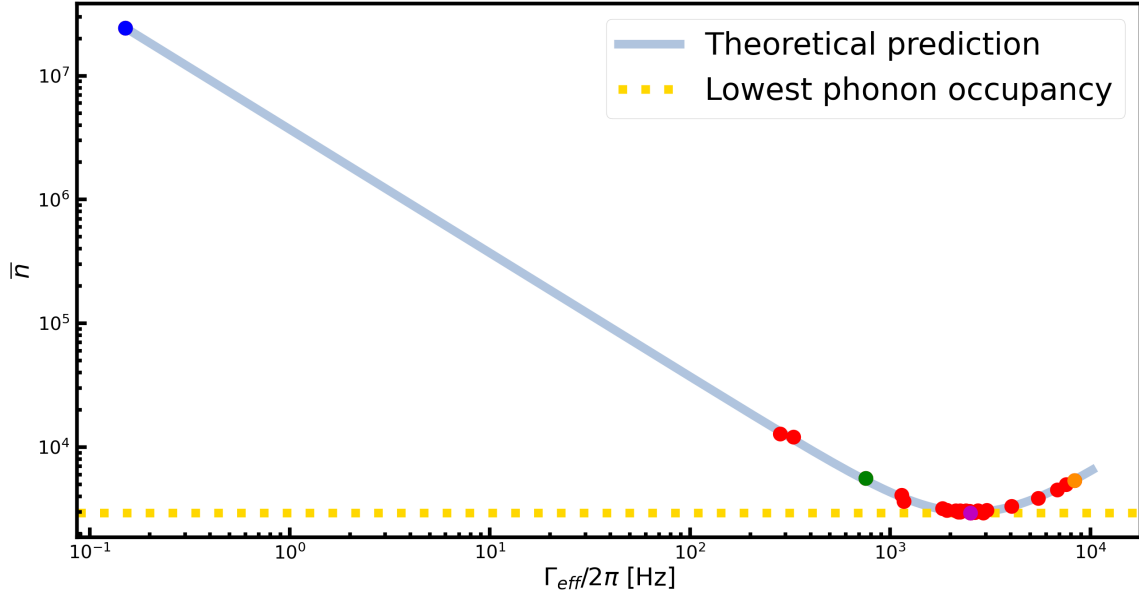


Figure 4.23: Phonon number occupancy  $\bar{n}$  of our TOTrampoline as a function of the effective mechanical linewidth  $\Gamma_{eff}$ . Blue, green, purple and orange circles represent the values extracted from the spectra in Figs. 4.22a-c. The red markers describe the values computed for other spectra from the same dataset. The dotted yellow line marks the lowest measured phonon occupancy  $\bar{n}^{min} = 2940 \pm 40$ , represented by the purple circle. Results are compared to a theoretical prediction (grey line) obtained from the  $n_{imp}$  and  $n_{tot}$  values estimated at zero gain and assuming  $\arg[h_{fb}(\Omega_M)] = \pi/2$ .

## 5 Conclusions

In the previous chapter, we presented the theory of optomechanical feedback cooling and our experimental realization of such protocol. Two versions of the experiment were presented, with the first one designed by my predecessor PhD candidate Jan Bilek and modified by me. This allowed feedback cooling of the fundamental vibrational mode of a trampoline from room temperature down to a minimum phonon occupancy of 39300 phonons. The estimated quantum cooperativity for a  $1 \mu\text{W}$  input power was about  $2 \times 10^{-7}$ , far below the unitary value necessary to reach the motional ground state of a mechanical resonator. A second version of the experiment was then conceived to increase this number. A new optomechanical assembly was designed to ensure a better spatial overlap between the intracavity field and the center of our mechanical resonators. This resulted in an increase of single-photon optomechanical coupling of up to six times with respect to the first setup. A phononic membrane and a topology-optimized trampoline (TOTrampoline) were chosen to replace the first tethered membrane given their higher mechanical quality factor. In order to minimize the imprecision noise, measurement inefficiencies were reduced. All sources of loss were examined, including homodyne visibility, intrinsic optical losses and quantum efficiency of the photodiodes and significant efforts were made to increase the corresponding efficiencies. For an input power of  $1 \mu\text{W}$ , the new setup features a quantum cooperativity of  $2 \times 10^{-6}$  and  $4 \times 10^{-6}$  in the case of the phononic membrane and the topology-optimized trampoline, respectively. Although these values are still far below unity, they represent an improvement of one order of magnitude with respect to the previous setup and an about 5000-fold improvement with respect to Jan Bilek's work [16]. Furthermore, in comparison with the first version of the experiment, the horizontal cavity offers a superior optical stability, enabling use of higher optical power and further enhancement of the quantum cooperativity. Room-temperature feedback cooling of the lowest-frequency bandgap mode of a phononic membrane and of the fundamental mode of a topology-optimized trampoline led to a minimum occupancy number of 1800 and 2940, respectively. We highlight that although a lower phonon number was achieved for the phononic membrane, this also features a lower room-temperature occupancy thanks to its 1.37 MHz mechanical frequency, about five times higher than the 260 kHz frequency of the TOTrampoline. The ratio between the room-temperature mechanical occupancy and the minimum achieved value is 2538 for the phononic membrane and 8300 for the TOTrampoline. The effective temperature corresponding to the minimum occupancy number obtained by feedback cooling is then 120 mK for the phononic membrane and 40 mK for the TOTrampoline.

Previous works on feedback cooling of mechanical resonators with MHz frequencies into the ground state partly based their success on the use of cryogenic equipment to pre-cool the mechanical mode of interest and lower its thermal occupancy [38]. The measurements presented in this work were carried out at room temperature, in order to avoid the practical limitations related to cryogeny and offer the possibility for a scalable experiment. The operating wavelength of 1550 nm was chosen to offer a wide variety of opportunities of integration with other experimental platforms, especially in the field quantum communication [47] and computation [48]. Being based on homodyne detection of light reflected off a high-finesse single-sided cavity, our experimental scheme is favourable for use of sources of non-classical light. In particular, previous experimental work carried out in our group proved the advantage of probing the mechanical motion with phase-squeezed light [40], which results in a higher detected SNR. Although significant effort went into minimizing the optical losses, further work might be required since optical inefficiencies have a strong detrimental effect on the properties of squeezed light [49].

In this work, we attempted to harness the expertise on fabrication of microresonators with high quality factors developed in our group in the last few years [17]. We studied three different res-

onator geometries, i.e. a trampoline, a phononic membrane and topology-optimized trampoline. In particular, the last oscillator was based on an original design conceived by Dennis Høj during his PhD in QPIT [46]. Unfortunately, ringdown measurements revealed a discrepancy between data acquired before and after dicing the silicon wafers carrying the membranes into chips. Original quality factors as high as  $10^8$  were observed to decrease to  $10^6$ , causing a severe limitation in the performance of our feedback-cooling scheme. The cause of this reduction was not thoroughly investigated and its origin is not clear. Possible causes are represented by sample contamination happening during the dicing process or by an enhancement of the phonon tunneling losses due to clamping of our mechanical resonators in the horizontal cavity assembly. Although neither hypothesis could be ruled out, we notice that for both the phononic membrane and the TOTrampoline also a decrease of mechanical frequency in the order of few percentages was observed after the chips were diced out. This could be due to an increase in the oscillator mass, seemingly supporting the contamination hypothesis. If such a dramatic drop in quality factor could be prevented, an increase of two orders of magnitude in quantum cooperativity would be achieved, thanks to its direct proportionality to the mechanical quality factor.

## Bibliography

- [1] URL: [https://en.wikipedia.org/wiki/Radiation\\_pressure](https://en.wikipedia.org/wiki/Radiation_pressure).
- [2] T.J. Kippenberg and K.J. Vahala. “Cavity Opto-Mechanics”. In: *Opt. Express* 15 (2007), pp. 17172–17205. DOI: 10.1364/OE.15.017172. URL: <https://opg.optica.org/oe/fulltext.cfm?uri=oe-15-25-17172&id=148383>.
- [3] Alexander G Krause et al. “A high-resolution microchip optomechanical accelerometer”. In: *Nature Photonics* 6.11 (2012), pp. 768–772.
- [4] David D. Awschalom Andrew N. Cleland Joerg Bochmann Amit Vainsencher. “Nanomechanical coupling between microwave and optical photons”. In: 9 (2013), pp. 712–716. DOI: 10.1038/nphys2748. URL: <https://www.nature.com/articles/nphys2748>.
- [5] Aspelmeyer Cole G. “Mechanical memory sees the light”. In: *Nature Nanotech* 6 (2011), pp. 690–691. DOI: 10.1038/nnano.2011.199. URL: <https://www.nature.com/articles/nnano.2011.199#citeas>.
- [6] V. B. Braginskii. “Classical and quantum restrictions on the detection of weak disturbances of macroscopic oscillator”. In: *Zh. Eksp. Teor. Fiz.* 53 (1967), pp. 1434–1441.
- [7] F. Y. Khalili V. B. Braginskii and K. S. Thorne. “Quantum measurement”. In: *Cambridge University Press* (1995), p. 191.
- [8] R. Riviere et al. “Optomechanical sideband cooling of a micromechanical oscillator close to the quantum ground state”. In: *Phys. Rev. A* 83 (6 June 2011), p. 063835. DOI: 10.1103/PhysRevA.83.063835. URL: <https://link.aps.org/doi/10.1103/PhysRevA.83.063835>.
- [9] C. F. Ockeloen-Korppi et al. “Sideband cooling of nearly degenerate micromechanical oscillators in a multimode optomechanical system”. In: *Phys. Rev. A* 99 (2 Feb. 2019), p. 023826. DOI: 10.1103/PhysRevA.99.023826. URL: <https://link.aps.org/doi/10.1103/PhysRevA.99.023826>.
- [10] Stefano Mancini, David Vitali, and Paolo Tombesi. “Optomechanical Cooling of a Macroscopic Oscillator by Homodyne Feedback”. In: *Phys. Rev. Lett.* 80 (4 Jan. 1998), pp. 688–691. DOI: 10.1103/PhysRevLett.80.688. URL: <https://link.aps.org/doi/10.1103/PhysRevLett.80.688>.
- [11] D. Leibfried et al. “Quantum dynamics of single trapped ions”. In: *Rev. Mod. Phys.* 75 (1 Mar. 2003), pp. 281–324. DOI: 10.1103/RevModPhys.75.281. URL: <https://link.aps.org/doi/10.1103/RevModPhys.75.281>.
- [12] D. Leibfried et al. “Real-time optimal quantum control of mechanical motion at room temperature”. In: *Nature* 595 (2021), pp. 373–377. DOI: 10.1038/s41586-021-03602-3. URL: <https://www.nature.com/articles/s41586-021-03602-3#citeas>.
- [13] Massimiliano Rossi et al. “Measurement-based quantum control of mechanical motion”. In: *Nature* 563.7729 (2018), pp. 53–58.
- [14] Yannick Seis et al. “Ground state cooling of an ultracoherent electromechanical system”. In: *Nature communications* 13.1 (2022), pp. 1–7.
- [15] Jingkun Guo, Richard Norte, and Simon Gröblacher. “Feedback Cooling of a Room Temperature Mechanical Oscillator close to its Motional Ground State”. In: *Phys. Rev. Lett.* 123 (22 Nov. 2019), p. 223602. DOI: 10.1103/PhysRevLett.123.223602. URL: <https://link.aps.org/doi/10.1103/PhysRevLett.123.223602>.
- [16] Jan Bilek. “Cavity optomechanical feedback cooling and magnetic field sensing”. In: (2019).
- [17] Dennis Høj. “Development of ultra-high quality mechanical oscillators”. In: (2021).
- [18] T. C. Ralph H. A. Bachor. “A Guide to Experiments in Quantum Optics”. In: (2004). URL: <https://doi.org/10.1002/9783527695805>.

- [19] W. Schleich. “Quantum optics in phase space”. In: (2001). URL: <https://doi.org/10.1002/3527602976>.
- [20] U. Leonhardt. “Measuring the Quantum State of Light”. In: (1997). URL: [https://doi.org/10.1016/0079-6727\(94\)00007-L](https://doi.org/10.1016/0079-6727(94)00007-L).
- [21] L. Neuhaus et al. “PyRPL (Python Red Pitaya Lockbox) — An open-source software package for FPGA-controlled quantum optics experiments”. In: *2017 Conference on Lasers and Electro-Optics Europe European Quantum Electronics Conference (CLEO/Europe-EQEC)* (2017), p. 1. DOI: 10.1109/CLEOE-EQEC.2017.8087380.
- [22] Andreas Barg. “Optomechanics with soft-clamped silicon nitride membranes and carrier-mediated forces in coupled quantum wells”. In: (2018).
- [23] Warwick P. Bowen and Gerard J. Milburn. “Quantum Optomechanics”. In: (2015). URL: <https://doi.org/10.1201/b19379>.
- [24] E. S. Polzik Y. Tsaturyan A. Barg and A. Schliesser. “Ultracoherent nanomechanical resonators via soft clamping and dissipation dilution”. In: *Nature Nanotechnology* 12 (2017), pp. 776–783. DOI: <https://doi.org/10.1038/nnano.2017.101>.
- [25] S. Schmid et al. “Damping mechanisms in high- $Q$  micro and nanomechanical string resonators”. In: *Phys. Rev. B* 84 (16 2011), p. 165307. DOI: 10.1103/PhysRevB.84.165307. URL: <https://link.aps.org/doi/10.1103/PhysRevB.84.165307>.
- [26] A. E. Siegman. “Lasers”. In: (1986).
- [27] A. Yariv and P. Yeh. “Optical waves in crystals: Propagation and control of laser radiation”. In: (1984).
- [28] Malvin Carl Teich Bahaa E. A. Saleh. “Fundamentals of Photonics”. In: (2007). URL: <https://doi.org/10.1002/0471213748>.
- [29] Yeghishe Tsaturyan et al. “Demonstration of suppressed phonon tunneling losses in phononic bandgap shielded membrane resonators for high- $Q$  optomechanics”. In: *Optics express* 22.6 (2014), pp. 6810–6821.
- [30] Eric D. Black. “An introduction to Pound–Drever–Hall laser frequency stabilization”. In: *American Journal of Physics* 69.1 (2001), pp. 79–87. DOI: 10.1119/1.1286663.
- [31] Leo W.Hollberg Richard W.Fox Chris W.Oates. “1. Stabilizing diode lasers to high-finesse cavities”. In: *Experimental Methods in the Physical Sciences* 40 (2003), pp. 1–46. DOI: 10.1016/S1079-4042(03)80017-6.
- [32] Steffen Schmidt-Eberle. “Phase and Frequency Locking of Diode Lasers”. In: *Toptica Photonics Application Note* (). URL: [https://www.toptica.com/fileadmin/Editors\\_English/04\\_applications/10\\_application\\_notes/01\\_Application\\_Note\\_-\\_Phase\\_and\\_Frequency\\_Locking\\_of\\_Diode\\_Lasers/Phase\\_and\\_Frequency\\_Locking\\_of\\_Diode\\_Lasers.pdf](https://www.toptica.com/fileadmin/Editors_English/04_applications/10_application_notes/01_Application_Note_-_Phase_and_Frequency_Locking_of_Diode_Lasers/Phase_and_Frequency_Locking_of_Diode_Lasers.pdf).
- [33] C. Biancofiore et al. “Quantum dynamics of an optical cavity coupled to a thin semitransparent membrane: Effect of membrane absorption”. In: *Phys. Rev. A* 84 (3 Sept. 2011), p. 033814. DOI: 10.1103/PhysRevA.84.033814. URL: <https://link.aps.org/doi/10.1103/PhysRevA.84.033814>.
- [34] T. J. Kippenberg M. Aspelmeyer and F. Marquardt. “Cavity optomechanics”. In: *Rev. Mod. Phys.* 86 (4 Dec. 2014), pp. 1391–1452. DOI: 10.1103/RevModPhys.86.1391. URL: <https://link.aps.org/doi/10.1103/RevModPhys.86.1391>.
- [35] ML Gorodetsky et al. “Determination of the vacuum optomechanical coupling rate using frequency noise calibration”. In: *Optics express* 18.22 (2010), pp. 23236–23246.
- [36] N. Piro et al D. Wilson V. Sudhir. “Measurement-based control of a mechanical oscillator at its thermal decoherence rate”. In: *Opt. Express* 524 (2015), pp. 325–329. DOI: 10.1038/nature14672.
- [37] O. Strobel H. Schmuck. “Stabilization of a Fiber-Optic Mach-Zehnder-Interferometer Used as an Intensity Modulator”. In: *Journal of Optical Communications* 3.7 (1986), pp. 86–91.

## BIBLIOGRAPHY

- [38] J. Chen et al. M. Rossi D. Mason. “Measurement-based quantum control of mechanical motion”. In: *Nature* 563 (2018), pp. 53–58. DOI: 10.1038/s41586-018-0643-8. URL: <https://www.nature.com/articles/s41586-018-0643-8>.
- [39] M. Poggio et al. “Feedback Cooling of a Cantilever’s Fundamental Mode below 5 mK”. In: *Phys. Rev. Lett.* 99 (1 July 2007), p. 017201. DOI: 10.1103/PhysRevLett.99.017201. URL: <https://link.aps.org/doi/10.1103/PhysRevLett.99.017201>.
- [40] U. Hoff et al. C. Schäfermeier H. Kerdoncuff. “Quantum enhanced feedback cooling of a mechanical oscillator using nonclassical light”. In: *Nat Commun* 7 (2016), p. 13628. DOI: 10.1038/ncomms13628. URL: <https://www.nature.com/articles/s41586-018-0643-8>.
- [41] Christian M Pluchar et al. “Towards cavity-free ground-state cooling of an acoustic-frequency silicon nitride membrane”. In: *Applied optics* 59.22 (2020), G107–G111.
- [42] R. A. Norte, J. P. Moura, and S. Gröblacher. “Mechanical Resonators for Quantum Optomechanics Experiments at Room Temperature”. In: *Phys. Rev. Lett.* 116 (14 Apr. 2016), p. 147202. DOI: 10.1103/PhysRevLett.116.147202. URL: <https://link.aps.org/doi/10.1103/PhysRevLett.116.147202>.
- [43] Dalziel J Wilson et al. “Measurement-based control of a mechanical oscillator at its thermal decoherence rate”. In: *Nature* 524.7565 (2015), pp. 325–329.
- [44] Niels Aage et al. “Giga-voxel computational morphogenesis for structural design”. In: *Nature* 550.7674 (2017), pp. 84–86.
- [45] M Baandrup et al. *Closing the gap towards super-long suspension bridges using computational morphogenesis. Nat Commun* 11 (1): 2735. 2020.
- [46] Dennis Høj et al. “Ultra-coherent nanomechanical resonators based on inverse design”. In: *Nature communications* 12.1 (2021), pp. 1–8.
- [47] Xueshi Guo et al. “Distributed quantum sensing in a continuous-variable entangled network”. In: *Nature Physics* 16.3 (2020), pp. 281–284.
- [48] Mikkel V Larsen et al. “Deterministic multi-mode gates on a scalable photonic quantum computing platform”. In: *Nature Physics* 17.9 (2021), pp. 1018–1023.
- [49] Jens Arnbak Holbøll Nielsen. “Generation and Application of Squeezed States of Light in Quantum Sensing”. In: (2021).



*BIBLIOGRAPHY*

